

Global modelling of soil carbonyl sulfide exchanges

Camille Abadie¹, Fabienne Maignan¹, Marine Remaud¹, Jérôme Ogée², J. Elliott Campbell³, Mary E. Whelan⁴, Florian Kitz⁵, Felix M. Spielmann⁵, Georg Wohlfahrt⁵, Richard Wehr⁶, Wu Sun⁷, Nina Raoult¹, Ulli Seibt⁸, Didier Hauglustaine¹, Sinikka T. Lennartz^{9,10}, Sauveur Belviso¹, David Montagne¹¹ and Philippe Peylin¹.

¹Laboratoire des Sciences du Climat et de l'Environnement, LSCE/IPSL, CEA-CNRS-UVSQ, Université Paris-Saclay, Gif-sur-Yvette, France

²INRA, UMR 1391 ISPA, 33140 Villenave d'Ornon, France

³Sierra Nevada Research Institute, University of California, Merced, California 95343, USA

⁴Department of Environmental Sciences, Rutgers University, New Brunswick, NJ 08901, USA

⁵Department of Ecology, University of Innsbruck, Innsbruck, 6020, Austria

⁶Center for Atmospheric and Environmental Chemistry, Aerodyne Research, Inc., Billerica, Massachusetts, 01821, USA.

⁷Department of Global Ecology, Carnegie Institution for Science, Stanford, CA 94305, USA

⁸Department of Atmospheric & Oceanic Sciences, University of California Los Angeles, California 90095, USA

⁹Institute of Chemistry and Biology of the Marine Environment, University of Oldenburg, 26129 Oldenburg, Germany

¹⁰Department of Earth, Atmospheric and Planetary Sciences, Massachusetts Institute of Technology, Cambridge, 02139, MA, USA

¹¹AgroParisTech, INRAE, Université Paris-Saclay, UMR ECOSYS, 78850 Thiverval-Grignon, France

Correspondence to: Camille Abadie (camille.abadie.research@gmail.com)

Abstract. Carbonyl sulfide (COS) is an atmospheric trace gas of interest for C cycle research because COS uptake by continental vegetation is strongly related to terrestrial gross primary productivity (GPP), the largest and most uncertain flux in atmospheric CO₂ budgets. However, to use atmospheric COS budgets as an additional tracer of GPP, an accurate quantification of COS exchange by soils is also needed. At present, the atmospheric COS budget is unbalanced globally, with total COS flux estimates from oxic and anoxic soils that vary between -409 and -104 89 GgS yr⁻¹. This uncertainty hampers the use of atmospheric COS concentrations to constrain GPP estimates through atmospheric transport inversions. In this study we implemented a mechanistic soil COS model in the ORCHIDEE land surface model to simulate COS fluxes in oxic and anoxic soils. Evaluation of the model against flux measurements at 7 sites yields a mean root mean square deviation of 1.6 pmol m⁻² s⁻¹, instead of 2 pmol m⁻² s⁻¹ when using a previous empirical approach that links soil COS uptake to soil heterotrophic respiration. However, soil COS model evaluation is still limited by the scarcity of observation sites and long-term measurement periods, with all sites located in a latitudinal band between 39°N and 62°N and no observations during wintertime in this study. The new model predicts that, globally and over the 2009-2016 period, oxic soils act as a net uptake of -126 GgS yr⁻¹, and anoxic soils are a source of +96 GgS yr⁻¹, leading to a global net soil sink of only -30 GgS yr⁻¹, i.e., much smaller than previous estimates. The small magnitude of the soil fluxes suggests that the error in the COS budget is dominated by the much larger fluxes from plants, oceans, and industrial activities. The predicted spatial distribution of soil COS fluxes, with large emissions in the tropics from oxic (up to 68.2 pmol COS m⁻² s⁻¹) and anoxic (up to 36.8 pmol COS m⁻² s⁻¹) soils in the tropics, especially in India and in the Sahel region, marginally improves the latitudinal gradient of atmospheric COS concentrations, after transport by the LMDZ atmospheric transport model. The impact of different soil COS flux representations on the latitudinal gradient of the atmospheric COS concentrations is strongest in the northern hemisphere. We also implemented spatio-temporal variations of near-ground atmospheric COS concentrations in the modelling of biospheric COS fluxes, which

a mis en forme : Justifié

45 helped reduce the imbalance of the atmospheric COS budget by lowering ~~COS uptake by soils~~ soil COS uptake by
46 10% and plant COS uptake by 8% ~~soils and vegetation~~ globally (~~-10% for soil, and -8% for vegetation~~ with
47 a revised mean vegetation budget estimate of -576 GgS yr^{-1} over 2009-2016). Sensitivity analyses highlighted
48 the different parameters to which each soil COS flux model is the most responsive, selected in a parameter
49 optimization framework. Having both vegetation and soil COS fluxes modelled within ORCHIDEE opens the way
50 for using observed ecosystem COS fluxes and larger scale atmospheric COS mixing ratios to improve the
51 simulated GPP, through data assimilation techniques.

52 1 Introduction

53 Carbonyl sulfide (COS) has been proposed as a tracer for constraining the simulated Gross Primary Productivity
54 (GPP) in Land Surface Models (LSMs) (Launois et al., 2015; Remaud et al., ~~2021~~~~2021~~~~2021~~~~2021~~~~2022~~; Campbell
55 et al., 2008). COS is an atmospheric trace gas that is scavenged by plants at the leaf level through stomatal uptake
56 and irreversibly hydrolyzed in a reaction catalyzed by the enzyme Carbonic Anhydrase (CA) (Protoschill-Krebs
57 et al., 1996). This enzyme also interacts with CO_2 inside leaves. COS and CO_2 follow a similar pathway from the
58 atmosphere to the leaf interior. However, while CO_2 is also released during respiration, plants generally do not
59 emit COS (Montzka et al., 2007; Sandoval-Soto et al., 2005; Wohlfahrt et al., 2012). To infer GPP at the regional
60 scale using COS observations, modelers can use measurements of ecosystem COS fluxes directly, or
61 measurements of atmospheric COS concentrations combined with an atmospheric transport inversion model,
62 provided all COS flux components are taken into account. In both cases, net soil COS flux estimates are needed,
63 as well as a functional relationship between GPP and COS uptake by foliage.

64 One important limitation for using COS as a tracer for GPP is the uncertainty that remains on the COS budget
65 components. Several atmospheric transport inversion studies have suggested that an unidentified COS source
66 located over the tropics, of the order of $400\text{-}600 \text{ GgS yr}^{-1}$, was needed to close the contemporary COS budget
67 (Berry et al., 2013; Glatthor et al., 2015; Kuai et al., 2015; Ma et al., 2021; Remaud et al., 2022). It was recently
68 estimated to account for 432 GgS yr^{-1} by Ma et al. (2021)~~Several atmospheric transport inversion studies have~~
69 ~~suggested that a COS source located over the tropical oceans and estimated between 700 and 1100 GgS yr^{-1} was~~
70 ~~missing to close the contemporary COS budget (Berry et al., 2013; Glatthor et al., 2015; Kuai et al., 2015).~~
71 ~~ThisThisThisThies~~ hypothesis of a strong tropical oceanic source has not been substantiated by in situ COS and
72 CS_2 measurements in sea waters (Lennartz et al., 2017, 2020, 2021), except by Davidson et al. (2021) that invoke
73 an oceanic source of $600 \pm 400 \text{ GgS yr}^{-1}$ based on direct measurements of sulfur isotopes. Clearly, an accurate
74 characterization of all flux components of the atmospheric COS budget is still needed. In particular, the
75 contribution of soils to the COS budget is poorly constrained and improved estimates of their contribution may
76 therefore provide clues to the attribution of the missing source.

77 A distinction is usually made between oxic soils that mainly absorb COS, and anoxic soils that emit COS (Whelan
78 et al., 2018). Regarding COS uptake, COS diffuses into the soil, where it is hydrolyzed by CA contained in soil
79 microorganisms such as fungi and bacteria (Smith et al., 1999). It is to be noted that COS can also be consumed
80 by other enzymes, like nitrogenase, CO dehydrogenase, or CS_2 hydrolase (Smith and Ferry, 2000; Masaki et al.,
81 2021), but these enzymes are less ubiquitous than CA. The rate of uptake varies with soil type, temperature, and
82 soil moisture (Kesselmeier et al., 1999; VanDiest et al. 2007; Whelan et al., 2016). With high temperature or
83 radiation, soils were also found to emit COS through thermal or photo degradation processes (Kitz et al., 2017,

84 2020; Whelan and Rhew, 2015; Whelan et al., 2016, 2018). Although such COS emissions can be large in some
85 conditions, ~~they are usually neglected in current figures of the atmospheric COS budget. they have usually not been~~
86 ~~considered in atmospheric COS budgets.~~

87 Using the empirical relationship between soil COS uptake and soil respiration by Yi et al. (2007), Berry et al.
88 (2013) provided new global estimates of COS uptake by oxic soils. Launois et al. (2015) proposed another
89 empirical model, linking oxic soil COS uptake to H₂ deposition based on the correlation between these two
90 processes observed at Gif-sur-Yvette (Belviso et al., 2013). Models with a physical representation of the involved
91 processes are also available. Sun et al. (2015) proposed such a mechanistic model including COS diffusion and
92 reactions within a layered soil. Ogée et al. (2016) also developed a mechanistic model including both COS uptake
93 and production, with steady-state analytical solutions in homogeneous soils. When including such models in an
94 LSM, the challenge is to spatialize them, which requires new variables or parameters not readily available at the
95 global scale but inferred ~~form-from~~ field or lab experiments.

96 In this study, our goal is to provide and evaluate new global estimates of net soil COS exchange. To this end:

- 97 i. We implemented an empirical-based and a mechanistic-based soil COS model in the ORCHIDEE
98 LSM;
- 99 ii. We evaluated the soil COS models at seven sites against in situ flux measurements;
- 100 iii. We estimated soil contributions to the COS budget at the global scale;
- 101 iv. We transported all COS sources and sinks using an atmospheric model and evaluated the
102 concentrations against measurements of the National Oceanic and Atmospheric Administration
103 (NOAA) air sampling network.

104 2 Methods

105 2.1 Description of the models

106 2.1.1 The ORCHIDEE Land Surface Model

107 The ORCHIDEE Land Surface Model is developed at the Institut Pierre Simon Laplace (IPSL). The model version
108 used here is the one involved in the 6th Coupled Model Inter-comparison Project (CMIP6) (Boucher et al., 2020;
109 Cheruy et al., 2020). ORCHIDEE computes the carbon, water and energy balances over land surfaces. It can be
110 run at the site level or at the global scale. Fast processes such as soil hydrology, photosynthesis and respiration are
111 computed at a half-hourly time step. Other processes such as carbon allocation, leaf phenology and soil carbon
112 turnover are evaluated at a daily time step. Plant species are classified into 14 Plant Functional Types (PFTs),
113 according to their structure (trees, grasslands, croplands), bioclimatic range (boreal, temperate, tropical), leaf
114 phenology (broadleaf versus evergreen) and photosynthetic pathway (C₃ versus C₄). The vegetation distribution in
115 each grid cell is prescribed using yearly-varying PFT maps, derived from the ESA Climate Change Initiative (CCI)
116 land cover products (Poulter et al., 2015).

117 Soil parameters such as soil porosity, wilting point, and field capacity are derived from a global map of soil textures
118 based on the FAO/USDA (Food and Agriculture Organization of the United Nations/United States Department of
119 Agriculture) texture classification with 12 texture classes (Reynolds et al., 2000). The different textures for the
120 USDA classification are presented in Table S1 in the supporting information. To better represent the observed soil
121 conditions at the different sites ~~that will be used for evaluation in this study~~, we substituted the soil textures initially
122 assigned in ORCHIDEE from the USDA texture global map with the ~~observed-field~~ soil textures ~~corresponding~~
123 ~~to the~~translated into USDA texture classes (Table S2). In a previous study of vegetation COS fluxes in
3

a mis en forme : Justifié

124 ORCHIDEE, Maignan et al. (2021) used the global soil map based on the Zobler texture classification (Zobler,
125 1986), which is reduced to 3 different textures in ORCHIDEE. However, the USDA soil classification gives a
126 finer description of the different soil textures than the Zobler soil classification, considering 12 soil textures instead
127 of 3. The move from the coarse Zobler classes to the finer USDA classes is found to be more important to the
128 mechanistic model [than to the empirical model](#). Since the USDA texture classes are more accurate with its finer
129 discretization of soil textures, in the rest of this study, we only illustrate the results based on the USDA texture
130 classification.

131
132
133 For site level simulations, the ORCHIDEE LSM was forced by local micro-meteorological measurements obtained
134 from the FLUXNET network at the FLUXNET sites following the Creative Commons (CC-BY 4.0) license
135 (Pastorello et al., 2020), and at the remaining sites by other local meteorological measurements performed together
136 with the COS fluxes measurements when available, eventually gap-filled using the $0.25^\circ \times 0.25^\circ$, hourly reanalysis
137 from the fifth generation of meteorological analyses of the European Centre for Medium-Range Weather Forecasts
138 (ECMWF) (ERA5) (Hersbach et al., 2020). Global simulations were forced by the 0.5° and 6-hourly CRUJRA
139 reanalysis (Friedlingstein et al., 2020). Near-surface COS concentrations (noted C_a below) were prescribed using
140 monthly-mean atmospheric COS concentrations at the first vertical level of the LMDZ atmospheric transport
141 model (GCM, see description below in Sect. 2.1.3), forced with optimized COS surfaces fluxes. The latter have
142 been inferred by atmospheric inverse modelling from the COS surface measurements of the NOAA network
143 (Remaud et al., 2024). Simulations with constant atmospheric COS concentrations at a mean global value of 500
144 ppt were also run, to evaluate the impact of spatio-temporal variations of near-surface COS concentrations versus
145 a constant value. Near-surface CO_2 concentrations were estimated using global yearly-mean values provided by
146 the TRENDY project (Sitch et al., 2015).

147

148 2.1.2 COS soil models

149 The empirical soil COS flux model

150 We implemented in the ORCHIDEE LSM the soil COS flux model from Berry et al. (2013), which assumes that
151 COS uptake is proportional to CO_2 production by soil respiration, following Yi et al. (2007). Although Yi et al.
152 (2007) reported a relationship between soil COS uptake and total soil respiration, including root respiration, Berry
153 et al. (2013) assumed that COS flux was proportional to soil heterotrophic respiration only. The rationale behind
154 this assumption is that soil CA concentration is related to soil organic matter content, and thus ecosystem
155 productivity (Berry et al., 2013). As heterotrophic respiration is also linked to productivity, Berry et al. (2013)
156 considered soil COS uptake to be proportional to soil heterotrophic respiration. However, soil respiration alone
157 did not correlate well in incubation studies (Whelan et al., 2016). As the proportionality between COS fluxes and
158 soil respiration has only been demonstrated for the total (heterotrophic and autotrophic) soil respiration (Yi et al.
159 2007), we used in this study total soil respiration as a scaling factor for soil COS uptake. This model will be
160 referred to as the empirical model.

161

162 The influence of soil temperature and moisture are included in the calculation of soil respiration. Thus, we
163 computed soil COS flux $F_{\text{soil},\text{empirical}}$ ($\text{pmol COS m}^{-2} \text{s}^{-1}$) as follows,

4

a mis en forme : Justifié

164 $F_{soil,empirical} = -k_{soil} * Resp_{tot}$ (1)

165 where $Resp_{tot}$ is total soil respiration ($\mu\text{mol CO}_2 \text{ m}^{-2} \text{ s}^{-1}$) and k_{soil} is a constant equal to $1.2 \text{ pmol COS } \mu\text{mol}^{-1}$
 166 CO_2 that converts CO_2 production from respiration to COS uptake. The value of $1.2 \text{ pmol COS } \mu\text{mol}^{-1}$ was
 167 estimated from field chamber measurements in a pine and broadleaf mixed forest (Dinghushan Biosphere Reserve,
 168 south China) from Yi et al. (2007). In ORCHIDEE, we calculated the total soil respiration as the sum of soil
 169 heterotrophic respiration within the soil column, including that of the litter, and root autotrophic respiration.

170 **The mechanistic soil COS flux model**

171 The mechanistic COS soil model of Ogée et al. (2016) describes both soil COS uptake and production. This model
 172 includes COS diffusion in the soil matrix, COS dissolution and hydrolysis in the water-filled pore space and COS
 173 production under low redox conditions. ~~COS advection is neglected as the advective flux becomes negligible for~~
 174 ~~time scales longer than 1 h (Ogée et al., 2016).~~ The soil is assumed to be horizontally homogeneous so that the
 175 soil COS concentration C (mol m^{-3}) is only a function of time t (s) and soil depth z (m). The mass balance equation
 176 for COS can then be written as (Ogée et al., 2016),

177 $\frac{\partial \varepsilon_{tot} C}{\partial t} = -\frac{\partial F_{diff}}{\partial z} + P - S$ (2)

178 with ε_{tot} the soil total porosity ($\text{m}^3 \text{ air m}^{-3} \text{ soil}$), F_{diff} the diffusional flux of COS ($\text{mol m}^{-2} \text{ s}^{-1}$), S the COS
 179 consumption rate ($\text{mol m}^{-3} \text{ s}^{-1}$) and P the COS production rate under low redox conditions ($\text{mol m}^{-3} \text{ s}^{-1}$).
 180 Under steady-state conditions and uniform soil temperature, moisture and porosity profiles, an analytical solution
 181 of Eq. 2 can be found (Ogée et al., 2016). We assume that the environmental conditions, such as soil temperature
 182 and moisture, are constant in ORCHIDEE over the 30-minute model time step. We also assume chemical
 183 equilibrium between the gaseous and the dissolved COS, neglecting advection as suggested by Ogée et al. (2016).
 184 In these conditions, the typical time scale for COS diffusion in the upper active soil layer is much shorter than the
 185 30-minute model time step. Although Eq. 2 could also be solved numerically using the soil discretization in
 186 ORCHIDEE, we preferred to use the analytical solution, using the mean soil moisture and temperature averaged
 187 over the first few soil layers (down to about 9 cm deep), weighted by the thickness of each soil layer. Assuming
 188 fully mixed atmospheric conditions within and below the vegetated canopy, we also assumed that the COS
 189 concentration at the soil surface $C(z=0)$ is equal to the near-surface COS concentration C_a . With these boundaries'
 190 conditions, the steady-state COS flux at the soil surface $F_{soil,mechanistic}$ ($\text{mol m}^{-2} \text{ s}^{-1}$) is (Ogée et al., 2016),

191 $F_{soil,mechanistic} = \sqrt{kB\theta D} \left(C_a - \frac{z_1^2 P}{D} (1 - \exp(-z_{max}/z_1)) \right)$ (3)

192 with k the first-order COS consumption rate constant within the soil (s^{-1}), B the solubility of COS in water (m^3
 193 water m^{-3} air), θ the soil volumetric water content ($\text{m}^3 \text{ water m}^{-3} \text{ soil}$), D the total effective COS diffusivity (m^2
 194 s^{-1}), $z_1 = \sqrt{D/kB\theta}$ (m) and z_{max} the soil depth below which the COS production rate and the soil COS gradient
 195 are assumed negligible (Ogée et al., 2016). In the following, z_{max} is set at 0.09 m.

196 COS diffusion

197 The total effective COS diffusivity in soil, D , includes the effective diffusivity of gaseous COS $D_{eff,a}$ ($\text{m}^3 \text{air m}^{-1}$
198 soil s^{-1}) and dissolved COS $D_{eff,l}$ ($\text{m}^3 \text{water m}^{-1} \text{soil s}^{-1}$) through the soil matrix,

$$199 \quad D = D_{eff,a} + D_{eff,l} B \quad (4)$$

200 The solubility of COS in water B is calculated using Henry's law constant K_H ($\text{mol m}^{-3} \text{Pa}^{-1}$),

$$201 \quad B = K_H R T \quad (5)$$

202 with $R = 8,314 \text{ J mol}^{-1} \text{K}^{-1}$ the ideal gas constant and T the soil temperature (K) and (Wilhelm et al., 1977),

$$203 \quad K_H = 0.00021 \exp[24900/R(1/T - 1/298,15)] \quad (6)$$

204 The effective diffusivity of gaseous COS $D_{eff,a}$ is expressed as (Ogée et al., 2016),

$$205 \quad D_{eff,a} = D_{0,a} \tau_a \varepsilon_a \quad (7)$$

206 with $D_{0,a}$ the binary diffusivity of COS in the air ($\text{m}^2 \text{air s}^{-1}$), τ_a the air tortuosity factor representing the tortuosity
207 of the air-filled pores, and ε_a is the air-filled porosity ($\text{m}^3 \text{air m}^{-3} \text{soil}$). The binary diffusivity of COS in the air
208 $D_{0,a}$ is expressed following the Chapman-Enskog theory for ideal gases (Bird et al., 2002) and depends on
209 temperature and pressure,

$$210 \quad D_{0,a}(T, p) = D_{0,a}(T_0, p_0) \left(\frac{T}{T_0}\right)^{1.5} \left(\frac{p}{p_0}\right) \quad (8)$$

211 with $D_{0,a}(T_0, p_0) = D_{0,a}(25^\circ\text{C}, 1 \text{ atm}) = 1.27 \times 10^{-5} \text{ m}^2 \text{ s}^{-1}$ (Massman, 1998).

212 The expression of the air tortuosity factor τ_a depends on whether the soil is repacked or undisturbed. In
213 ORCHIDEE, repacked soils correspond to the agricultural soils represented by the C_3 and C_4 crops. Soils not
214 covered by crops are considered as undisturbed soils. The expression of τ_a for repacked soils $\tau_{a,r}$ is given by
215 Moldrup et al. (2003),

$$216 \quad \tau_{a,r} = \varepsilon_a^{3/2} / \varphi \quad (9)$$

217 with φ the soil porosity ($\text{m}^3 \text{m}^{-3}$) that includes the air-filled and water-filled pores. Soil porosity is assumed constant
218 through the soil column in ORCHIDEE and is determined by the USDA texture global map. The air-filled porosity
219 ε_a is calculated as $\varepsilon_a = \varphi - \theta$.

220 The expression of τ_a for undisturbed soils $\tau_{a,u}$ is given in Deepagoda et al. (2011). We chose this expression rather
221 than the expression proposed by Moldrup et al. (2003) for undisturbed soils because it appears to be more accurate
222 and does not require information on the pore-size distribution (Ogée et al., 2016),

$$223 \quad \tau_{a,u} = [0.2(\varepsilon_a/\varphi)^2 + 0.004]/\varphi \quad (10)$$

224 In a similar way to COS diffusion in the gas phase, the effective diffusivity of dissolved COS $D_{eff,l}$ is described
225 by Ogée et al. (2016),

226 $D_{eff,l} = D_{0,l} \tau_l \theta$ (11)

227 with $D_{0,l}$ the binary diffusivity of COS in the free water ($\text{m}^2 \text{ water s}^{-1}$) and τ_l the tortuosity factor for solute
 228 diffusion. The binary diffusivity of COS in the free water $D_{0,l}$ is described using an empirical formulation proposed
 229 by Zeebe (2011) for CO_2 , which only depends on temperature,

230 $D_{0,l}(T) = D_{0,l}(T_0) \left(\frac{T}{T_0} - 1 \right)^2$ (12)

231 with $T_0 = 216\text{K}$ (Ogée et al., 2016) and $D_{0,l}(25^\circ\text{C}) = 1.94 \times 10^{-9} \text{ m}^2 \text{ s}^{-1}$ (Ulshöfer et al., 1996).
 232 The expression of τ_l is the same for repacked and undisturbed soils. We used the expression given by Millington
 233 and Quirk (1961) as a good compromise between simplicity and accuracy (Moldrup et al. 2003),

234 $\tau_l = \theta^{7/3} / \phi^2$ (13)

235 COS consumption

236 COS can be destroyed by biotic and abiotic processes. The abiotic process corresponds to COS hydrolysis in soil
 237 water at an uncatalyzed rate k_{uncat} (s^{-1}), which depends on soil temperature T (K) and pH (Elliott et al., 1989),

238 $k_{uncat} = 2.15 \cdot 10^{-5} \exp\left(-10450\left(\frac{1}{T} - \frac{1}{298.15}\right)\right) + 12.7 \cdot 10^{-pK_w + pH} \exp\left(-6040\left(\frac{1}{T} - \frac{1}{298.15}\right)\right)$ (14)

239 with pK_w the dissociation constant of water.
 240 This uncatalyzed hydrolysis is quite low compared to the COS hydrolysis catalysed by soil microorganisms, which
 241 is the main contribution of COS uptake by soils (Kesselmeier et al., 1999; Sauze et al., 2017; Meredith et al.,
 242 2018). The enzymatic reaction catalysed by CA follows Michaelis-Menten kinetics. The turnover rate k_{cat} (s^{-1})
 243 and the Michaelis-Menten constant K_m (mol m^{-3}) of this reaction depend on temperature. The temperature
 244 dependence of the ratio $\frac{k_{cat}}{K_m}$ is expressed as (Ogée et al., 2016),

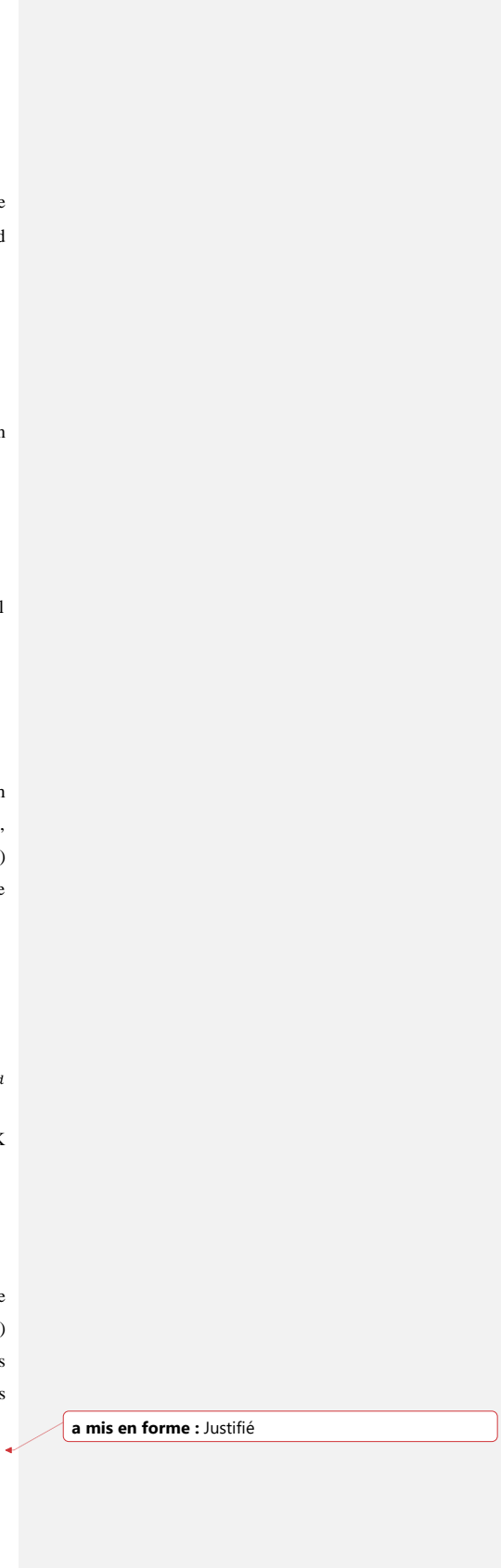
245 $x_{CA}(T) = \frac{\exp\left(-\frac{\Delta H_a}{RT}\right)}{1 + \exp\left(-\frac{\Delta H_d + \Delta S_d}{RT} + \frac{\Delta S_d}{R}\right)}$ (15)

246 where ΔH_a , ΔH_d and ΔS_d are thermodynamic parameters, such as $\Delta H_a = 40 \text{ kJ mol}^{-1}$, $\Delta H_d = 200 \text{ kJ mol}^{-1}$ and ΔS_d
 247 $= 660 \text{ J mol}^{-1} \text{ K}^{-1}$.

248 The total COS consumption rate by soil k (s^{-1}) is described with respect to the uncatalyzed rate at $T = 298.15 \text{ K}$
 249 and $pH = 4.5$ (Ogée et al., 2016),

250 $k = f_{CA} k_{uncat}(298.15, 4.5) \frac{x_{CA}(T)}{x_{CA}(298.15)}$ (16)

251 where f_{CA} is the CA enhancement factor, which characterizes the soil microbial community that can consume
 252 COS. The CA enhancement factor depends on soil CA concentration, temperature, and pH. Ogée et al. (2016)
 253 reported that its values range between 21 600 and 336 000, with a median value at 66 000. We adapted the values
 254 of f_{CA} found in (Meredith et al., 2019) to have a CA enhancement factor that depends on ORCHIDEE biomes
 255 (Appendix A, Table A1).



a mis en forme : Justifié

256 Oxic soil COS production

257 Abiotic oxic soil COS production has been observed at high soil temperature (Maseyk et al., 2014; Whelan and
258 Rhew, 2015; Kitz et al., 2017, 2020; Spielmann et al., 2019, 2020). However, photodegradation has also been
259 proposed as an abiotic production mechanism in oxic soils (Whelan and Rhew, 2015; Kitz et al., 2017, 2020).

260 Abiotic COS production is still not well understood but was assumed to originate from biotic precursors (Meredith
261 et al., 2018).

262 In Ogée et al. (2016), the production rate P is described as independent of soil pH but depends on soil temperature
263 and redox potential. This dependence on soil redox potential enables us to consider the transition between oxic
264 and anoxic soils. However, because little information is available on soil redox potential at the global scale, its
265 influence cannot yet be represented in a spatially and temporally dynamic way in a land surface model such as
266 ORCHIDEE. Thus, we decided to use the production rate described in Whelan et al. (2016) that only depends on
267 soil temperature and land use type,

268
$$P_{oxic} = e^{\alpha + \beta T} \quad (17)$$

269 where P_{oxic} is expressed in $\text{pmol g}^{-1} \text{min}^{-1}$, T is soil temperature ($^{\circ}\text{C}$) and α and β are parameters determined by
270 Whelan et al. (2016) for each land use type using the least-squares fitting approach. We adapted the values of α
271 and β given for four land use types to ORCHIDEE biomes (Appendix A Table A2). Values of α and β for deserts
272 could not be estimated by Whelan et al. (2016) because COS emission for this biome was not found to increase
273 with temperature. Figure 11 in Whelan et al. (2016) shows that COS emission from a desert soil is always near
274 zero for temperatures ranging from 10°C to 40°C . Moreover, COS emission from a desert soil is also found to be
275 near zero in Fig. 1 of Meredith et al. (2018). This could be explained by a lack of organic precursors to produce
276 COS (Whelan et al., 2016). Therefore, we considered that desert soils, which correspond to a specific non-
277 vegetated PFT in ORCHIDEE, do not emit COS. For other ORCHIDEE biomes, COS production was estimated
278 using α and β for each PFT and the mean soil temperature over the top 9 cm. The unit of P_{oxic} was converted from
279 $\text{pmol g}^{-1} \text{min}^{-1}$ to $\text{mol m}^{-3} \text{s}^{-1}$ (in equation 3) using soil bulk density information from the Harmonized World Soil
280 Database (HWSD; FAO/IIASA/ISRIC/ISSCAS/JRC, 2012).

281

282 Anoxic soil COS production/emission

283 Several studies have shown direct COS emissions by anoxic soils (Devai and DeLaune, 1997; de Mello and Hines,
284 1994; Whelan et al., 2013; Yi et al., 2007). This has been linked to a strong activity of sulfate reduction
285 metabolisms in highly reduced environments such as wetlands (Aneja et al., 1981; Kanda et al., 1992; Whelan et
286 al., 2013; Yi et al., 2007). A previous approach developed by Launois et al. (2015) was based on the representation
287 of seasonal methane emissions by Wania et al. (2010) in the LPJ-WHyME model to represent anoxic soils in
288 ORCHIDEE. The mean values of soil COS emissions from Whelan et al. (2013) were used to attribute to each
289 grid point a value of soil COS emission. In this approach by Launois et al. (2015), salt marshes were not represented
290 despite their strong COS emissions found in Whelan et al. (2013). Emissions from rice paddies were also neglected.
291 Thus, COS emissions from anoxic soils peaked in summer over the high latitudes, following methane production.
292 Because of the scarce knowledge on anoxic soil COS exchange, here we propose another approach to represent
293 the contribution of anoxic soils, which could be compared to the previous approach developed by Launois et al.
294 (2015). To represent the distribution of anoxic soils we selected the regularly flooded wetlands from the map

8

a mis en forme : Police :Non Gras, Soulignement

a mis en forme : Justifié

295 developed by Tootchi et al. (2019), as represented in Fig. 1. The regularly flooded wetlands cover 9.7% of the
296 global land area, which is among the average values found in the literature ranging from 3% to 21% (Tootchi et
297 al., 2019). Then, in ORCHIDEE each pixel is either considered as anoxic following the wetland map distribution
298 from Tootchi et al. (2019), or as oxic for the rest of the land surfaces. The pixels defined as anoxic soils are
299 considered flooded through the entire year: the seasonal variations of the flooding, as happening during the
300 monsoon seasons, are consequently neglected.

301 On anoxic pixels, we represent anoxic soil COS flux with aThe production rate for anoxic soils is based on the
302 expression developed by Ogée et al. (2016),

$$303 P_{anoxic} = P_{ref} z_{max} Q_{10}^{\frac{(T - T_{ref})}{10}} \quad (18)$$

304 with P_{ref} ($\text{mol m}^{-2} \text{s}^{-2}$) the reference production term, T_{ref} a reference soil temperature (K) and Q_{10} the
305 multiplicative factor of the production rate for a 10 °C increase in soil temperature (unitless). As anoxic soil
306 production ranges from 10 to 300 $\text{pmol m}^{-2} \text{s}^{-1}$ for salt marshes and is usually below 10 $\text{pmol m}^{-2} \text{s}^{-1}$ for freshwater
307 wetlands (Whelan et al., 2018), the reference production term was set to 10 $\text{pmol m}^{-2} \text{s}^{-1}$.

308 All the variables and constants of the empirical and mechanistic models are presented in Appendix A Tables A3
309 and A4.

310 2.1.3 The atmospheric chemistry transport model LMDZ

311 To simulate the COS atmospheric distribution, we use an “offline” version of the Laboratoire de Météorologie
312 Dynamique General Circulation Model (GCM), LMDZ 6 (Hourdin et al., 2020), which has been used as the
313 atmospheric component in the IPSL Coupled Model for CMIP6. The LMDZ GCM has a spatial resolution
314 $3.75^\circ \text{long} \times 1.9^\circ \text{lat}$. with 39 sigma-pressure layers extending from the surface to about 75 km, corresponding to a
315 vertical resolution of about 200-300 m in the planetary boundary layer, and a first level at 33 m above sea or
316 ground level. The model u and v wind components were nudged towards winds from ERA5 reanalysis with a
317 relaxation time of 2.5 hours to ensure realistic wind advection (Hourdin and Issartel, 2000; Hauglustaine et al.,
318 2004). The ECMWF fields are provided every 6 hours and interpolated onto the LMDZ grid. This version has
319 been shown to reasonably represent the transport of passive tracers (Remaud et al., 2018). The off-line model uses
320 pre-computed mass-fluxes provided by this full LMDZ GCM version and only solves the continuity equation for
321 the tracers, which significantly reduces the computation time. In the following, we refer to this offline version as
322 LMDZ. The model time step is 30 minutes, and the output concentrations are 3-hourly averages.

323 The atmospheric COS oxidation is computed from pre-calculated OH monthly concentration fields produced from
324 a simulation of the INCA (Interaction with Chemistry and Aerosols) model (Folberth et al., 2006; Hauglustaine et
325 al., 2004, 2014) coupled to LMDZ. The atmospheric OH oxidation of COS amounts to 100 GgS yr^{-1} in the model.
326 Similarly, the COS photolysis rates are also pre-calculated with the INCA model, which uses the Troposphere
327 Ultraviolet and Visible (TUV) radiation model (Madronich et al., 2003) adapted for the stratosphere (Terrenoire
328 et al., in prep.). The temperature-dependent carbonyl sulfide absorption cross-sections from 186.1 nm to 296.3 nm
329 are taken from (Burkholder et al., 2019). The calculated photolysis rates are averaged over the period 2008-2018
330 and prescribed to LMDZ. Implemented in LMDZ, the COS photolysis in the stratosphere amounts to about 30

331 GgS yr⁻¹, which of the same order of magnitude as previous estimates: 21 GgS yr⁻¹ (71% of 30 GgS yr⁻¹) by Chin
332 and Davis (1995), between 11 GgS yr⁻¹ and 21 GgS yr⁻¹ by Kettle et al. (2002) and between 16 GgS yr⁻¹ and 40
333 GgS yr⁻¹ by Ma et al. (2021).

334 2.2 Observation data sets

335 2.2.1 Description of the sites

336 The description of the studied sites is given in Table 1.

337 2.2.2 Soil COS flux determination at selected sites

338 Soil COS flux chamber measurements were conducted in 2015 at AT-NEU, in 2016 at DK-SOR, ES-LMA and
339 ET-JA, and in 2017 at IT-CRO (abbreviations as in Table 1). The aboveground vegetation was removed one day
340 before the measurements if needed and the fluxes were derived from concentration measurements using a Quantum
341 Cascade Laser (see Kitz et al., 2020 and Spielmann et al., 2020, 2019). At AT-NEU, DK-SOR, ES-LMA and IT-
342 CRO, a Random Forest model was calibrated against the manual chamber measurements, and then used to simulate
343 half-hourly soil COS fluxes in Spielmann et al. (2019). We compared the ORCHIDEE half-hourly simulated fluxes
344 to half-hourly outputs of the Random Forest model. This enabled to study the diel cycle, and to compute daily
345 observations with no sampling bias for the study of the seasonal cycle. Soil COS fluxes for ET-JA were derived
346 by using the same training method ~~than-as~~ the one used in Spielmann et al. (2019).

347 At FI-HYY, soil COS fluxes were measured using two automated soil chambers in 2015. These chambers were
348 connected to a quantum cascade laser spectrometer to calculate soil COS fluxes from concentration measurements
349 (see Sun et al. (2018) for more information on the experimental setup). ~~Any vegetation was removed from the~~
350 ~~chambers before the measurements.~~

351 At US-HA, soil COS fluxes ~~in 2012 and 2013~~ were not directly measured but derived ~~from flux-profile~~
352 ~~measurements, connected to CO₂ soil chamber measurements and profiles, eddy-covariance COS and CO₂~~
353 ~~measurements and soil chamber CO₂ measurements conducted in 2012 and 2013.~~ A sub-canopy flux gradient
354 approach was used to partition canopy uptake from soil COS fluxes. For more information on this approach and
355 its limitations, see Wehr et al. (2017).

356 In the study of soil COS fluxes, the difficulty of performing soil COS flux measurements must be acknowledged,
357 as well as the differences between experimental setups and methods to retrieve soil COS fluxes. These limitations
358 are illustrated in the set of observations selected here. Aboveground vegetation had to be removed at some sites to
359 not measure the plant contribution in addition to soil COS fluxes (Sun et al., 2018; Spielmann et al., 2019; Kitz et
360 al., 2020). Vegetation removal prior to the measurements might lead to artefacts in the observations. Some
361 components of the measuring system can also emit COS. In this case, a blank system is needed to apply a post-
362 correction to the measured fluxes (Sun et al., 2018; Kitz et al., 2020). Litter was left in place at the measurement
363 sites.

364 2.2.3 COS concentrations at the NOAA/ESRL sites

365 The NOAA surface flask network provides long-term measurements of the COS mole fraction at 14 locations at
366 weekly to monthly frequencies from the year 2000 onwards. We use an extension of the data initially published in
367 Montzka et al. (2007). The data were collected as paired flasks analyzed using gas chromatography and mass

368 spectrometry. The stations located in the northern Hemisphere sample air masses coming from the entire northern
369 hemisphere domain above 30 degrees. Among them, the sites LEF, NWR, HFM, WIS have a mostly continental
370 footprints (Remaud et al., 2021) while the sites SPO, CGO, PSA sample mainly oceanic air masses of the southern
371 hemisphere (Montzka et al., 2007). The locations of these sites are depicted in Appendix B, Fig. B1.

372 **2.3 Simulations**

373 **2.3.1 Spin-up phase**

374 A “spin-up” phase was performed before each simulation, which enabled all carbon pools to stabilize and the net
375 biome production to oscillate around zero. Reaching the equilibrium state is accelerated in the ORCHIDEE LSM
376 thanks to a pseudo-analytical iterative estimation of the carbon pools, as described in Lardy et al. (2011). For site
377 simulations, the spin-up was performed by cycling the years available in the forcing files of each site, for a total
378 of about 340 years. For global simulations, the spin-up phase of 340 years was performed by cycling over 10 years
379 of meteorological forcing files in the absence of any disturbances.

380 **2.3.2 Transient phase**

381 Following the spin-up phase we ran a transient simulation of about 40 years that introduced disturbances such as
382 climate change, land use change and increasing CO₂ atmospheric concentrations.

383 This transient phase was performed by cycling over the available years for site simulations. For global simulations,
384 the transient phase was run where we introduced disturbances from 1860 to 1900. After this transient phase, COS
385 fluxes were simulated from 1901 to 2019.

386 **2.3.3 Atmospheric simulations: sampling and data processing**

387 We ran the LMDZ6 version of the atmospheric transport model described above for the years 2009 to 2016. We
388 started from a uniform initial condition and we remove the first year as it is considered to be part of the spin-up
389 period. The ~~prescribed~~ COS fluxes used as model inputs are presented in [Table 2-2](#). The fluxes are given as a lower
390 boundary condition, called the surface, of the atmospheric transport model (LMDZ), which then simulates the
391 transport of COS by large-scale advection and sub-grid scale processes such as convection and boundary layer
392 turbulence. In this study, we only evaluate the sensitivity of the latitudinal gradient and seasonal cycle of COS
393 concentrations to the soil COS fluxes. The horizontal gradient aims at validating the latitudinal repartition of the
394 surface fluxes, while the seasonal cycle partly reflects the seasonal exchange with the terrestrial sink, which peaks
395 in spring/summer. This study does not aim at reproducing the mean value as the top-down COS budget is currently
396 unbalanced, with a source component missing (Whelan et al., 2018; Remaud et al., 2022, and see [Table Table](#)
397 [53](#)).

398 For each COS observation, the ~~3D3DD~~ simulated concentration fields were sampled at the nearest grid point to
399 the station and at the closest hour of the measurements. For each station, the curve fitting procedure developed by
400 the NOAA Climate Monitoring and Diagnostic Laboratory (NOAA/CMDL) (Thoning et al., 1989) was applied to
401 modelled and observed COS time series to extract a smooth detrended seasonal cycle. We first fitted a function
402 including a first-order polynomial term for the growth rate and two harmonic terms for seasonal variations. The
403 residuals (raw time series minus the smooth curve) were fitted using a lowpass filter with either 80 or 667 ~~days~~

a mis en forme : Anglais (Royaume-Uni)

a mis en forme : Justifié

404 as short-term and long-term cut-off values. The detrended seasonal cycle is defined as the smooth curve (full
 405 function plus short-term residuals) minus the trend curve (polynomial plus long-term residuals). Regarding
 406 vegetation COS fluxes (Maignan et al., 2021), we added the possibility to use spatially and temporally varying
 407 atmospheric COS concentrations, as for soil.

408 2.4 Numerical methods for model evaluation and parameter optimisation

409 2.4.1 Statistical scores

410 We evaluated modelled soil COS fluxes against field measurements using the Root Mean Square Deviation
 411 (RMSD):

$$412 \text{RMSD} = \sqrt{\frac{\sum_{n=1}^N (F_{\text{COS}}^{\text{Obs}}(n) - F_{\text{COS}}^{\text{Mod}}(n))^2}{N}} \quad (19)$$

413 where N is the number of considered observations, $F_{\text{COS}}^{\text{Obs}}(n)$ is the n th observed COS flux and $F_{\text{COS}}^{\text{Mod}}(n)$ is the n th
 414 modelled COS flux, and the relative RMSD (rRMSD):

$$415 \text{rRMSD} = \frac{\text{RMSD}}{\frac{\sum_{n=1}^N F_{\text{COS}}^{\text{Obs}}(n)}{N}} \quad (20)$$

416 which is the RMSD divided by the mean value of observations.

417 Simulated atmospheric COS concentrations were evaluated by computing the normalized standard deviations
 418 (NSDs), which is the standard deviation of the simulated concentrations divided by the mean of the observed
 419 concentrations, and the Pearson correlation coefficients (r) between simulated and observed COS concentrations.

420 The closer NSD and r values are to 1, the better the model accuracy is.

422 2.4.2 Data assimilation

423 One of the main difficulties with the implementation of a model is to define the parameter values that lead to the
 424 most accurate representation of the processes in ORCHIDEE. Calibrating the model parameters is of interest as
 425 Ogée et al. (2016) indicate that some of the model parameters such as f_{CA} and the production term parameters have
 426 to be constrained by observations. Moreover, the default values for the soil COS model parameters used in this
 427 study (Appendix A Tables A1 and A2) are determined by laboratory experiments (Ogée et al., 2016; Whelan et
 428 al., 2016), that is why it is interesting to study how the values obtained by calibration against field observations
 429 differ from these default values. Data assimilation (DA) aims at producing an optimal estimate by combining
 430 observations and model outputs. In this study, we used ~~data-assimilation~~DA to find the model parameter values
 431 that improve the fit between simulated and observed soil COS fluxes from the empirical and the mechanistic
 432 models. We used the ORCHIDEE ~~Data Assimilation A~~-System (ORCHIDAS), which is based on a Bayesian
 433 framework. ORCHIDAS has been described in detail in previous studies (Bastrikov et al., 2018; Kuppel et al.,
 434 2014; MacBean et al., 2018; Peylin et al., 2016; Raoult et al., 2021), so below we only briefly present the method.
 435 Assuming that the observations and model outputs follow a Gaussian distribution, we aim at minimizing the
 436 following cost function $J(x)$ by optimizing the model parameters (Tarantola, 2005),

$$437 J(x) = \frac{1}{2} [(M(x) - y)^T \cdot E^{-1} \cdot (M(x) - y) + (x + x^b)^T \cdot B^{-1} \cdot (x + x^b)] \quad (21)$$

438 with x the vector of parameters to optimize and y the observations. The first part of the cost function measures the
439 mismatch between the observations and the model, and the second part represents the mismatch between the prior
440 parameter values x^b and the considered set of parameters x . Both terms of the cost function are weighted by the
441 prior covariance matrices for the observation errors E^{-1} and parameter errors B^{-1} . The minimization of the cost
442 function follows the genetic algorithm (GA) method, which is derived from the principles of genetics and natural
443 selection (Goldberg, 1989; Haupt and Haupt, 2004) and is described for ORCHIDAS in Bastrikov et al. (2018).
444 For each soil COS model, we selected the 8 most important parameters to which soil COS fluxes are sensitive
445 following sensitivity analyses (Sect. 2.4.3). The observation sites selected for sensitivity analyses and DA are the
446 ones with the largest number of observations for model parameter calibration, which are FI-HYY and US-HA.

448 2.4.3 Sensitivity analyses

449 We conducted sensitivity analyses at two contrasting sites (FI-HYY and US-HA) to determine which model
450 parameters have the most influence on the simulated soil COS fluxes from the empirical and the mechanistic
451 models. Sensitivity analyses can help to identify the key parameters before aiming at calibrating these parameters.
452 Indeed, focusing on the key model parameters for calibration limits both the computational cost of optimization
453 that increases with the number of parameters and the risk of overfitting.

454 The Morris method (Morris, 1991; Campolongo et al., 2007) was used for the sensitivity analysis as it is relatively
455 time-efficient and enables ranking the parameters by importance. This qualitative method requires only a small
456 number of simulations, $(p+1)n$, with p the number of parameters and n the number of random trajectories generated
457 (here, $n=10$).

458 We selected a set of parameters for the Morris sensitivity analyses based on previous sensitivity analyses conducted
459 on soil parameters in ORCHIDEE (Dantec-Nédélec et al., 2017; Raoult et al., 2021; Mahmud et al., 2021). A
460 distinction is made between the soil COS model parameters called first-order parameters (f_{CA} , α and β for the
461 mechanistic model and k_{soil} for the empirical model), and parameters called second-order parameters related to
462 soil hydrology, carbon uptake and allocation, phenology, conductance, or photosynthesis (18 parameters, see
463 Tables S3 and S4). The range of variation of the second-order parameters are described in previous studies using
464 ORCHIDEE (Dantec-Nédélec et al., 2017; Raoult et al., 2021; Mahmud et al., 2021). For the first-order
465 parameters, the range of variation is described in Yi et al. (2007) for k_{soil} (± 1.08 pmol COS μmol^{-1} CO₂) and in
466 Table 1 in Meredith et al. (2019) for f_{CA} . The ranges of variation for α and β parameters are not directly given in
467 the literature and were calculated based on information from the production parameters defined in Meredith et al.
468 (2018) (Text S1 and Table S5).

469 3 Results

470 3.1 Site scale COS fluxes

471 3.1.1 Soil COS flux seasonal cycles

472 Figure 2 shows the seasonal cycles of soil COS fluxes at the different sites where measurements were conducted.
473 The empirical model mainly differs from the mechanistic model with a stronger seasonal amplitude of soil COS
474 fluxes (34% higher), except at the sites where a net COS production is found with the mechanistic model in summer
13

a mis en forme : Justifié

475 (ES-LMA and IT-CRO). At all sites, the empirical model shows that the simulated uptake increases in spring
476 reaching a maximum in summer, and decreases in autumn with a minimal uptake during winter. The strong COS
477 uptake in summer from the empirical model can be explained by the proportionality of soil COS uptake to
478 simulated soil respiration, which increases with the high temperatures in summer. In contrast, the mechanistic
479 model depicts almost no seasonality at all the sites where no net COS production is found over the year. As the
480 mechanistic model represents both soil COS uptake and production, the increase in COS production due to higher
481 temperature in summer compensates part of the COS uptake (Appendix C Figure C1). While the uptake from the
482 empirical model is often higher than the one computed with the mechanistic model in summer, soil COS uptake
483 in winter is stronger with the mechanistic representation.

484 The scarcity of field measurements at AT-NEU, ES-LMA, IT-CRO, DK-SOR and ET-JA does not allow an
485 evaluation of the simulated seasonality of COS fluxes. However, at US-HA, the absence of seasonality from May
486 to October in the observations is also found in the mechanistic model, while a maximum net soil COS uptake is
487 reached with the empirical model.

488 We found that the mechanistic model is in better agreement with the observations for 4 (IT-CRO, ET-JA, FI-HYY,
489 US-HA) out of the 7 sites (Table 3), with a mean of $1.58 \text{ pmol m}^{-2} \text{ s}^{-1}$ and $2.03 \text{ m}^{-2} \text{ s}^{-1}$ for the mechanistic and
490 empirical model, respectively. However, the mechanistic model struggles to reproduce soil COS fluxes at AT-
491 NEU and ES-LMA, with an overestimation of soil COS uptake or an underestimation of soil COS production at
492 AT-NEU and a delay in the simulated net COS production at ES-LMA. We might suspect that the removal of
493 vegetation at these sites prior to the measurements could have artificially enhanced COS production in the
494 observations. Indeed, the removal of vegetation could change soil structure and increase the availability of soil
495 organic matter to degradation (Whelan et al., 2016). AT-NEU and ES-LMA are grassland sites for which soils are
496 expected to receive higher light intensity than forest soils. These sites also show a high mean soil temperature of
497 about 20°C during the measurement periods. Therefore, high soil temperature and light intensity on soil surface
498 could enhanced soil COS production as it was related to thermal or photo degradation of soil organic matter (Kitz
499 et al., 2017, 2020; Whelan et Rhew, 2015; Whelan et al., 2016, 2018). This is not the case at FI-HYY, ET-JA or
500 DK-SOR, where soil temperature is much lower (mean value about 10°C at FI-HYY and 15°C at ET-JA and DK-
501 SOR during the measurement periods) and the forested cover decreases the radiation level reaching the soil. Note
502 that herbaceous biomass is also likely to be higher in grasslands than in forests. Besides, AT-NEU and ES-LMA
503 are managed grassland sites with nitrogen inputs. Then, soil COS production could also be enhanced by a high
504 nitrogen content as suggested by several studies (Kaisermann et al., 2018; Kitz et al., 2020; Spielmann et al., 2020),
505 which is not represented in our models. The mechanistic model is able to represent a net COS production at IT-
506 CRO but overestimates it. This might highlight the importance of adapting the production parameters (α and β)
507 in this model to adequately represent a net COS production. In this model, the net soil COS production is related
508 to an increase in soil temperature. However, it is to be noted that IT-CRO is an agricultural site with nitrogen
509 fertilization. Therefore, soil COS production in the observations could also be enhanced by nitrogen inputs. As
510 expected, the empirical model is unable to correctly simulate the direction of the observed positive soil COS
511 exchange rates at ES-LMA and IT-CRO.

512 3.1.2 Soil COS flux diel cycles

513 Figure 3 shows the comparison between the simulated and observed mean diel cycles over a month. The
514 observations show a minimum net soil COS uptake or a maximum net soil COS production reached between 11
515 am and 1 pm at AT-NEU, ES-LMA, IT-CRO and DK-SOR. ~~A minimum net soil COS uptake is also observed at~~
516 ~~US-HA but in the afternoon.~~ At AT-NEU and ES-LMA, neither model is able to represent the observed diel cycle.
517 ~~At these grassland sites, Spielmann et al. (2020) and Kitz et al. (2020) found that the daytime net COS emissions~~
518 ~~were mainly related to high radiations reaching the soil surface, which impact is not represented in the soil COS~~
519 ~~models.~~ At IT-CRO ~~and~~ DK-SOR ~~and US-HA~~, the diel cycles simulated by the mechanistic model show patterns
520 similar to the observations with a peak in the middle of the day, but with an overestimation of the net soil COS
521 production and a delay in the peak at IT-CRO, and an overestimation of the net soil COS uptake at DK-SOR. The
522 mechanistic model reproduces the absence of a diel cycle observed at FI-HYY ~~and ET-JA.~~ ~~Small diel variations~~
523 ~~are observed at ET-JA, which are also captured by the mechanistic model~~ but with an underestimation of the net
524 soil COS uptake ~~at ET-JA.~~ ~~AT US-HA, the observed soil COS flux does not exhibit diel variations while the~~
525 ~~mechanistic model shows a peak with a decrease of the net soil COS uptake around 3 pm. Wehr et al. (2017)~~
526 ~~explain this absence of diel cycle in the observations by a range of variations for soil temperature and soil water~~
527 ~~content that is too low to influence soil COS flux. In ORCHIDEE, the simulated range of temperature at US-HA~~
528 ~~is larger than the one measured on site and temperature is the main driver of the decrease in net soil COS uptake~~
529 ~~at this site (not shown). Therefore, the enhancement of soil COS production by soil temperature could be only~~
530 ~~found in the simulated flux, or it could be totally compensated by soil COS uptake in the observations. Therefore,~~
531 ~~the enhancement of soil COS production by soil temperature could be only found in the simulated flux. Another~~
532 ~~possibility is that, or it could be totally compensated by soil COS uptake in the observations. The mismatch~~
533 ~~between the model and the observations could be due to several factors including: i) an insufficient representation~~
534 ~~of the vegetation complexity by the division in PFTs; ii) a poor calibration of the PFT-specific parameters ($f_{CA}, \alpha,$~~
535 ~~β); or iii) missing processes in the model, such as considering the effect of nitrogen content on soil COS fluxes.~~
536 ~~As the mechanistic model includes PFT-specific parameters (f_{CA}, α, β), we can think that these parameters would~~
537 ~~need to be calibrated to improve the model performance at the site scale.~~ The empirical model shows a maximum
538 soil COS uptake around 3 pm at ET-JA, FI-HYY, US-HA and IT-CRO, which is not found in the observations at
539 FI-HYY and is in contradiction with the observed diel variations at IT-CRO and ES-LMA. Considering all sites,
540 the mechanistic model leads to a smaller error between the simulations and the observations, with a mean RMSD
541 of $1.38 \text{ pmol m}^{-2} \text{ s}^{-1}$ against $1.87 \text{ pmol m}^{-2} \text{ s}^{-1}$ for the empirical model (Table 4).

542

543 3.1.3 Dependency on environmental variables

544 Figure 4 represents simulated net soil COS fluxes versus soil temperature and soil water content at the different
545 sites. At the sites where only a net soil COS uptake is simulated by the mechanistic model (all sites except IT-
546 CRO and ES-LMA), soil COS uptake ~~globally-generally~~ decreases with increasing soil water content, which
547 appears to be the main driver of soil COS fluxes. This behaviour can be explained by a decrease in COS diffusivity
548 through the soil matrix with increasing soil moisture, reducing soil COS availability for microorganism
549 consumption. Furthermore, an optimum soil water content for net soil COS uptake is found between 10% and
550 15% ~~, which was also observed, %-%. This optimum soil moisture is also represented~~ in Ogée et al. (2016) and was

15

a mis en forme : Justifié

551 ~~described~~ in several field studies to be around 12% (Kesselmeier et al., 1999; Liu et al., 2010; van Diest and
552 Kesselmeier, 2008). ~~This~~~~The~~~~The~~ optimum soil water content for soil COS uptake is related to a site-specific
553 temperature optimum, which is found between 13°C and 15°C at US-HA for example. Indeed, Ogée et al. (2016)
554 also describe a temperature optimum ~~Similarly, a temperature optimum was described in Ogée et al. (2016) and in empirical~~
555 ~~studies with a nanan optimum value value~~ that also depends on the studied site (Kesselmeier et al., 1999; Liu et al.,
556 2010; van Diest and Kesselmeier, 2008). At IT-CRO and ES-LMA where a strong net soil COS production is
557 simulated by the mechanistic model, the main driver of soil COS fluxes becomes soil temperature. At these sites,
558 the net soil COS production increases with soil temperature, due to the exponential response of soil COS
559 production term to soil temperature. The increase in soil COS production with soil temperature at IT-CRO and
560 ES-LMA is supported by the observations (Figure S1).
561 Contrary to the mechanistic model, soil COS uptake computed with the empirical model is mainly driven by soil
562 temperature, with a soil COS uptake that increases with increasing soil temperature. This response of the empirical
563 model to soil temperature is due to its relation to soil respiration, which is enhanced by strong soil temperature.
564 ~~However, this net increase in soil COS uptake with soil temperature at all sites is not found in the observations~~
565 (Figure S1). ~~However~~~~It can be noted that~~ ~~However~~ ~~However~~, low soil moisture values were found to limit soil COS
566 uptake for the empirical model, as seen at ES-LMA for a soil water content below 8%.

567 3.1.4 Sensitivity analyses of soil COS fluxes to parameterization

568 Sensitivity analyses including a set of parameters (19 for the empirical model and 21 for the mechanistic model)
569 were performed to evaluate the sensitivity of soil COS fluxes to each of the selected parameter. The Morris scores
570 were normalised by highest values to help rank the parameters by their relative influence on soil COS fluxes, a
571 score of 1 represents the most important parameter and 0 represents the parameters that have no influence on soil
572 COS fluxes. For reasons of clarity, in the following we present the results only for the parameters that were found
573 to have an impact on soil COS fluxes (Morris scores not equal to 0).

574
575 Figure 5 shows the results of the Morris sensitivity experiments highlighting the key parameters influencing soil
576 COS fluxes from the empirical and the mechanistic models at FI-HYY and US-HA. For the empirical model at
577 both sites, the first order parameter (k_{soil}) is the most important parameter in the computation of soil COS fluxes,
578 as it directly scales soil respiration to soil COS fluxes. The following parameters to which soil COS fluxes are the
579 most sensitive are the scalar on the active soil C pool content (soilC) and the temperature-dependency factor for
580 heterotrophic respiration (soil_Q10). Indeed, the soilC parameter determines the soil carbon active pool content,
581 which can be consumed by soil microorganisms during respiration, therefore impacting soil COS fluxes from the
582 empirical model. soil_Q10 impacts soil COS fluxes at both sites as it determines the response of soil heterotrophic
583 respiration to temperature, which is included in the proportionality of soil COS fluxes to the total soil respiration
584 in the empirical model. Similarly, one of the second order parameters, the minimum soil wetness to limit the
585 heterotrophic respiration (min_SWC_resp), has an impact on soil COS fluxes from the empirical model only. The
586 importance of min_SWC_resp for soil COS fluxes is found at US-HA but not at FI-HYY. This can be explained
587 by the difference in soil moisture between the two sites, with an annual mean of 16.2% at US-HA and reaching a
588 minimum of only 8.8%, against an annual mean of 17.5% with a minimum of 12.4% at FI-HYY.

589 Contrary to the empirical model, soil COS fluxes computed with the mechanistic model are more sensitive to two
590 second-order parameters, the Van Genuchten water retention curve coefficient n (n) and the saturated volumetric
591 water content (θ_{SAT}). These two second-order parameters are strongly linked to soil hydrology and determine the
592 soil water content, which affects COS diffusion through the soil matrix and its uptake. The Van Genuchten
593 coefficients occur in the relationships linking hydraulic conductivity and diffusivity to soil water content (van
594 Genuchten, 1980). At both sites, the strong impact of the Van Genuchten water retention curve coefficient n on
595 soil COS fluxes simulated with the mechanistic model highlights the critical importance of soil architecture. Thus,
596 soil COS fluxes computed with the mechanistic model are expected to strongly vary according to the different soil
597 types. Then, the first-order parameters (f_{CA} , α and β) also influence soil COS fluxes from the mechanistic model.
598 However, the uptake parameter (f_{CA} of PFT 15, boreal C_3 grass) has the most influence on soil COS fluxes at FI-
599 HYY, while it is the production-related parameter (α of PFT 6, temperate broadleaved summergreen forest) that
600 has the largest impact at US-HA. The stronger influence of the production parameter involved in the temperature
601 response at US-HA might be explained by the difference of temperature between the two sites, which ranges from
602 -10°C to 25°C at US-HA with an annual mean of 7.5°C in 2013, while only ranging from -5°C to 15°C with an
603 annual mean of 4.3°C at FI-HYY in 2015. Similar to the difference in the main driver of soil COS fluxes found in
604 Fig. 4, the most important first-order parameters to which soil COS fluxes are sensitive seem to differ between
605 uptake and production parameters depending on the site conditions. It is to be noted that at US-HA, the most
606 important production parameters are the ones of the dominant PFT at this site (PFT 6), which also correspond to
607 a stronger response of the production term to temperature than for PFT 10 (temperate C_3 grass). However, at FI-
608 HYY the most influential uptake parameter is for PFT 15 (boreal C_3 grass) that only represents 20% of the PFTs
609 at this site while PFT 7 (boreal needleleaf evergreen forest) is the dominant PFT. This can be explained by the
610 range of variation that is assigned to f_{CA} of PFT 7 by Meredith et al. (2019), which is larger than the one of f_{CA} for
611 PFT 15 (9000 against 3100).

612 Finally, a set of parameters related to photosynthesis, conductance, phenology, hydrology, and carbon uptake has
613 an impact on soil COS fluxes computed with both the empirical and the mechanistic models at the two sites. The
614 specific leaf area (SLA), maximum rate of Rubisco activity-limited carboxylation at 25°C (V_{cmax25}), residual
615 stomatal conductance (g_0) and minimum photosynthesis temperature (T_{min}) have an impact on soil COS fluxes
616 as they also indirectly affect soil moisture through their influence on transpiration and stomatal opening. The
617 second-order parameters related to soil hydrology (a , K_s , Z_{root} , θ_{WP} , θ_{FC} , θ_R , θ_{Transp_max}) impact the soil
618 water availability, which affects soil respiration for the empirical model and soil COS diffusion and uptake in the
619 mechanistic model. For example, the parameter for root profile (Z_{root}) determines the density and depth of the
620 roots, and therefore how much water can be taken up by roots.

621 3.1.5 Soil COS flux optimization

622 Figure 6 presents soil COS fluxes before and after optimization of the model parameters to better fit the
623 observations at FI-HYY and US-HA. For the mechanistic model, the optimization at the two sites mainly changes
624 the mean value of soil COS fluxes, by reducing the net uptake at US-HA and increasing it at FI-HYY. Similar to
625 the mechanistic model optimization, the posterior soil COS uptake computed with the empirical model is enhanced
626 at FI-HYY and reduced at US-HA. However, at US-HA, the increase in soil COS uptake is only found between
627 April and October, while the winter soil COS fluxes are not impacted by the optimization. Using the optimized

628 parameterization improves the RMSD by 7% and 5% at US-HA and by 23% and 25% at FI-HYY for the
629 mechanistic and the empirical model, respectively. While it leads to similar posterior RMSD values between the
630 two models at US-HA, the optimization of the mechanistic model gives a lower RMSD than the empirical model
631 at FI-HYY, with $0.54 \text{ pmol m}^{-2} \text{ s}^{-1}$ against $0.95 \text{ pmol m}^{-2} \text{ s}^{-1}$.

632 At FI-HYY, the difference between prior and posterior soil COS fluxes from the empirical model seems to mainly
633 come from the change in soil_Q10 value (Appendix E, Figure E1). soil_Q10 value drops from 0.83 to 0.53, which
634 corresponds to a prior Q10 value of 2.29 versus a posterior value of 1.70, decreasing the heterotrophic respiration
635 response to soil temperature. Soil COS fluxes computed with the empirical model were found to be strongly
636 sensitive to soil_Q10 (Figure 5). The posterior value of this parameter has nearly attained the lower bound of its
637 variation range. Since the range of variation represents the realistic values this parameter can take, we need to be
638 careful about the fact that this parameter is trying to take values close to, or potentially beyond, these meaningful
639 values. Furthermore, the optimization deviates the Q10 value at FI-HYY from the ones calculated in the
640 observations over the measurement period (3.0 for soil chamber 1 and 2.5 for soil chamber 2). We could assume
641 that k_{soil} should be defined as temperature-dependent for linking soil COS flux to soil respiration (Berkelhammer
642 et al., 2014; Sun et al., 2018), instead of being considered as a constant. Thus, the optimization of the empirical
643 model could in fact be aliasing the error of k_{soil} onto soil_Q10 because of the impossibility to account for the
644 temperature-dependence of soil COS to CO_2 uptake ratio (Sun et al., 2018). At US-HA, the optimization also leads
645 to a decrease of soil_Q10 but to a lesser extent, the parameter remaining comfortably within its range of variation.
646 For the mechanistic model, the optimization reduces the enhancement factor value (f_{CA}) for PFT 10 at US-HA and
647 increases the value of the production parameter α for the dominant PFT (PFT 6). This enhances the reduction in
648 net soil COS uptake, which was slightly overestimated with the prior model parameterization. At FI-HYY, the
649 optimized parameters show higher values of f_{CA} and of α for PFT 15, and of both production parameters (α and
650 β) for the dominant PFT (PFT 7). This increase in both soil COS uptake and production after optimization could
651 correspond to an attempt to better simulate the larger range of variation found in the observations compared to the
652 modelled fluxes.

653 Finally, the optimization also affects hydrology-related parameters for both models. However, while it improves
654 the simulated water content compared to the observations for the mechanistic model at the two sites (RMSD
655 decreases by 28% at FI-HYY and 22% at US-HA), it leads to a degradation at FI-HYY for the empirical model
656 (RMSD increases by more than 3 times~~not shown~~). Since the empirical model is quite a simplistic model with few
657 parameters, it relies on parameters from different processes to help better fit the observations – sometimes
658 degrading the fit to the other processes. The mechanistic model is able to both improve the fit to the COS
659 observations and soil moisture values implying its parameterization is more consistent.

660 This optimization experiment has been promising, highlighting how observations can be used to improve the
661 models. However, since we only optimized over two sites due to the scarcity of soil COS flux observations, for
662 the global scale simulations in the rest of this study, we will rely on the default parameter values of each
663 parameterization.

664

665 3.2 Global scale COS fluxes

666 3.2.1 Soil COS fluxes

667 The spatial distribution of oxic soil COS fluxes shows a net soil COS uptake everywhere except in India, in the
668 Sahel region and some areas in the tropical zone, where net soil COS production is simulated (Figure Figure-7a).
669 The strongest uptake rates are found in Western North and South America, and in China, with a mean maximum
670 uptake of $-4.4 \text{ pmol COS m}^{-2} \text{ s}^{-1}$ over 2010-2019. The difference in magnitude between the maximum uptake value
671 and the maximum of production can be noticed, with a net production reaching $67.2 \text{ pmol COS m}^{-2} \text{ s}^{-1}$ in the Sahel
672 region. India and the Sahel region, where oxic soil COS production is concentrated, are represented in ORCHIDEE
673 by a high fraction of C_3 and C_4 crops (Figure S3S3S3-S34). In the mechanistic model, crops are associated with
674 the lowest f_{CA} value due to overall lower fungal diversity and abundance in agricultural fields (Meredith et al.,
675 2019), and the strongest response of oxic soil COS production to temperature as observed by Whelan et al. (2016).
676 Thus, these PFT-specific parameters combined with high temperature in the tropical region can explain the net
677 oxic soil COS production found in these regions. C_3 crops are also dominant in China near the Yellow Sea (Figure
678 S3S3S3-S3S4). However, the mean soil temperature in this region is about 15°C lower than the mean soil
679 temperature in India, leading to a lower enhancement of soil COS production. The highest atmospheric COS
680 concentration is also found in this region with about 800 ppt (Figure S2S3S2-S2).). Indeed, recent inventories
681 have shown that China was related to strong anthropogenic COS emissions due to the industry, biomass burning,
682 coal combustion, agriculture, or vehicle exhaust (Yan et al., 2019; Zumkehr et al., 2018). High atmospheric COS
683 concentrations increase soil COS diffusion and uptake that can compensate part of soil COS production. The
684 highest values of soil COS fluxes for anoxic soils are located in northern India, with a mean maximum value
685 reaching $36.8 \text{ pmol COS m}^{-2} \text{ s}^{-1}$ (Figure Figure-7b). This region is characterized by rice paddies, which were also
686 associated with strong COS production in previous studies (Zhang et al., 2004).

687 The total soil COS fluxes (oxic and anoxic) computed with the mechanistic model (Figure Figure-7c) show a very
688 different spatial distribution than the one obtained with the empirical model (Figure Figure-7d). Soil COS fluxes
689 from the empirical model are on the same order of magnitude for net COS uptake than the mechanistic model,
690 with a mean maximum uptake of $-6.41 \text{ pmol COS m}^{-2} \text{ s}^{-1}$. However, most soil COS uptakes simulated by the
691 empirical model is located in the tropical region, where soil respiration is strong due to high temperature. The
692 distribution and magnitude of soil COS flux from the empirical approach is similar to the one presented in
693 Kooijmans et al. (2021) (see Figure S15 in the supplementary material of Kooijmans et al., 2021), when
694 implemented in SiB4. For the mechanistic model, the comparison of oxic soil COS flux distribution with the one
695 in SiB4 shows a net soil COS emission in India in both SiB4 and ORCHIDEE. However, the maximum oxic soil
696 COS flux is about $60 \text{ pmol m}^{-2} \text{ s}^{-1}$ higher in ORCHIDEE than in SiB4. The regions with the strongest net oxic soil
697 COS uptake also differ between SiB4 and ORCHIDEE as it is concentrated in the tropics in SiB4 and in Western
698 North and South America, and in China for ORCHIDEE.

699 The difference of soil COS fluxes between the mechanistic model and the empirical model ranges from -4.1 pmol
700 $\text{COS m}^{-2} \text{ s}^{-1}$ to $+68.0 \text{ pmol COS m}^{-2} \text{ s}^{-1}$ (Appendix D, Figure D1). Over western North and South America, northern
701 and southern Africa, western Asia, and eastern, northern and Central Asia, the net COS uptake from the
702 mechanistic model exceeds the uptake from the empirical model. On the contrary, soil COS uptake from the
703 empirical approach is higher than the net COS uptake simulated with the mechanistic model over Eastern North

a mis en forme : Police :(Par défaut) Times New Roman, 10 pt

a mis en forme : Police :(Par défaut) Times New Roman, 10 pt

a mis en forme : Police :(Par défaut) Times New Roman, 10 pt

a mis en forme : Police :(Par défaut) Times New Roman, 10 pt

a mis en forme : Justifié

704 and South America, Western, Central and Eastern Africa, and Indonesia. The absence of soil COS production
705 representation in the empirical approach leads to the strongest differences in India and in the Sahel region, reaching
706 +68.0 pmol COS m⁻² s⁻¹.

707 3.2.2 Temporal evolution of the soil COS budget

708 We computed the mean annual soil COS budget over the period 2010-2019 using the monthly variable atmospheric
709 COS concentration and we compared its evolution to the variations of the mean annual atmospheric COS
710 concentration.

711
712 The evolution of the mean annual soil COS budget (Figure 8) shows small variations in the budget for oxic soils
713 computed with the mechanistic model between 2010 and 2015, with a net sink ranging from -133 GgS y⁻¹ to -124
714 GgS y⁻¹. Then, from 2016 we see a sharp decrease in this budget, which reaches -98 GgS y⁻¹ in 2019. This decrease
715 also corresponds to the decrease in atmospheric COS concentration observed between 2016 and 2019 with a loss
716 of 25 ppt in 3 years. ~~It is worth noting that other~~ Several monitoring stations recorded a drop in atmospheric COS
717 concentration over Europe, as for the GIF station with -42 ppt between 2015 and 2021 (updated after Belviso et
718 al., 2020). Note that the decrease in oxic soil COS budget computed with the mechanistic model is sharper than
719 the drop in atmospheric COS concentration because changes in oxic soil COS budget result from the combined
720 effect of decreasing atmospheric COS concentration and changes in the drivers of soil COS fluxes (i.e., changes
721 in soil temperature and water content during the 10-year period which are not homogeneously distributed around
722 the globe (not shown)). On the contrary, the soil COS net uptake computed with the empirical model slightly
723 increases from -212 GgS y⁻¹ in 2010 to -219 GgS y⁻¹ in 2019. As the empirical model defines soil^s COS flux as
724 proportional to the total soil respiration independently of atmospheric COS concentration, the budget obtained
725 with this model is not impacted by the variations observed in atmospheric COS concentration. The anoxic soil
726 COS budget follows soil temperature variations (not shown), with an increasing trend of about 0.17 GgS yr⁻¹ over
727 the studied period.

728 3.3 Transport and site-scale concentrations

729 Interhemispheric gradient

730 We transported total COS fluxes for the different configurations (i.e. including the soil fluxes but also other
731 components of the COS atmospheric budget, listed in [Table 2-2](#)) with the LMDZ6 atmospheric transport model as
732 described in Sect. 2.1.3. We analyzed COS concentrations derived from simulated COS fluxes obtained with the
733 mechanistic and two empirical approaches with regards to the COS concentrations observed at 14 NOAA sites
734 depicted in Appendix B, Fig. B1. Note that atmospheric mixing ratios of COS result from the transport of all COS
735 sources and sinks and that, due to other sources of errors (transport and errors in the other COS fluxes), the
736 comparison presented in the following should be taken as a sensitivity study of COS seasonal cycle and inter-
737 hemispheric gradient to the soil exchange fluxes rather than a complete validation of one approach or the other.
738 ~~Figure 9~~ Figure 9 shows the COS atmospheric concentrations at NOAA sites as a function of latitude for each
739 simulated soil flux and for the observations. Here as we want to focus on the latitudinal variations of atmospheric
740 COS mixing ratios, the atmospheric COS concentrations have been vertically shifted to have the same mean as the

741 observations. This means that the concentrations values cannot be compared at each site, we can only compare the
742 interhemispheric gradients of simulated and observed concentrations. The RMSD for the mechanistic model with
743 oxic soils only, the mechanistic model with oxic and anoxic soils, the empirical Berry model (with oxic soils only),
744 and the empirical Launois model (with oxic and anoxic soils) are 36.5, 39.4, 43.0, 51.0 ppt, respectively. While
745 the different approaches show similar gradient patterns in the southern latitudes, they lead to strong differences in
746 the simulated concentrations in the northern hemisphere. Compared to empirical approaches, the mechanistic
747 approach marginally improves the latitudinal distribution of the atmospheric mixing ratios by decreasing the
748 concentrations in the high latitudes. The lower atmospheric mixing ratios above 60 °N reflect the stronger soil
749 absorption in the mechanistic model (see Figure 9), where soil COS uptake is dominant and the compensation by
750 COS production is small (Appendix D, Figure D2). Despite this slight improvement, there are persistent biases as
751 overestimated concentrations at the high latitude sites ALT, BRW, SUM, and underestimated concentrations at
752 most tropical sites: WIS, MLO and SMO. These model-observation mismatches have led top-down studies to
753 identify ~~vegetation as an underestimated sink in the high latitudes (Ma et al., 2021; Remaud et al., 2022), and the~~
754 ~~missing source as being~~ the tropical oceanic emissions ~~as being the missing source~~ (Berry et al., 2013; Launois et
755 al., 2015; ~~Le Kuai et al. 2015; Ma et al. 2021; Remaud et al., 2022~~2022; Davidson et al., 2021). The present anoxic
756 soil fluxes have little impact on the surface latitudinal distributions and therefore are unlikely to shed new light on
757 the tropical missing source. An explanation for the small impact is that they are located outside areas experiencing
758 deep convection events (e.g. the Indian monsoon domain) and thus the surface concentrations are less sensitive to
759 these fluxes.

760 Seasonal cycle at NOAA sites

761 Figure 10 shows the detrended temporal evolution of COS concentrations for the mechanistic and empirical
762 approaches at Alert (ALT, Canada) and Harvard Forest (HFM, USA). Because of the mean westerly flow, the
763 HFM site is influenced by continental regions to the west (Sweeney et al., 2015), and is more sensitive to the soil
764 fluxes than other mid-latitude sites located to the west of the ocean (MHD, THD), see Fig. 1 in Remaud et al.
765 ~~(2022)~~2022). The ALT site samples air masses coming from high-latitude ecosystems (Peylin et al., 1999), but
766 also from regions further south due to atmospheric transport (Parazoo et al., 2011). The reader is referred to
767 Appendix B, Table B2 for the other sites. At both sites, the mechanistic approach tends to weaken the total seasonal
768 amplitude and increase the model-data ~~mismatch. mismatch. At HFM At ALT, the seasonal amplitude is marginally~~
769 ~~decreased, while at HFM it is divided by two. At ALT, BRW and SUM, the too high atmospheric concentrations~~
770 ~~and the too weak seasonal amplitude given by the mechanistic approach are consistent with an underestimated soil~~
771 ~~absorption at sites ET JA (Estonia) and FI HYY (Finland) (see Figure 2). As for Harvard Forest, since the~~
772 ~~mechanistic soil model shows overall good agreement with the observed soil fluxes (e.g. Figure 2) Figure 2), the~~
773 model-observation mismatch likely arises from errors in other components of the COS budget (in particular
774 oceanic and vegetation fluxes). Therefore, empirical approaches give a more realistic seasonality of atmospheric
775 concentrations for the wrong reasons, which likely hides an underestimated vegetation uptake. Indeed, as Maignan
776 et al. (2021) showed that the vegetation uptake magnitude in ORCHIDEE was consistent with measurements, the
777 introduction of variable atmospheric COS concentrations decreased the vegetation uptake, which as a result, is
778 very likely underestimated now. Moreover, the comparison between simulated and observed concentrations show
779 a degradation of the simulated concentrations in this study compared to Maignan et al. (2021). It is to be noted that
780 in addition to using a variable atmospheric COS concentration in this study, the transported ocean COS fluxes
781 21

a mis en forme : Justifié

781 from Masotti et al. (2016) and Lennartz et al. (2017, 2021) differ from the ones used in Maignan et al. (2021),
782 from Kettle et al. (2002) and Launois et al. (2015). These results illustrate the necessity of well constraining both
783 the soil and vegetation fluxes in order to optimize the GPP with the help of atmospheric inverse modelling.

784 4 Discussion

785 4.1 Soil budget

786 According to the mechanistic approach of this study, the COS budget for oxic soil is a net sink of -126 GgS yr⁻¹
787 over 2009-2016, which is close to the value of -130 GgS yr⁻¹ found by Kettle et al. (2002) (Table Table 35). This
788 net COS uptake by oxic soils is higher than the one found in SiB4 by Kooijmans et al. (2021) with -89 GgS yr⁻¹,
789 also based on the mechanistic model described in Ogée et al. (2016). In SiB4 and in ORCHIDEE, the mechanistic
790 model gives the lowest oxic soil COS net uptake compared~~The-meehanistic-model-gives-the-lowest-oxic-soil-COS~~
791 ~~net-uptake-compared~~ to all previous studies, which were -using empirical approaches. This budget is also 41%
792 lower than the one found with the Berry empirical approach in this study, with an uptake of -214 GgS yr⁻¹. The
793 anoxic soil COS budget computed with the mechanistic approach is +96 GgS yr⁻¹, which is close to the budget
794 found by Launois et al. (2015) of +101 GgS yr⁻¹ based on methane emissions. However, while COS emissions
795 from anoxic soils were only located in the northern latitudes in Launois et al. (2015), the COS production in this
796 study is also distributed in the tropical region. Thus, we can expect that despite similar budget values for anoxic
797 soils, the difference in flux distribution will impact the latitudinal gradient of COS fluxes. Finally, adding anoxic
798 soil COS budget to oxic soil COS budget results in a total soil COS budget of only -30 GgS yr⁻¹ for the mechanistic
799 approach.

800 When computing the net total COS budget considering all sources and sinks of COS (Table 2), the net total
801 from empirical we found that neglecting the potential COS production of oxic soils and COS emissions from anoxic
802 soils leads to an overestimation of COS sink or an underestimation of COS source to close the budget (-165 GgS
803 yr⁻¹). On the contrary, the total COS budget computed with the mechanistic soil model is closed given the
804 uncertainties on each component (Table 2). However, despite a closed budget, the mismatch between the observed
805 and simulated latitudinal gradients of atmospheric COS concentration highlights errors in COS flux component
806 distributions (Figure 9).

807 It ~~When computing the net total COS budget considering all sources and sinks of COS, the net total from the~~
808 ~~empirical approach is closer to zero (-35 GgS yr⁻¹) than the net total from the mechanistic model (+model~~
809 ~~(+model (+149 GgS yr⁻¹). In the empirical approach, neglecting the potential COS production of oxic soils and~~
810 ~~COS emissions from anoxic soils leads to a small overestimation of COS sink or underestimation of COS source~~
811 ~~to close the budget. On the contrary, the mechanistic approach leads to an overestimation of COS source or an~~
812 ~~underestimation of COS sink components. This positive net global budget could be due to an underestimation of~~
813 ~~vegetation COS uptake in the northern hemisphere, participating in the underestimation of the COS concentration~~
814 ~~drawdown (Figure 9), but the absence of anthropogenic emission seasonality could also play a role. The two net~~
815 ~~totals obtained in this study are closer to closing the COS budget than the previous approach from Launois et al.~~
816 ~~(2015).~~

a mis en forme : Police :(Par défaut) Times New Roman, 10 pt

a mis en forme : Justifié

817 ~~Despite a net COS budget closer to zero with the empirical model, it is also~~ to be noted that the mechanistic model
818 better simulates the lack of seasonality ~~in the soil COS flux~~ at US-HA compared to the empirical model (Figure
819 2). US-HA is represented by 80% of PFT6 (temperate broadleaved summergreen forest) and the absence of
820 seasonality by this PFT has also been reported at a mid-latitude site at Gif-sur-Yvette (Belviso et al., 2020). This
821 PFT is largely found in the temperate region such as in Europe and in the southern United-States. Moreover, NWR,
822 HFM and LEF stations are mainly influenced by COS exchanges from the PFT6. Therefore, the use of the
823 mechanistic model would be recommended to carry out new comparisons at these mid-latitude sites.

824 4.2 Variable atmospheric COS concentration versus constant atmospheric COS concentration

825 We studied the impacts of using a constant versus a variable atmospheric COS concentration on soil COS fluxes.
826 At the site-scale we found a distinction between the sites where soil COS production is strong (IT-CRO and ES-
827 LMA) and the sites mainly showing a net soil COS uptake. The impact of using a constant atmospheric COS
828 concentration is lower at IT-CRO and ES-LMA because the atmospheric COS concentration does not directly
829 impact the soil COS production term but participates in the net soil COS flux. Our study shows that at the sites
830 where a net soil COS uptake is dominant, using a constant atmospheric COS concentration leads to an
831 ~~underestimation of lower~~ soil COS flux in winter and an ~~overestimation higher of~~ soil COS flux from spring to
832 autumn (not shown). Indeed, during the growing season, plant uptake decreases atmospheric COS concentration
833 (Figure ~~S1S2+S1S1~~), which reduces COS availability for soil COS diffusion, whereas during winter, a higher
834 atmospheric COS concentration enhances COS diffusion into the soil.

835 At the global scale, as the variable atmospheric COS concentration used in this study shows a decrease of about
836 25 ppt in the recent years (Figure 8), considering a constant atmospheric COS concentration would not enable to
837 represent the impact of this strong variation on soil COS fluxes. When computing the soil COS budget over 2016
838 to 2019, we found a net uptake of -126 GgS yr⁻¹ with the mechanistic model using a constant atmospheric COS
839 concentration, against the -110 GgS yr⁻¹ computed with a monthly spatially variable concentration. Using a
840 constant atmospheric COS concentration would then lead to ~~an overestimation of about 13% of thea 13% higher~~
841 net soil COS uptake over the past 4 years.

842 We also studied the impact of considering a constant versus a variable atmospheric COS concentration on the
843 seasonal variations of mean monthly soil COS fluxes over 2010-2019, simulated with the mechanistic model (not
844 shown). We found that using a constant atmospheric COS concentration leads to an ~~overestimation increase~~ of net
845 soil COS uptake over the whole year in the southern latitudes and from June to February in the northern latitudes
846 (reaching 1.62 pmol m⁻² s⁻¹). This ~~overestimation increase is higher~~ over the regions with the lowest atmospheric
847 COS concentrations, which limits COS diffusion through the soil matrix. On the contrary when atmospheric COS
848 concentration is high in the northern latitudes between April and May, considering a constant atmospheric COS
849 concentration ~~leads to an underestimation of decreases the~~ net soil COS uptake. We notice that this ~~underestimation~~
850 ~~lower net soil COS uptake~~ with a constant atmospheric COS concentration can be found as early as March over
851 Europe, where atmospheric COS concentration is higher in this region. In eastern Asia, where atmospheric COS
852 concentration is higher than 800 ppt, the ~~underestimation decrease fin~~ the net soil COS uptake can reach -2.34
853 pmol m⁻² s⁻¹ when considering a constant atmospheric COS concentration.

854 It is to be noted that the modelled COS concentrations we used have their own uncertainty, which is however
855 smaller than their difference with the fixed value (Remaud et al., ~~20212021~~–~~20212022~~–~~2021~~).

856 4.3 Foreseen improvements

857 The mechanistic representation of soil COS fluxes was found to be in better agreement with the observations at
858 field sites. However, there can be strong differences between the simulated fluxes and the observations at some
859 sites, especially at AT-NEU and ES-LMA. In the mechanistic approach, the influence of light on soil COS fluxes
860 is not considered. Several field studies have reported light-induced emissions in oxic soils (Kitz et al., 2017;
861 Meredith et al., 2018; Spielmann et al., 2019; Whelan and Rhew, 2015), assumed to be related to the effect of light
862 on soil organic matter. Spielmann et al. (2019) related strong soil COS emissions during daytime to light at the
863 sites where direct solar radiations reached the surface, such as ES-LMA and AT-NEU. At these sites, the
864 mechanistic model was unable to represent the soil COS emission peak during daytime. The optimization we
865 performed showed that, as expected, adjusting the parameters to site observations improves the fit between the
866 simulated and observed fluxes. However, it is necessary to represent all important processes in the mechanistic
867 approach before calibrating the parameters. Thus, a next step in our modelling approach could be to include the
868 light influence on soil COS fluxes, which can be of major importance for the sites where radiations strongly affect
869 soil COS fluxes. ~~Mellillo and Steudler (1989). Several studies~~ also found that soil COS production could be related
870 to nitrogen content, which increases with nitrogen fertilizer application (Kaisermann et al., 2018; Meredith et al.
871 2018, 2019). ~~At the sites where soil is enriched with nitrogen inputs, such as agricultural fields or managed and
872 fertilized grasslands and forests, the fertilization~~ ~~Then crop management practices~~ ~~might would~~ also need to be
873 included when representing the dynamics of soil COS fluxes. ~~However, the soil nitrogen content and soil microbial
874 nitrogen biomass vary not only with fertilization, but also with location. Then, in addition to indications on land
875 use, information on the total soil nitrogen content should be included in the model to consider nitrogen impact on
876 soil COS flux. In the soil COS models, the impact of snow cover is also not represented. Indeed, due to the scarcity
877 of soil COS flux observations in winter and with snow cover, its effect on soil COS flux could not be implemented
878 in soil COS models yet. However, Helmig et al. (2009) found that COS uptake was not zero when soil is covered
879 by snow at Niwot Ridge, Colorado.~~

880 Moreover, one difficulty with the study of soil COS fluxes arises from the scarcity of field measurements that
881 could be used for ~~data assimilation. Therefore, more field measurements would help to build a larger field
882 observation database for model validation and calibration. Besides, the observation sites considered here are all
883 located in a small latitudinal range between 39°N and 62°N. Measurements in the tropics and in the Southern
884 hemisphere are needed. Especially, soil COS flux observations in Northern India could help to validate the net soil
885 COS production simulated in both SiB4 and ORCHIDEE.- In the tropical rainforest, soil COS flux measurements
886 were performed at La Selva Biological Station in Costa Rica (personal communication). In particular, ~~in the
887 tropical rainforest, soil COS flux measurements were performed at La Selva Biological Station in Costa Rica (Sun
888 et al., 2014). When available, these measurements could allow a first comparison between the observed and
889 simulated soil COS flux in a tropical region.~~~~

890 ~~Then, the characterization of the soil microbial community should also be addressed to improve the scaling of CA
891 content and activity, represented by the f_{CA} parameter (Meredith et al., 2019).~~

892 ~~The mechanistic model from Ogée et al. (2016) has also recently been implemented in the LSM SiB4 (Kooijmans
893 et al., 2021). The implementation of the soil COS flux mechanistic model from Ogée et al. (2016) in SiB4
894 (Kooijmans et al., 2021), the simulated soil COS fluxes with the mechanistic model shows a seasonal cycle with
895 a maximum net soil COS uptake in summer for the sites without crops, while the fluxes computed in ORCHIDEE~~

a mis en forme : Justifié

896 show almost no seasonality. The expression of the production term P differs between the two models, which is
897 based on Meredith et al. (2018) in SiB4 and on Whelan et al. (2016) in ORCHIDEE. The observation sites that are
898 common to the two studies (FI-HYY, US-HA, AT-NEU and DK-SOR) are also represented by different fractions
899 of biomes between SiB4 and ORCHIDEE, which changes the parameterization to compute soil COS fluxes.
900 Finally, the parameter values for the enhancement factor f_{CA} for grass differ as the value for tropical grass is also
901 assigned to C_3 and C_4 grass in SiB4. Soil COS flux field data are mainly available in summer, therefore having
902 field measurements over a whole year could better inform the seasonality of observed soil COS fluxes to compare
903 to the simulations.

904 The optimization does not modify the respective seasonality of both soil COS models, with a seasonal cycle that
905 agrees with the one of soil respiration for the empirical model and a lack of seasonality for the mechanistic model.

906 The lack of observations in winter does not enable to validate or constrain soil COS fluxes in winter. Therefore,
907 having field observations over a whole year could help to determine if both models could be calibrated with a
908 constrain over the whole year instead of only during summer and autumn. Moreover, the optimized set of
909 parameters for the empirical models leads to a degradation of the simulated soil water content compared to the
910 observations at FI-HYY, while the optimized parameters of the mechanistic model improve the representation of
911 soil water content at US-HA and FI-HYY. Thus, the mechanistic approach is to be preferred over the empirical
912 model and should be selected for future COS studies in ORCHIDEE.

913 The sensitivity analyses showed the importance of the hydrology-related parameters in the computation of soil
914 COS fluxes with the mechanistic model. Thus, assuming an accurate representation of soil COS fluxes, soil COS
915 fluxes could have the potential to add a new constraint on hydrology-related parameters.

916 In this work, soil COS fluxes are computed in the top 9 cm, which assumes that soil COS uptake and production
917 depend on the conditions in the first soil layers. Indeed, soil COS uptake depends on diffusive supply of COS from
918 the atmosphere. However, since soil COS production does not depend on COS supply, deeper soil layers could
919 also contribute to soil COS production. A study by Yang et al. (2019) presents COS profile measurements in an
920 orchard, which shows a non-zero COS concentration in deeper soil layers, but no direct evidence for attributing it
921 to soil COS production. Thus, we could consider deeper soil layers in the future to study the impact on soil COS
922 fluxes compared to considering only the top soil layers.

923 The anoxic soil map of regularly flooded wetlands from Tootchi et al. (2019) enables to approximate the spatial
924 distribution of anoxic soil. However, in our approach, seasonality is only represented through soil temperature
925 seasonality. Anoxic soil temporal dynamic was initially included in the model described by Ogée et al. (2016) with
926 the soil redox potential but is not implemented in land surface models such as ORCHIDEE yet. We could also
927 refine our approach by distinguishing between the different types of wetlands and define a P_{ref} value for each
928 wetland type instead of a global value of $10 \text{ pmol COS m}^{-2} \text{ s}^{-1}$. Then, a distinction could also be made for anoxic
929 soil COS fluxes from boreal peatlands, as Meredith et al. (2019) give a value of f_{CA} specific to this biome.
930 Moreover, indirect COS emissions from DMS oxidation in anoxic soils have been reported (Kettle et al., 2002;
931 Watts, 2000) but are not represented in this study. Finally, the anoxic map used here represents 9.7% of the global
932 land area, but the distribution of anoxic soils can greatly vary depending on the study (between 3% and 21%,
933 Tootchi et al., 2019). Therefore, it would also be interesting to investigate the impact of anoxic soil coverage on
934 soil COS flux uncertainty.

935 **5 Conclusions and Outlooks**

936 We have implemented in the ORCHIDEE LSM a mechanistic and an empirical model for simulating soil COS
937 fluxes. The mechanistic model, that performs a spatialization of the Ogee et al. (2016) model, enables us to
938 consider that oxic soils can be net COS producers, as illustrated at some of the observation sites. The inter-
939 hemispheric gradient of COS surface atmospheric mixing ratio is marginally improved when all known COS
940 sources and sinks are transported with the LMDZ model. This study also highlights the sensitivity of simulated
941 atmospheric COS concentrations to soil COS flux representation in the northern latitudes. Thus, the uncertainty in
942 soil COS fluxes could complicate GPP estimation using COS in the northern hemisphere.

943 The soil COS budget at global scale over the 2009-2016 period is -30 GgS yr^{-1} , resulting from the contribution of
944 oxic soils that represent a net sink of -126 GgS yr^{-1} , and of anoxic soils that represent a source of $+96 \text{ GgS yr}^{-1}$. It
945 is to be noted that the contribution from anoxic soils, while leading to a similar global budget to Launois et al.
946 (2015), has a different spatial distribution based on the repartition of regularly flooded wetlands from Tootchi et
947 al. (2019). This repartition seems more accurate as it also includes anoxic soil COS flux in the tropical region and
948 considers a larger variety of anoxic soils, such as salt marshes and rice paddies.

949 During this work, we have also shown the importance of considering spatially and temporally variable atmospheric
950 COS concentrations on soil COS fluxes, with an especially large impact at global scale. This result evidences the
951 impact of the recently decreasing atmospheric COS concentrations on the estimated soil COS fluxes.

952 Regarding the ORCHIDEE model, we performed a sensitivity study highlighting the key parameters to optimize
953 for the soil models. The impact of soil model parameter optimization was studied at two sites. This study exhibited
954 strong arguments in favour of the mechanistic model as performing an optimization of the empirical model
955 parameters can lead to aliasing errors and a degradation of the simulated soil water content. A larger database of
956 COS flux measurements at the site scale and especially full year time series would greatly help for the next step,
957 which would be to optimize the parameters of ecosystem COS fluxes.

958 **Appendix A: Parameters, variables, and constants for soil COS models**

959

960

Table A1: Carbonic anhydrase enhancement factor adapted to ORCHIDEE biomes.

ORCHIDEE biomes	Biomes from Meredith et al. (2019)	f_{CA} value from Meredith et al. (2019) (unitless)
1 - Bare soil	Desert	13000 ± 5400
2 - Tropical broad-leaved evergreen	Temperate broadleaf forest	32000 ± 1800
3 - Tropical broad-leaved raingreen	Temperate broadleaf forest	32000 ± 1800
4 - Temperate needleleaf evergreen	Temperate coniferous forest	32000 ± 3100
5 - Temperate broad-leaved evergreen	Temperate broadleaf forest	32000 ± 1800
6 - Temperate broad-leaved summergreen	Temperate broadleaf forest	32000 ± 1800
7 - Boreal needleleaf evergreen	Temperate coniferous forest	32000 ± 3100
8 - Boreal broad-leaved summergreen	Temperate broadleaf forest	32000 ± 1800
9 - Boreal needleleaf summergreen	Temperate coniferous forest	32000 ± 3100
10 - C ₃ grass	Mediterranean grassland	17000 ± 9000
11 - C ₄ grass	Mediterranean grassland	17000 ± 9000
12 - C ₃ agriculture	Agricultural	6500 ± 6900
13 - C ₄ agriculture	Agricultural	6500 ± 6900
14 - Tropical C ₃ grass	Tropical grassland	45000
15 - Boreal C ₃ grass	Mediterranean grassland	17000 ± 9000

961

962

a mis en forme : Justifié

963 **Table A2: α and β parameters for COS production term adapted to ORCHIDEE biomes.**

ORCHIDEE biomes	Biomes from Whelan et al. (2016)	α parameter from Whelan et al. (2016) (unitless)	β parameter from Whelan et al. (2016) ($^{\circ}\text{C}^{-1}$)
1 - Bare soil	Desert	N/A	N/A
2 - Tropical broad-leaved evergreen	Rainforest	-8.2	0.101
3 - Tropical broad-leaved raingreen	Rainforest	-8.2	0.101
4 - Temperate needleleaf evergreen	Temperate forest	-7.77	0.119
5 - Temperate broad-leaved evergreen	Temperate forest	-7.77	0.119
6 - Temperate broad-leaved summergreen	Temperate forest	-7.77	0.119
7 - Boreal needleleaf evergreen	Temperate forest	-7.77	0.119
8 - Boreal broad-leaved summergreen	Temperate forest	-7.77	0.119
9 - Boreal needleleaf summergreen	Temperate forest	-7.77	0.119
10 - C ₃ grass	Savannah	-9.54	0.108
11 - C ₄ grass	Savannah	-9.54	0.108
12 - C ₃ agriculture	Soy field	-6.12	0.096
13 - C ₄ agriculture	Soy field	-6.12	0.096
14 - Tropical C ₃ grass	Savannah	-9.54	0.108
15 - Boreal C ₃ grass	Savannah	-9.54	0.108

964
965
966
967

968 **Table A3: Variables for the empirical and mechanistic COS soil models.**

Variable name	Description	Unit	Reference
Empirical COS soil model			
$F_{soil,empirical}$	Empirical model soil COS flux	pmol COS m ⁻² s ⁻¹	(Berry et al., 2013) (Yi et al., 2007b)
$Resp_{tot}$	Total (heterotrophic and autotrophic) soil respiration	μmol CO ₂ m ⁻² s ⁻¹	(Yi et al., 2007b)
Mechanistic COS soil model			
ϵ_{tot}	Total soil COS porosity	m ³ air m ⁻³ soil	(Ogée et al., 2016)
C	Soil COS concentration	mol m ⁻³	(Ogée et al., 2016)
F_{diff}	Soil COS diffusional flux	mol m ⁻² s ⁻¹	(Ogée et al., 2016)
S	Soil COS consumption rate	mol m ⁻³ s ⁻¹	(Ogée et al., 2016)
P	Soil COS production rate	mol m ⁻³ s ⁻¹	(Whelan et al., 2016)
$F_{soil,mechanistic}$	Mechanistic model soil COS flux	mol m ⁻² s ⁻¹	(Ogée et al., 2016)
k	Total COS consumption rate by soil	s ⁻¹	(Ogée et al., 2016)
B	Solubility of COS in soil water	m ³ water m ⁻³ air	(Ogée et al., 2016)
θ	Soil volumetric water content	m ³ water m ⁻³ soil	(Ogée et al., 2016)
D	Total effective COS diffusivity in soil	m ² s ⁻¹	(Ogée et al., 2016)
z_1	Characteristic deep for soil COS flux	m	(Ogée et al., 2016)
k_{uncat}	Uncatalysed rate of COS hydrolysis in the soil water	s ⁻¹	(Elliott et al., 1989)
k_{cat}	Turnover rate of COS enzymatic reaction catalyzed by CA	s ⁻¹	(Ogée et al., 2016)
K_m	Michaelis-Menten constant of CA catalysis	mol m ⁻³	(Ogée et al., 2016)

x_{CA}	Temperature dependence of the ratio k_{cat}/K_m	1	(Ogée et al., 2016)
k	Soil total COS consumption rate	s^{-1}	(Ogée et al., 2016)
f_{CA}	CA enhancement factor	1	(Meredith et al., 2019)
$D_{eff,a}$	Effective diffusivity of gaseous COS in soil	$m^3 \text{ air } m^{-1} \text{ soil } s^{-1}$	(Ogée et al., 2016)
$D_{eff,l}$	Effective diffusivity of dissolved COS in soil	$m^3 \text{ water } m^{-1} \text{ soil } s^{-1}$	(Ogée et al., 2016)
K_H	Henry's law constant	$mol \text{ m}^{-3} \text{ Pa}^{-1}$	(Bird et al., 2002)
$D_{0,a}$	Binary diffusivity of COS in the free air	$m^2 \text{ air } s^{-1}$	(Bird et al., 2002)
τ_a	Tortuosity factor for gaseous diffusion	1	(Ogée et al., 2016)
$\tau_{a,r}$	Tortuosity factor for gaseous diffusion in repacked soils	1	(Moldrup et al., 2003)
$\tau_{a,u}$	Tortuosity factor for gaseous diffusion in undisturbed soils	1	(Deepagoda et al., 2011)
$D_{0,l}$	Binary diffusivity of COS in the free water	$m^2 \text{ water } s^{-1}$	(Zeebe, 2011)
τ_l	Tortuosity factor for solute diffusion	1	(Millington and Quirk, 1961)
α	COS production parameter	1	(Whelan et al., 2016)
β	COS production parameter	1	(Whelan et al., 2016)
ORCHIDEE LSM			
p	Pressure		ORCHIDEE LSM
ε_a	Air-filled porosity	$m^3 \text{ air } m^{-3} \text{ soil}$	ORCHIDEE LSM

φ	Total soil porosity (air-filled and water-filled pores)	$\text{m}^3 \text{m}^{-3}$	ORCHIDEE LSM
T	Mean soil temperature	K	ORCHIDEE LSM
t	time	s	ORCHIDEE LSM
z	depth	m	ORCHIDEE LSM

969
970

971 **Table A4: Constants for the empirical and mechanistic COS soil models.**

Constant name	Description	Value	Unit	Reference
Empirical COS soil model				
k_{soil}	Constant to converts CO ₂ production from respiration to a COS uptake	1.2	pmol COS/μmol CO ₂	(Yi et al., 2007)
Mechanistic COS soil model				
C_a	Ambient air COS concentration when chosen constant (500 ppt)	2.0437×10^{-8}	mol m ⁻³	
z_{max}	Maximum soil depth	0.09	m	ORCHIDEE LSM
pK _w	Dissociation constant of water	14	1	
ΔH_a	Thermodynamic parameter	40	kJ mol ⁻¹	(Ogée et al., 2016)
ΔH_d	Thermodynamic parameter	200	kJ mol ⁻¹	(Ogée et al., 2016)
ΔS_d	Thermodynamic parameter	660	J mol ⁻¹ K ⁻¹	(Ogée et al., 2016)
R	Ideal gas constant	8.314	J mol ⁻¹ K ⁻¹	
$D_{0,a}(25^\circ C, 1 atm)$	Binary diffusivity of COS in the free air at 25°C and 1 atm	1.27×10^{-5}	m ² s ⁻¹	(Massman, 1998)
$D_{0,l}(25^\circ C)$	Binary diffusivity of COS in the free water at 25°C	1.94×10^{-9}	m ² s ⁻¹	(Ulshöfer et al., 1996)
Q_{10}	Multiplicative factor of the production rate for a 10 °C temperature rise	2.7	1	(Meredith et al., 2018)

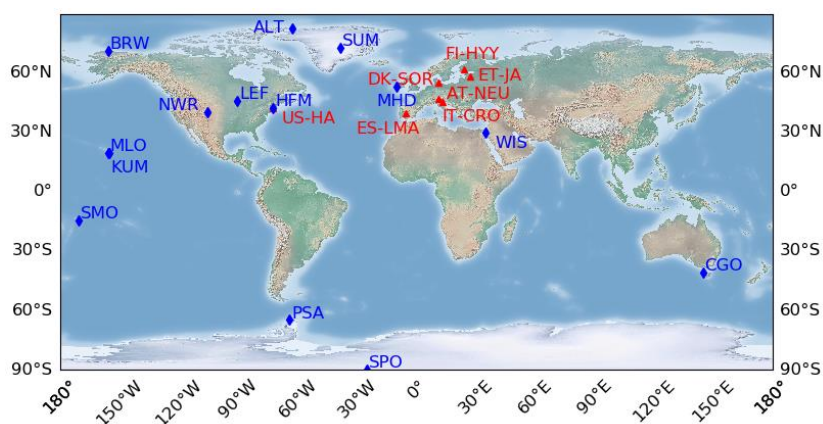
972

P_{ref}	Reference production term	10	$\text{pmol m}^2 \text{s}^{-1}$
-----------	---------------------------	----	---------------------------------

a mis en forme : Justifié

973 **Appendix B: Locations and descriptions of the observation sites**

974



975

976 **Figure B1: Locations of the observation sites for soil COS flux measurements (red) and atmospheric concentration**
 977 **measurements (blue).**

978

979 **Table B1: List of air sampling sites selected for evaluation of COS concentrations.**

Site	Short name	Coordinates	Elevation (m above sea level)	Comments
South Pole, Antarctica, United States	SPO	90.0°S, 24.8°E	2810	
Palmer Station, Antarctica, United States	PSA	64.77°S, 64.05°W	10.0	
Cape Grim, Australia	CGO	40.68°S, 144.69°E	164	inlet is 70 m aboveground
Tutuila, American Samoa	SMO	14.25°S, 170.56°W	77	
Mauna Loa, United States	MLO	19.54°N, 155.58°W	3397	
Cape Kumukahi, United States	KUM	19.74°N, 155.01°W	3	
Weizmann Institute of Science at the Arava Institute, Ketura, Israel	WIS	29.96°N, 35.06°E	151	
Niwot Ridge, United States	NWR	40.04°N, 105.54°W	3475	
Harvard Forest, United States	HFM	42.54°N, 72.17°W	340	inlet is 29 m aboveground

Wisconsin, United States	LEF	45.95°N, 90.28°W	868	inlet is 396 m aboveground on a tall tower
Mace Head, Ireland	MHD	53.33°N, 9.9°W	18	
Barrow, United States	BRW	71.32°N, 155.61°W	8	
Summit, Greenland	SUM	72.6°N, 38.42°W	3200	
Alert, Canada	ALT	82.45°N, 62.51°W	195	

980

981

982 **Table B2: Normalized standard deviations (NSDs) of the simulated concentrations by the observed concentrations.**

983 **Within brackets are the Pearson correlation coefficients (r) between simulated and observed COS concentrations for**

984 **the mechanistic and empirical approaches, calculated between 2011 and 2015 at selected NOAA stations. For each**

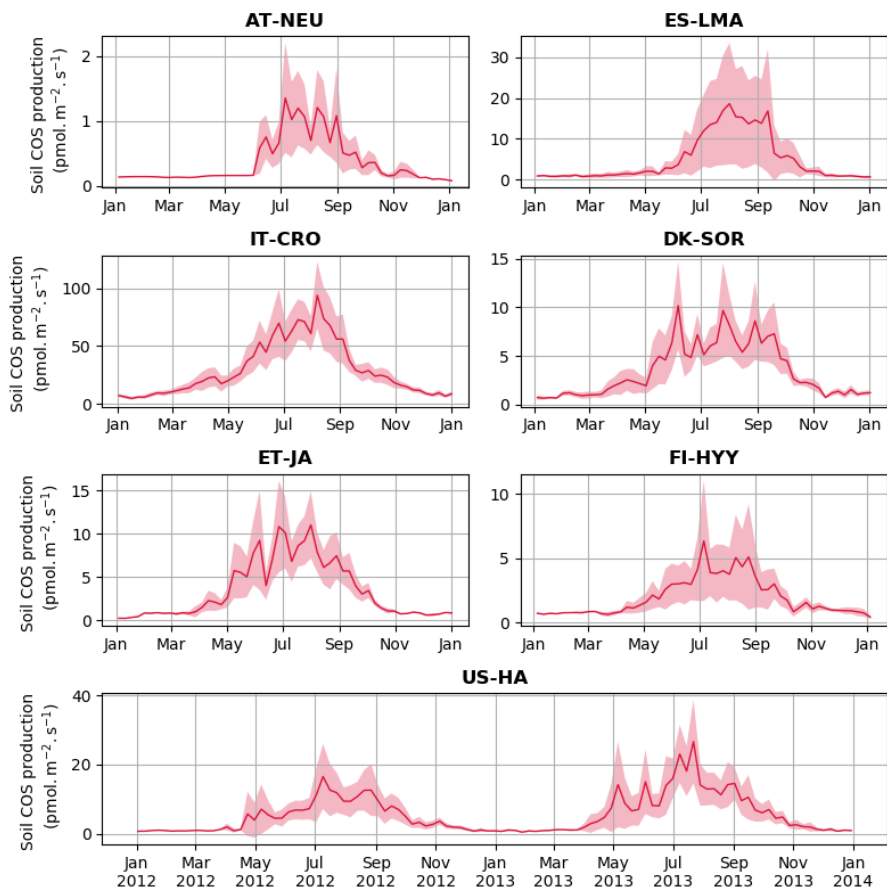
985 **station, NSD and r closest to one are in bold and farthest ones are in italic. The time-series have been detrended**

986 **beforehand and filtered to remove the synoptic variability (see Sect. 2.3.3).**

	SMO	KUM	MLO	NWR	LEF	HFM	MHD	SUM	BRW	ALT
Mechanistic	1.1	0.7	0.9	0.4	0.2	0.3	1.5	0.4	1.1	0.8
(Oxic)	(0.8)	(0.7)	(0.8)	(0.4)	(0.7)	(0.8)	(0.2)	(0.2)	(0.1)	(0.1)
Empirical	1.0	0.8	1.2	0.8	0.5	0.6	1.5	0.5	1.3	0.9
(Oxic)	(0.7)	(0.9)	(0.9)	(0.4)	(0.9)	(0.9)	(0.4)	(0.6)	(0.3)	(0.4)
Mechanistic	1.2	0.6	0.9	0.5	0.2	0.3	1.0	0.4	1.3	0.8
(Oxic+Anoxic)	(0.7)	(0.6)	(0.7)	(0.1)	(0.2)	(0.5)	(0.1)	(0.0)	(0.1)	(0.1)
Launois	1.1	1.0	1.4	1.4	0.9	0.8	1.6	0.6	1.2	0.9
(Oxic+Anoxic)	(0.6)	(0.9)	(0.9)	(0.7)	(0.9)	(0.9)	(0.4)	(0.7)	(0.4)	(0.4)

987

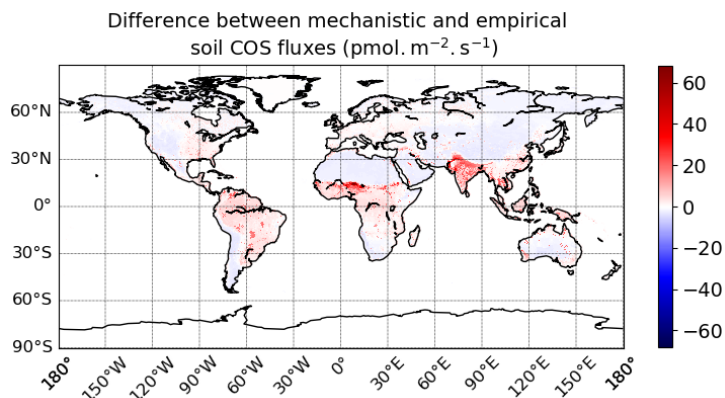
988



992 **Figure C1:** Seasonal cycles of soil COS production with weekly average production at AT-NEU, ES-LMA, IT-CRO,
993 **DK-SOR, ET-JA, FI-HYY, US-HA.** The shaded areas above and below the modelled curve represent the standard-
994 deviation over a week. Soil COS production was computed with a variable atmospheric COS concentration.

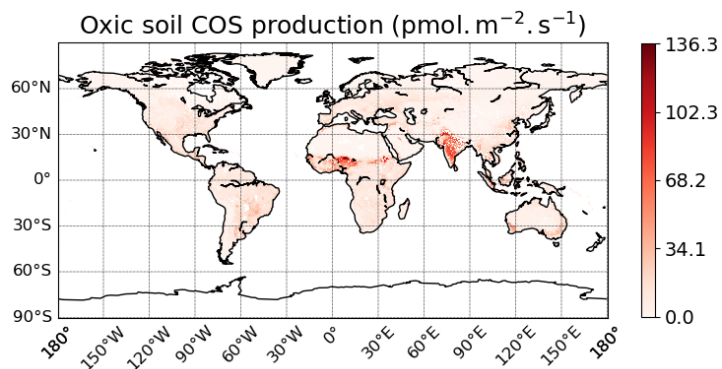
997 **Appendix D: Global scale soil COS fluxes**

998



999
1000 **Figure D1: Mean difference between soil COS fluxes computed with the mechanistic and the empirical model over 2010-**
1001 **2019. The map resolution is 0.5°x0.5°.**

1002



1003
1004 **Figure D2: Mean spatial distribution of oxic soil COS production term over 2010-2019. The map resolution is 0.5°x0.5°.**

1005

1006

1007

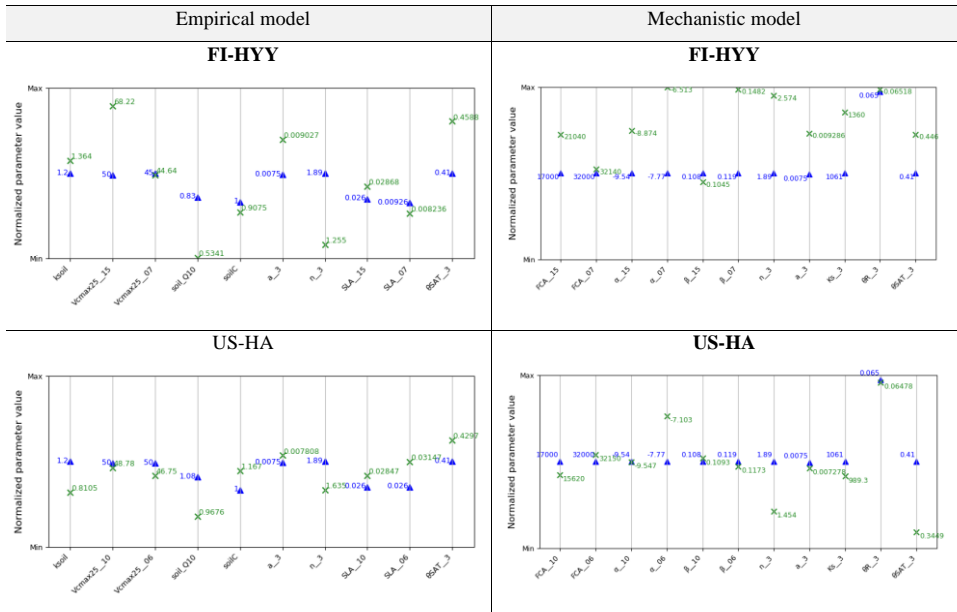
1008

1009

1010

1011

1012 Appendix E: Prior versus post optimization parameter values
 1013



1014 Figure E1: Comparison between prior and posterior optimization parameter values at FI-HYY and US-HA. The y-axis
 1015 represents the normalization between the edges of the range of variation for each parameter. Prior values of the
 1016 parameters are represented in blue and post optimization values are in green.

a mis en forme : Justifié

1017 *Code availability.* The CMIP6 version of the ORCHIDEE model including the soil COS sub-models is available
1018 on request to the authors. The LMDZ model is available from <http://web.lmd.jussieu.fr/LMDZ/LMDZ6/> (last
1019 access: 21 October 2021) under the CeCILL v2 Free Software License.

1020

1021 *Data availability.* For FI-HYY, we used the 2015 soil chamber COS measurements published in Sun et al. (2018).
1022 For US-HA, we used the soil COS flux data derived from eddy covariance COS and CO₂ measurements and soil
1023 chamber CO₂ measurements conducted in 2012 and 2013, published in Wehr et al. (2017). We used the COS flux
1024 data published in Kitz et al. (2020) and Spielmann et al. (2019) for AT-NEU in 2015, DK-SOR and ES-LMA in
1025 2016 and IT-CRO in 2017.

1026

1027 *Author contributions.* CA, FM, MR, and PP conceived the research. JO advised regarding the spatialization of his
1028 mechanistic model. CA and FM coded the ORCHIDEE developments and made the simulations. MR transported
1029 all COS sinks and sources with the LMDZ model. FK, FMS, and GW provided the data for AT-NEU, ES-LMA,
1030 DK-SOR, IT-CRO and ET-JA. WS provided the data for FI-HYY site and RW for the US-HA site. NR provided
1031 code and guidance for the sensitivity analysis and data assimilation experiments. SB, JEC, MEW, DH, STL, US
1032 and DM were consulted on their respective expertise.

1033

1034 *Competing interests.* The authors declare that they have no conflict of interest.

1035

1036 *Acknowledgments.*

1037 [The authors thank the reviewers for their insightful and useful comments which helped to improve this study.](#) The
1038 authors are very grateful to everyone who participated in field data collection used in this study. We thank
1039 Vladislav Bastrikov for providing the ORCHIDAS code. We also acknowledge Nicolas Vuichard for providing
1040 the soil bulk density map used in ORCHIDEE simulations. Operation of the US-HA site is supported by the
1041 AmeriFlux Management Project with funding by the U.S. Department of Energy's Office of Science under
1042 Contract No. DE-AC02-05CH11231 and additionally is a part of the Harvard Forest LTER site supported by the
1043 National Science Foundation (DEB-1832210). The field campaign at DK-SOR was supported by the Danish ICOS
1044 contribution (ICOS/DK) and by the Danish Council for Independent Research grant DFF-1323-00182.

1045

1046 *Financial support.*

1047 This research has been mainly supported by the European Commission, Horizon 2020 Framework Programme,
1048 4C (grant no. 821003) and to a small extend VERIFY (grant no. 776810)

1049 FK, FMS and GW acknowledge funding by the Austrian National Science Fund (FWF) through contracts P26931,
1050 P27176, P31669 and I03859 and the University of Innsbruck.

1051

1052 References

- 1053
- 1054 Aneja, V. P., Overton, J. H., and Aneja, A. P.: Emission survey of biogenic sulfur flux from terrestrial surfaces,
1055 31, 256–258, <https://doi.org/10.1080/00022470.1981.10465218>, 1981.
- 1056 Barba, J., Cueva, A., Bahn, M., Barron-Gafford, G. A., Bond-Lamberty, B., Hanson, P. J., Jaimes, A., Kulmala,
1057 L., Pumpanen, J., Scott, R. L., Wohlfahrt, G., and Vargas, R.: Comparing ecosystem and soil respiration: review
1058 and key challenges of tower-based and soil measurements, 2018.
- 1059 Bastrikov, V., Macbean, N., Bacour, C., Santaren, D., Kuppel, S., and Peylin, P.: Land surface model parameter
1060 optimisation using in situ flux data: Comparison of gradient-based versus random search algorithms (a case study
1061 using ORCHIDEE v1.9.5.2), 11, 4739–4754, <https://doi.org/10.5194/gmd-11-4739-2018>, 2018.
- 1062 Belviso, S., Schmidt, M., Yver, C., Ramonet, M., Gros, V., and Launois, T.: Strong similarities between night-
1063 time deposition velocities of carbonyl sulphide and molecular hydrogen inferred from semi-continuous
1064 atmospheric observations in Gif-sur-Yvette, Paris region, 65, 20719, <https://doi.org/10.3402/tellusb.v65i0.20719>,
1065 2013.
- 1066 Belviso, S., Lebegue, B., Ramonet, M., Kazan, V., Pison, I., Berchet, A., Delmotte, M., Yver-Kwok, C., Montagne,
1067 D., and Ciaï, P.: A top-down approach of sources and non-photosynthetic sinks of carbonyl sulfide from
1068 atmospheric measurements over multiple years in the Paris region (France),
1069 <https://doi.org/10.1371/journal.pone.0228419i>, 2020.
- 1070 Berkelhammer, M., Asaf, D., Still, C., Montzka, S., Noone, D., Gupta, M., Provencal, R., Chen, H., and Yakir, D.:
1071 Constraining surface carbon fluxes using in situ measurements of carbonyl sulfide and carbon dioxide, 28, 161–
1072 179, <https://doi.org/10.1002/2013GB004644>, 2014.
- 1073 Berry, J., Wolf, A., Campbell, J. E., Baker, I., Blake, N., Blake, D., Denning, A. S., Kawa, S. R., Montzka, S. A.,
1074 Seibt, U., Stimler, K., Yakir, D., and Zhu, Z.: A coupled model of the global cycles of carbonyl sulfide and CO₂:
1075 A possible new window on the carbon cycle, 118, 842–852, <https://doi.org/10.1002/jgrg.20068>, 2013.
- 1076 Bird, B., Stewart, W., and Lightfoot, E.: *Transport Phenomena*, 2002.
- 1077 Boucher, O., Servonnat, J., Albright, A. L., Aumont, O., Balkanski, Y., Bastrikov, V., Bekki, S., Bonnet, R., Bony,
1078 S., Bopp, L., Braconnot, P., Brockmann, P., Cadule, P., Caubel, A., Cheruy, F., Codron, F., Cozic, A., Cugnet, D.,
1079 D’Andrea, F., Davini, P., de Lavergne, C., Denvil, S., Deshayes, J., Devilliers, M., Ducharne, A., Dufresne, J. L.,
1080 Dupont, E., Éthé, C., Fairhead, L., Falletti, L., Flavoni, S., Foujols, M. A., Gardoll, S., Gastineau, G., Ghattas, J.,
1081 Grandpeix, J. Y., Guenet, B., Guez, L. E., Guilyardi, E., Guimberteau, M., Hauglustaine, D., Hourdin, F., Idelkadi,
1082 A., Joussaume, S., Kageyama, M., Khodri, M., Krinner, G., Lebas, N., Levvasseur, G., Lévy, C., Li, L., Lott, F.,
1083 Lurton, T., Luyssaert, S., Madec, G., Madeleine, J. B., Maignan, F., Marchand, M., Marti, O., Mellul, L.,
1084 Meurdesoif, Y., Mignot, J., Musat, I., Ottlé, C., Peylin, P., Planton, Y., Polcher, J., Rio, C., Rochetin, N., Rousset,
1085 C., Sepulchre, P., Sima, A., Swingedouw, D., Thiéblemont, R., Traore, A. K., Vancoppenolle, M., Vial, J., Vialard,
1086 J., Viovy, N., and Vuichard, N.: Presentation and Evaluation of the IPSL-CM6A-LR Climate Model, 12,
1087 <https://doi.org/10.1029/2019MS002010>, 2020.
- 1088 Brændholt, A., Ibrom, A., Larsen, K. S., and Pilegaard, K.: Partitioning of ecosystem respiration in a beech forest,
1089 252, 88–98, <https://doi.org/10.1016/j.agrformet.2018.01.012>, 2018.
- 1090 Burkholder, J. B., Sander, S. P., Abbatt, J. P. D., Barker, J. R., Cappa, C., Crouse, J. D., Dibble, T. S., Huie, R.
1091 E., Kolb, C. E., Kurylo, M. J., Orkin, V. L., Percival, C. J., Wilmouth, D. M., and Wine, P. H.: Chemical Kinetics

1092 and Photochemical Data for Use in Atmospheric Studies Evaluation Number 19 NASA Panel for Data Evaluation,
1093 2019.

1094 Campbell, J. E., Carmichael, G. R., Chai, T., Mena-Carrasco, M., Tang, Y., Blake, D. R., Blake, N. J., Vay, S. A.,
1095 Collatz, G. J., Baker, I., Berry, J. A., Montzka, S. A., Sweeney, C., Schnoor, J. L., and Stanier, C. O.:
1096 Photosynthetic control of atmospheric carbonyl sulfide during the growing season, 322, 1085–1088,
1097 <https://doi.org/10.1126/science.1164015>, 2008.

1098 Campolongo, F., Cariboni, J., and Saltelli, A.: An effective screening design for sensitivity analysis of large
1099 models, 22, 1509–1518, <https://doi.org/10.1016/j.envsoft.2006.10.004>, 2007.

1100 Cheruy, F., Ducharne, A., Hourdin, F., Musat, I., Vignon, É., Gastineau, G., Bastrikov, V., Vuichard, N., Diallo,
1101 B., Dufresne, J. L., Ghattas, J., Grandpeix, J. Y., Idelkadi, A., Mellul, L., Maignan, F., Ménégoz, M., Ottlé, C.,
1102 Peylin, P., Servonnat, J., Wang, F., and Zhao, Y.: Improved Near-Surface Continental Climate in IPSL-CM6A-
1103 LR by Combined Evolutions of Atmospheric and Land Surface Physics, 12,
1104 <https://doi.org/10.1029/2019MS002005>, 2020.

1105 Chin, M. and Davis, D. D.: A reanalysis of carbonyl sulfide as a source of stratospheric background sulfur aerosol,
1106 100, 8993–9005, <https://doi.org/10.1029/95JD00275>, 1995.

1107 Dantec-Nédélec, S., Ottlé, C., Wang, T., Guglielmo, F., Maignan, F., Delbart, N., Valdayskikh, V., Radchenko,
1108 T., Nekrasova, O., Zakharov, V., and Jouzel, J.: Testing the capability of ORCHIDEE land surface model to
1109 simulate Arctic ecosystems: Sensitivity analysis and site-level model calibration, 9, 1212–1230,
1110 <https://doi.org/10.1002/2016MS000860>, 2017.

1111 Davidson, C., Amrani, A., and Angert, A.: Tropospheric carbonyl sulfide mass balance based on direct
1112 measurements of sulfur isotopes, <https://doi.org/10.1073/pnas.2020060118/-/DCSupplemental>, 2021.

1113 Deepagoda, T. K. K. C., Moldrup, P., Schjønning, P., de Jonge, L. W., Kawamoto, K., and Komatsu, T.: Density-
1114 Corrected Models for Gas Diffusivity and Air Permeability in Unsaturated Soil, 10, 226–238, <https://doi.org/10.2136/vzj2009.0137>, 2011.

1116 Devai, I. and DeLaune, R. D.: Trapping Efficiency of Various Solid Adsorbents for Sampling and Quantitative
1117 Gas Chromatographic Analysis of Carbonyl Sulfide, 30, 187–198, <https://doi.org/10.1080/00032719708002300>,
1118 1997.

1119 van Diest, H. and Kesselmeier, J.: Soil atmosphere exchange of carbonyl sulfide (COS) regulated by diffusivity
1120 depending on water-filled pore space, *Biogeosciences*, 475–483 pp., 2008.

1121 Elliott, S., Lu, E., and Rowland, F. S.: Rates and mechanisms for the hydrolysis of carbonyl sulfide in natural
1122 waters, 23, 458–461, <https://doi.org/10.1021/es00181a011>, 1989.

1123 El-Madany, T. S., Reichstein, M., Perez-Priego, O., Carrara, A., Moreno, G., Pilar Martín, M., Pacheco-Labrador,
1124 J., Wohlfahrt, G., Nieto, H., Weber, U., Kolle, O., Luo, Y. P., Carvalhais, N., and Migliavacca, M.: Drivers of
1125 spatio-temporal variability of carbon dioxide and energy fluxes in a Mediterranean savanna ecosystem, 262, 258–
1126 278, <https://doi.org/10.1016/j.agrformet.2018.07.010>, 2018.

1127 Folberth, G. A., Hauglustaine, D. A., Lathi Ere, J., and Brocheton, F.: Interactive chemistry in the Laboratoire de
1128 Météorologie Dynamique general circulation model: model description and impact analysis of biogenic
1129 hydrocarbons on tropospheric chemistry, *Atmos. Chem. Phys.*, 2273–2319 pp., 2006.

1130 Friedlingstein, P., O’Sullivan, M., Jones, M. W., Andrew, R. M., Hauck, J., Olsen, A., Peters, G. P., Peters, W.,
1131 Pongratz, J., Sitch, S., le Quééré, C., Canadell, J. G., Ciais, P., Jackson, R. B., Alin, S., Aragão, L. E. O. C., Arneth,

1132 A., Arora, V., Bates, N. R., Becker, M., Benoit-Cattin, A., Bittig, H. C., Bopp, L., Bultan, S., Chandra, N.,
1133 Chevallier, F., Chini, L. P., Evans, W., Florentie, L., Forster, P. M., Gasser, T., Gehlen, M., Gilfillan, D., Gkritzalis,
1134 T., Gregor, L., Gruber, N., Harris, I., Hartung, K., Haverd, V., Houghton, R. A., Ilyina, T., Jain, A. K., Joetzjer,
1135 E., Kadono, K., Kato, E., Kitidis, V., Korsbakken, J. I., Landschützer, P., Lefèvre, N., Lenton, A., Lienert, S., Liu,
1136 Z., Lombardozi, D., Marland, G., Metzl, N., Munro, D. R., Nabel, J. E. M. S., Nakaoka, S. I., Niwa, Y., O'Brien,
1137 K., Ono, T., Palmer, P. I., Pierrot, D., Poulter, B., Resplandy, L., Robertson, E., Rödenbeck, C., Schwinger, J.,
1138 Séférian, R., Skjelvan, I., Smith, A. J. P., Sutton, A. J., Tanhua, T., Tans, P. P., Tian, H., Tilbrook, B., van der
1139 Werf, G., Vuichard, N., Walker, A. P., Wanninkhof, R., Watson, A. J., Willis, D., Wiltshire, A. J., Yuan, W., Yue,
1140 X., and Zaehle, S.: Global Carbon Budget 2020, 12, 3269–3340, <https://doi.org/10.5194/essd-12-3269-2020>, 2020.
1141 van Genuchten, M. Th.: A closed-form equation for predicting the hydraulic conductivity of unsaturated soils,
1142 44(5), 892–898, 1980.
1143 Giasson, M. A., Ellison, A. M., Bowden, R. D., Crill, P. M., Davidson, E. A., Drake, J. E., Frey, S. D., Hadley, J.
1144 L., Lavine, M., Melillo, J. M., Munger, J. W., Nadelhoffer, K. J., Nicoll, L., Ollinger, S. v., Savage, K. E., Stuedler,
1145 P. A., Tang, J., Varner, R. K., Wofsy, S. C., Foster, D. R., and Finzi, A. C.: Soil respiration in a northeastern US
1146 temperate forest: A 22-year synthesis, 4, <https://doi.org/10.1890/ES13.00183.1>, 2013.
1147 Glatthor, N., Höpfner, M., Baker, I. T., Berry, J., Campbell, J. E., Kawa, S. R., Krysztofiak, G., Leysner, A.,
1148 Sinnhuber, B. M., Stiller, G. P., Stinecipher, J., and von Clarmann, T.: Tropical sources and sinks of carbonyl
1149 sulfide observed from space, 42, 10082–10090, <https://doi.org/10.1002/2015GL066293>, 2015.
1150 Goldberg, D. E.: Genetic Algorithms in Search, Optimization, and Machine Learning., 1989.
1151 Hauglustaine, D. A., Hourdin, F., Jourdain, L., Filiberti, M. A., Walters, S., Lamarque, J. F., and Holland, E. A.:
1152 Interactive chemistry in the Laboratoire de Météorologie Dynamique general circulation model: Description and
1153 background tropospheric chemistry evaluation, 109, <https://doi.org/10.1029/2003jd003957>, 2004.
1154 Hauglustaine, D. A., Balkanski, Y., and Schulz, M.: A global model simulation of present and future nitrate
1155 aerosols and their direct radiative forcing of climate, 14, 11031–11063, [https://doi.org/10.5194/acp-14-11031-](https://doi.org/10.5194/acp-14-11031-2014)
1156 2014, 2014.
1157 Haupt, R. L. and Haupt, S. E.: Practical Genetic Algorithms., Wiley., 2004.
1158 [Helmig, D., Apel, E., Blake, D. et al. Release and uptake of volatile inorganic and organic gases through the](#)
1159 [snowpack at Niwot Ridge, Colorado. Biogeochemistry 95, 167–183 \(2009\). \[https://doi.org/10.1007/s10533-009-\]\(https://doi.org/10.1007/s10533-009-9326-8\)](#)
1160 [9326-8](#)
1161 Hersbach, H., Bell, B., Berrisford, P., Hirahara, S., Horányi, A., Muñoz-Sabater, J., Nicolas, J., Peubey, C., Radu,
1162 R., Schepers, D., Simmons, A., Soci, C., Abdalla, S., Abellan, X., Balsamo, G., Bechtold, P., Biavati, G., Bidlot,
1163 J., Bonavita, M., de Chiara, G., Dahlgren, P., Dee, D., Diamantakis, M., Dragani, R., Flemming, J., Forbes, R.,
1164 Fuentes, M., Geer, A., Haimberger, L., Healy, S., Hogan, R. J., Hólm, E., Janisková, M., Keeley, S., Laloyaux, P.,
1165 Lopez, P., Lupu, C., Radnoti, G., de Rosnay, P., Rozum, I., Vamborg, F., Villaume, S., and Thépaut, J. N.: The
1166 ERA5 global reanalysis, 146, 1999–2049, <https://doi.org/10.1002/qj.3803>, 2020.
1167 Hörtnagl, L., Bamberger, I., Graus, M., Ruuskanen, T. M., Schnitzhofer, R., Müller, M., Hansel, A., and
1168 Wohlfahrt, G.: Biotic, abiotic, and management controls on methanol exchange above a temperate mountain
1169 grassland, 116, <https://doi.org/10.1029/2011JG001641>, 2011.
1170 Hörtnagl, L. and Wohlfahrt, G.: Methane and nitrous oxide exchange over a managed hay meadow, 11, 7219–
1171 7236, <https://doi.org/10.5194/bg-11-7219-2014>, 2014.

1172 Hourdin, F. and Issartel, J. P.: Sub-surface nuclear tests monitoring through the CTBT xenon network, 27, 2245–
1173 2248, <https://doi.org/10.1029/1999GL010909>, 2000.

1174 Hourdin, F., Rio, C., Grandpeix, J. Y., Madeleine, J. B., Cheruy, F., Rochetin, N., Jam, A., Musat, I., Idelkadi, A.,
1175 Fairhead, L., Foujols, M. A., Mellul, L., Traore, A. K., Dufresne, J. L., Boucher, O., Lefebvre, M. P., Millour, E.,
1176 Vignon, E., Jouhaud, J., Diallo, F. B., Lott, F., Gastineau, G., Caubel, A., Meurdesoif, Y., and Ghattas, J.:
1177 LMDZ6A: The Atmospheric Component of the IPSL Climate Model With Improved and Better Tuned Physics,
1178 12, <https://doi.org/10.1029/2019MS001892>, 2020.

1179 [Kaisermann, A., Jones, S. P., Wohl, S., Ogée, J. and Wingate, L.: Nitrogen Fertilization Reduces the Capacity of](#)
1180 [Soils to Take up Atmospheric Carbonyl Sulphide, *Soil Syst.*, 2\(4\),doi:10.3390/soilsystems2040062, 2018.](#)

1181 Kanda, K. I., Tsuruta, H., and Minami, K.: Emission of dimethyl sulfide, carbonyl sulfide, and carbon disulfide
1182 from paddy fields, 38, 709–716, <https://doi.org/10.1080/00380768.1992.10416701>, 1992.

1183 Kesselmeier, J., Teusch, N., and Kuhn, U.: Controlling variables for the uptake of atmospheric carbonyl sulfide
1184 by soil, 104, 11577–11584, <https://doi.org/10.1029/1999JD900090>, 1999.

1185 Kettle, A. J., Kuhn, U., von Hobe, M., Kesselmeier, J., and Andreae, M. O.: Global budget of atmospheric carbonyl
1186 sulfide: Temporal and spatial variations of the dominant sources and sinks, 107,
1187 <https://doi.org/10.1029/2002JD002187>, 2002.

1188 Kitz, F., Gerdel, K., Hammerle, A., Laterza, T., Spielmann, F. M., and Wohlfahrt, G.: In situ soil COS exchange
1189 of a temperate mountain grassland under simulated drought, 183, 851–860, [https://doi.org/10.1007/s00442-016-](https://doi.org/10.1007/s00442-016-3805-0)
1190 [3805-0](https://doi.org/10.1007/s00442-016-3805-0), 2017.

1191 Kitz, F., Spielmann, F. M., Hammerle, A., Kolle, O., Migliavacca, M., Moreno, G., Ibrom, A., Krasnov, D., Noe,
1192 S. M., and Wohlfahrt, G.: Soil COS Exchange: A Comparison of Three European Ecosystems, 34,
1193 <https://doi.org/10.1029/2019GB006202> (last access: 21 Octobre 2021), 2020.

1194 Kolari, P., Kulmala, L., Pumpanen, J., Launiainen, S., Ilvesniemi, H., Hari, P., and Nikinmaa, E.: CO₂ exchange
1195 and component CO₂ fluxes of a boreal Scots pine forest, 2009.

1196 Kooijmans, L. M. J., Cho, A., Ma, J., Kaushik, A., Haynes, K. D., Baker, I., Luijckx, I. T., Groenink, M., Peters,
1197 W., Miller, J., Berry, J. A., Ogée, J., Meredith, L. K., Sun, W., -Maaria, K., Krol, M., and Kooijmans, L.:
1198 Evaluation of carbonyl sulfide biosphere exchange in the Simple Biosphere Model (SiB4), 10, 20,
1199 <https://doi.org/10.5194/bg-2021-192>, 2021.

1200 Kuai, L., Worden, J. R., Campbell, J. E., Kulawik, S. S., Li, K. F., Lee, M., Weidner, R. J., Montzka, S. A., Moore,
1201 F. L., Berry, J. A., Baker, I., Denning, A. S., Bian, H., Bowman, K. W., Liu, J., and Yung, Y. L.: Estimate of
1202 carbonyl sulfide tropical oceanic surface fluxes using aura tropospheric emission spectrometer observations, 120,
1203 11,012-11,023, <https://doi.org/10.1002/2015JD023493>, 2015.

1204 Kuppel, S., Peylin, P., Maignan, F., Chevallier, F., Kiely, G., Montagnani, L., and Cescatti, A.: Model-data fusion
1205 across ecosystems: From multisite optimizations to global simulations, 7, 2581–2597,
1206 <https://doi.org/10.5194/gmd-7-2581-2014>, 2014.

1207 Lardy, R., Bellocchi, G., and Soussana, J. F.: A new method to determine soil organic carbon equilibrium, 26,
1208 1759–1763, <https://doi.org/10.1016/j.envsoft.2011.05.016>, 2011.

1209 Launois, T., Peylin, P., Belviso, S., and Poulter, B.: A new model of the global biogeochemical cycle of carbonyl
1210 sulfide - Part 2: Use of carbonyl sulfide to constrain gross primary productivity in current vegetation models, 15,
1211 9285–9312, <https://doi.org/10.5194/acp-15-9285-2015>, 2015.

1212 Lennartz, S. T., Marandino, C. A., von Hobe, M., Cortes, P., Quack, B., Simo, R., Booge, D., Pozzer, A., Steinhoff,
1213 T., Arevalo-Martinez, D. L., Kloss, C., Bracher, A., Atlas, E., and Krüger, K.: Direct oceanic emissions unlikely
1214 to account for the missing source of atmospheric carbonyl sulfide, 17, 385–402, [https://doi.org/10.5194/acp-17-](https://doi.org/10.5194/acp-17-385-2017)
1215 385-2017, 2017.

1216 Lennartz, S., A Marandino, C., von Hobe, M., O Andreae, M., Aranami, K., Atlas, E., Berkelhammer, M.,
1217 Bingemer, H., Booge, D., Cutter, G., Cortes, P., Kremser, S., S Law, C., Marriner, A., Simó, R., Quack, B., Xie,
1218 H., and Xu, X.: Marine carbonyl sulfide (OCS) and carbon disulfide (CS₂): A compilation of measurements in
1219 seawater and the marine boundary layer, 12, 591–609, <https://doi.org/10.5194/essd-12-591-2020>, 2020.

1220 Lennartz, S. T., Gauss, M., von Hobe, M., and Marandino, C. A.: Monthly resolved modelled oceanic emissions
1221 of carbonyl sulphide and carbon disulphide for the period 2000–2019, 13, 2095–2110,
1222 <https://doi.org/10.5194/essd-13-2095-2021>, 2021.

1223 Liu, J., Geng, C., Mu, Y., Zhang, Y., Xu, Z., and Wu, H.: Exchange of carbonyl sulfide (COS) between the
1224 atmosphere and various soils in China, *Biogeosciences*, 753–762 pp., 2010.

1225 Lopez-Sangil, L., Rousk, J., Wallander, H., and Casals, P.: Microbial growth rate measurements reveal that land-
1226 use abandonment promotes a fungal dominance of SOM decomposition in grazed Mediterranean ecosystems, 47,
1227 129–138, <https://doi.org/10.1007/s00374-010-0510-8>, 2011.

1228 Ma, X., Huang, J., Zhao, T., Liu, C., Zhao, K., Xing, J., and Xiao, W.: Rapid increase in summer surface ozone
1229 over the North China Plain during 2013-2019: A side effect of particulate matter reduction control?, 21, 1–16,
1230 <https://doi.org/10.5194/acp-21-1-2021>, 2021.

1231 MacBean, N., Maignan, F., Bacour, C., Lewis, P., Peylin, P., Guanter, L., Köhler, P., Gómez-Dans, J., and Disney,
1232 M.: Strong constraint on modelled global carbon uptake using solar-induced chlorophyll fluorescence data, 8,
1233 <https://doi.org/10.1038/s41598-018-20024-w>, 2018.

1234 Mahmud, K., Scott, R. L., Biederman, J. A., Litvak, M. E., Kolb, T., Meyers, T. P., Bastrikov, V., and MacBean,
1235 N.: Optimizing Carbon Cycle Parameters Drastically Improves Terrestrial Biosphere Model Underestimates of
1236 Dryland Mean Net CO₂ Flux and its Inter-Annual Variability, 2021.

1237 Maignan, F., Abadie, C., Remaud, M., Kooijmans, L. M. J., Kohonen, K.-M., Commane, R., Wehr, R., Campbell,
1238 J. E., Belviso, S., Montzka, S. A., Raoult, N., Seibt, U., Shiga, Y. P., Vuichard, N., Whelan, M. E., and Peylin, P.:
1239 Carbonyl sulfide: comparing a mechanistic representation of the vegetation uptake in a land surface model and the
1240 leaf relative uptake approach, 18, 2917–2955, <https://doi.org/10.5194/bg-18-2917-2021>, 2021.

1241 Masaki, Y., Iizuka, R., Kato, H., Kojima, Y., Ogawa, T., Yoshida, M., Matsushita, Y., and Katayama, Y.: Fungal
1242 carbonyl sulfide hydrolase of trichoderma harzianum strain thif8 and its relationship with clade D β-carbonic
1243 anhydrases, 36, <https://doi.org/10.1264/jsme2.ME20058>, 2021.

1244 Maseyk, K., Berry, J. A., Billesbach, D., Campbell, J. E., Torn, M. S., Zahniser, M., and Seibt, U.: Sources and
1245 sinks of carbonyl sulfide in an agricultural field in the Southern Great Plains, 111, 9064–9069,
1246 <https://doi.org/10.1073/pnas.1319132111>, 2014.

1247 Masotti, I., Belviso, S., Bopp, L., Tagliabue, A., and Bucciarelli, E.: Effects of light and phosphorus on summer
1248 DMS dynamics in subtropical waters using a global ocean biogeochemical model, in: *Environmental Chemistry*,
1249 379–389, <https://doi.org/10.1071/EN14265>, 2016.

1250 Massman, W. J.: A review of the molecular diffusivities of H and NO in air, O and N near STP, *Atmospheric*
1251 *Environment*, 1111–1127 pp., 1998.

1252 Mellillo, J. M. and Stuedler, P. A.: The effect of nitrogen fertilization on the COS and CS₂ emissions from
1253 temperature forest soils, 9, 411–417, <https://doi.org/10.1007/BF00114753>, 1989.

1254 de Mello, W. Z. and Hines, M. E.: Application of static and dynamic enclosures for determining dimethyl sulfide
1255 and carbonyl sulfide exchange in Sphagnum peatlands: Implications for the magnitude and direction of flux,
1256 JOURNAL OF GEOPHYSICAL RESEARCH, 601–615 pp., 1994.

1257 Meredith, L. K., Boye, K., Youngerman, C., Whelan, M., Ogée, J., Sauze, J., and Wingate, L.: Coupled biological
1258 and abiotic mechanisms driving carbonyl sulfide production in soils, 2, 1–27,
1259 <https://doi.org/10.3390/soilsystems2030037>, 2018.

1260 Meredith, L. K., Ogée, J., Boye, K., Singer, E., Wingate, L., von Sperber, C., Sengupta, A., Whelan, M., Pang, E.,
1261 Keiluweit, M., Brüggemann, N., Berry, J. A., and Welander, P. v.: Soil exchange rates of COS and CO¹⁸O differ
1262 with the diversity of microbial communities and their carbonic anhydrase enzymes, 13, 290–300,
1263 <https://doi.org/10.1038/s41396-018-0270-2>, 2019.

1264 Millington, R. J. and Quirk, J. P.: Permeability of porous solids, 57, 1200–1207,
1265 <https://doi.org/10.1039/TF9615701200>, 1961.

1266 Moldrup, P., Olesen, T., Komatsu, T., Yoshikawa, S., Schjønning, P., and Rolston, D. E.: Modeling diffusion and
1267 reaction in soils: x. a unifying model for solute and gas diffusivity in unsaturated soil, 168, 2003.

1268 Montzka, S. A., Calvert, P., Hall, B. D., Elkins, J. W., Conway, T. J., Tans, P. P., and Sweeney, C. S.: On the
1269 global distribution, seasonality, and budget of atmospheric carbonyl sulfide (COS) and some similarities to CO₂,
1270 112, <https://doi.org/10.1029/2006JD007665>, 2007.

1271 Morris, M. D.: Factorial Sampling Plans for Preliminary Computational Experiments, 33, 161–174,
1272 <https://doi.org/10.1080/00401706.1991.10484804>, 1991.

1273 Noe, S. M., Kimmel, V., Hüve, K., Copolovici, L., Portillo-Estrada, M., Püttsepp, Ü., Jögiste, K., Niinemets, Ü.,
1274 Hörtnagl, L., and Wohlfahrt, G.: Ecosystem-scale biosphere-atmosphere interactions of a hemiboreal mixed forest
1275 stand at Järvselja, Estonia, 262, 71–81, <https://doi.org/10.1016/j.foreco.2010.09.013>, 2011.

1276 Noe, S. M., Niinemets, Ü., Krasnova, A., Krasnov, D., Motallebi, A., Kängsepp, V., Jögiste, K., Hörrak, U.,
1277 Komsaare, K., Mirmo, S., Vana, M., Tammet, H., Bäck, J., Vesala, T., Kulmala, M., Petäjä, T., and Kangur, A.:
1278 SMEAR Estonia: Perspectives of a large-scale forest ecosystem– Atmosphere research infrastructure, 63, 56–84,
1279 <https://doi.org/10.1515/fsmu-2015-0009>, 2015.

1280 Ogée, J., Sauze, J., Kesselmeier, J., Genty, B., van Diest, H., Launois, T., and Wingate, L.: A new mechanistic
1281 framework to predict OCS fluxes from soils, 13, 2221–2240, <https://doi.org/10.5194/bg-13-2221-2016>, 2016.

1282 Parazoo, N. C., Denning, A. S., Berry, J. A., Wolf, A., Randall, D. A., Kawa, S. R., Pauluis, O., and Doney, S. C.:
1283 Moist synoptic transport of CO₂ along the mid-latitude storm track, 38, <https://doi.org/10.1029/2011GL047238>,
1284 2011.

1285 Pastorello, G., Trotta, C., Canfora, E., Chu, H., Christianson, D., Cheah, Y. W., Poindexter, C., Chen, J.,
1286 Elbashandy, A., Humphrey, M., Isaac, P., Polidori, D., Ribeca, A., van Ingen, C., Zhang, L., Amiro, B., Ammann,
1287 C., Arain, M. A., Ardö, J., Arkebauer, T., Arndt, S. K., Arriga, N., Aubinet, M., Aurela, M., Baldocchi, D., Barr,
1288 A., Beamesderfer, E., Marchesini, L. B., Bergeron, O., Beringer, J., Bernhofer, C., Berveiller, D., Billesbach, D.,
1289 Black, T. A., Blanken, P. D., Bohrer, G., Boike, J., Bolstad, P. v., Bonal, D., Bonnefond, J. M., Bowling, D. R.,
1290 Bracho, R., Brodeur, J., Brümmer, C., Buchmann, N., Burban, B., Burns, S. P., Buysse, P., Cale, P., Cavagna, M.,
1291 Cellier, P., Chen, S., Chini, I., Christensen, T. R., Cleverly, J., Collalti, A., Consalvo, C., Cook, B. D., Cook, D.,

1292 Coursolle, C., Cremonese, E., Curtis, P. S., D'Andrea, E., da Rocha, H., Dai, X., Davis, K. J., de Cinti, B., de
1293 Grandcourt, A., de Ligne, A., de Oliveira, R. C., Delpierre, N., Desai, A. R., di Bella, C. M., di Tommasi, P.,
1294 Dolman, H., Domingo, F., Dong, G., Dore, S., Duce, P., Dufrene, E., Dunn, A., Dušek, J., Eamus, D., Eichelmann,
1295 U., ElKhidir, H. A. M., Eugster, W., Ewenz, C. M., Ewers, B., Famulari, D., Fares, S., Feigenwinter, I., Feitz, A.,
1296 Fensholt, R., Filippa, G., Fischer, M., Frank, J., Galvagno, M., Gharun, M., Gianelle, D., et al.: The
1297 FLUXNET2015 dataset and the ONEFlux processing pipeline for eddy covariance data, 7, 225,
1298 <https://doi.org/10.1038/s41597-020-0534-3>, 2020.

1299 Peylin, P., Ciais, P., Denning, A. S., Tans, P. P., Berry, J. A., and White, J. W. C.: A 3-dimensional study of δ^{18}
1300 O in atmospheric CO₂: contribution of different land ecosystems, 51, 642–667,
1301 <https://doi.org/10.3402/tellusb.v51i3.16452>, 1999.

1302 Peylin, P., Bacour, C., MacBean, N., Leonard, S., Rayner, P., Kuppel, S., Koffi, E., Kane, A., Maignan, F.,
1303 Chevallier, F., Ciais, P., and Prunet, P.: A new stepwise carbon cycle data assimilation system using multiple data
1304 streams to constrain the simulated land surface carbon cycle, 9, 3321–3346, [https://doi.org/10.5194/gmd-9-3321-](https://doi.org/10.5194/gmd-9-3321-2016)
1305 2016, 2016.

1306 Pilegaard, K., Ibrom, A., Courtney, M. S., Hummelshøj, P., and Jensen, N. O.: Increasing net CO₂ uptake by a
1307 Danish beech forest during the period from 1996 to 2009, 151, 934–946,
1308 <https://doi.org/10.1016/j.agrformet.2011.02.013>, 2011.

1309 [Poulter, B., MacBean, N., Hartley, A., Khlystova, I., Arino, O., Betts, R., Bontemps, S., Boettcher, M.,](#)
1310 [Brockmann, C., Defourny, P., Hagemann, S., Herold, M., Kirches, G., Lamarche, C., Lederer, D., Ottlé, C., Peters,](#)
1311 [M., and Peylin, P.: Plant functional type classification for earth system models: results from the European Space](#)
1312 [Agency's Land Cover Climate Change Initiative, Geosci. Model Dev., 8, 2315–2328, https://doi.org/10.5194/gmd-](#)
1313 [8-2315-2015, 2015.](#)

1314 Protoschill-Krebs, G., Wilhelm, C., and Kesselmeier, J.: Consumption of carbonyl sulphide (COS) by higher plant
1315 carbonic anhydrase (CA), Atmospheric Environment, 996 pp., 1996.

1316 Raoult, N., Ottlé, C., Peylin, P., Bastrikov, V., and Maugis, P.: Evaluating and Optimizing Surface Soil Moisture
1317 Drydowns in the ORCHIDEE Land Surface Model at In Situ Locations, <https://doi.org/10.1175/JHM-D-20, 2021>.

1318 Remaud, M., Chevallier, F., Cozic, A., Lin, X., and Bousquet, P.: On the impact of recent developments of the
1319 LMDz atmospheric general circulation model on the simulation of CO₂ transport, 11, 4489–4513,
1320 <https://doi.org/10.5194/gmd-11-4489-2018>, 2018.

1321 [Remaud, M., Chevallier, F., Maignan, F., Belviso, S., Berchet, A., Parouffe, A., Abadie, C., Bacour, C., Lennartz,](#)
1322 [S., and Peylin, P.: Plant gross primary production, plant respiration and carbonyl sulfide emissions over the globe](#)
1323 [inferred by atmospheric inverse modelling, Atmos. Chem. Phys., 22, 2525–2552, https://doi.org/10.5194/acp-22-](#)
1324 [2525-2022, 2022.](#) [Remaud, M., Chevallier, F., Maignan, F., Belviso, S., Berchet, A., Parouffe, A., Abadie, C.,](#)
1325 [Bacour, C., Lennartz, S., and Peylin, P.: Plant gross primary production, plant respiration and carbonyl sulfide](#)
1326 [emissions over the globe inferred by atmospheric inverse modelling, https://doi.org/10.5194/acp-2021-326, 2021.](#)

1327

1328 Reynolds, C. A., Jackson, T. J., and Rawls, W. J.: Estimating soil water-holding capacities by linking the Food
1329 and Agriculture Organization soil map of the world with global pedon databases and continuous pedotransfer
1330 functions, 36, 3653–3662, <https://doi.org/10.1029/2000WR900130>, 2000.

1331 Sandoval-Soto, L., Stanimirov, M., von Hobe, M., Schmitt, V., Valdes, J., Wild, A., and Kesselmeier, J.: Global
1332 uptake of carbonyl sulfide (COS) by terrestrial vegetation: Estimates corrected by deposition velocities normalized
1333 to the uptake of carbon dioxide (CO₂), *Biogeosciences*, 125–132 pp., 2005.

1334 Sauze, J., Ogée, J., Maron, P.-A., Crouzet, O., Nowak, V., Wohl, S., Kaisermann, A., Jones, S., Wingate, L., Ee,
1335 O., and Jones, S. P.: The interaction of soil phototrophs and fungi with pH and their impact on soil CO₂, CO¹⁸ O
1336 and OCS exchange, <https://doi.org/10.1016/j.soilbio.2017.09.009>, 2017.

1337 Sitch, S., Friedlingstein, P., Gruber, N., Jones, S. D., Murray-Tortarolo, G., Ahlström, A., Doney, S. C., Graven,
1338 H., Heinze, C., Huntingford, C., Levis, S., Levy, P. E., Lomas, M., Poulter, B., Viovy, N., Zaehle, S., Zeng, N.,
1339 Arneth, A., Bonan, G., Bopp, L., Canadell, J. G., Chevallier, F., Ciais, P., Ellis, R., Gloor, M., Peylin, P., Piao, S.
1340 L., le Quééré, C., Smith, B., Zhu, Z., and Myneni, R.: Recent trends and drivers of regional sources and sinks of
1341 carbon dioxide, 12, 653–679, <https://doi.org/10.5194/bg-12-653-2015>, 2015.

1342 Smith, K., Jakubzick, C., Whittam, T., and Ferry, J.: Carbonic anhydrase is an ancient enzyme widespread in
1343 prokaryotes, *P. Natl. Acad. Sci. USA*, 96, 15184–15189, 1999.

1344 Smith, K. S. and Ferry, J. G.: Prokaryotic carbonic anhydrases, 24, 335–366, <https://doi.org/10.1111/j.1574-6976.2000.tb00546.x>, 2000.

1346 Spielmann, F. M., Wohlfahrt, G., Hammerle, A., Kitz, F., Migliavacca, M., Alberti, G., Ibrom, A., El-Madany, T.
1347 S., Gerdel, K., Moreno, G., Kolle, O., Karl, T., Peressotti, A., and Delle Vedove, G.: Gross Primary Productivity
1348 of Four European Ecosystems Constrained by Joint CO₂ and COS Flux Measurements, 46, 5284–5293,
1349 <https://doi.org/10.1029/2019GL082006> (last access: 21 Octobre 2021), 2019.

1350 Spielmann, F., Hammerle, A., Kitz, F., Gerdel, K., and Wohlfahrt, G.: Seasonal dynamics of the COS and CO₂
1351 exchange of a managed temperate grassland, 1–19, <https://doi.org/10.5194/bg-2020-27>, 2020.

1352 Stinecipher, J. R., Cameron-Smith, P. J., Blake, N. J., Kuai, L., Lejeune, B., Mahieu, E., Simpson, I. J., and
1353 Campbell, J. E.: Biomass Burning Unlikely to Account for Missing Source of Carbonyl Sulfide, 46, 14912–14920,
1354 <https://doi.org/10.1029/2019GL085567>, 2019.

1355 [Sun, W., Maseyk, K. S., Juarez, S., Lett, C., and Seibt, U. H.: Soil-atmosphere carbonyl sulfide \(COS\) exchange
1356 in a tropical rainforest at La Selva, Costa Rica. AGU Fall Meeting Abstracts, 2014, B41C-0075, 2014.](#)

1357 Sun, W., Maseyk, K., Lett, C., and Seibt, U.: A soil diffusion-reaction model for surface COS flux: COSSM v1,
1358 8, 3055–3070, <https://doi.org/10.5194/gmd-8-3055-2015>, 2015.

1359 Sun, W., Kooijmans, L. M. J., Maseyk, K., Chen, H., Mammarella, I., Vesala, T., Levula, J., Keskinen, H., and
1360 Seibt, U.: Soil fluxes of carbonyl sulfide (COS), carbon monoxide, and carbon dioxide in a boreal forest in southern
1361 Finland, 18, 1363–1378, <https://doi.org/10.5194/acp-18-1363-2018> (last access: 21 Octobre 2021), 2018.

1362 Sweeney, C., Karion, A., Wolter, S., Newberger, T., Guenther, D., Higgs, J. A., Andrews, A. E., Lang, P. M., Neff,
1363 D., Dlugokencky, E., Miller, J. B., Montzka, S. A., Miller, B. R., Masarie, K. A., Biraud, S. C., Novelli, P. C.,
1364 Crotwell, M., Crotwell, A. M., Thoning, K., and Tans, P. P.: Seasonal climatology of CO₂ across north america
1365 from aircraft measurements in the NOAA/ESRL global greenhouse gas reference network, 120, 5155–5190,
1366 <https://doi.org/10.1002/2014JD022591>, 2015.

1367 Tarantola, A.: Inverse Problem Theory and Methods for Model Parameter Estimation, Society for Industrial and
1368 Applied Mathematics, <https://doi.org/10.1137/1.9780898717921>, 2005.

1369 Terrenoire, E., Hauglustaine, D., Cohen, Y., Cozic, A., Valorso, R., Lefevre, F., Jegou, F., and Matthes, S.: Impact
1370 of present-day and future aircraft NO_x and aerosol emissions on atmospheric composition and associated radiative
1371 forcings of climate, in prep.

1372 Thoning, K. W., Tans, P. P., and Komhyr, W. D.: Atmospheric Carbon Dioxide at Mauna Loa Observatory 2.
1373 Analysis of the NOAA GMCC Data, 1974-1985, *JOURNAL OF GEOPHYSICAL RESEARCH*, 8549–8565 pp.,
1374 1989.

1375 Tootchi, A., Jost, A., and Ducharme, A.: Multi-source global wetland maps combining surface water imagery and
1376 groundwater constraints, 11, 189–220, <https://doi.org/10.5194/essd-11-189-2019>, 2019.

1377 Ulshijfer, V. S., Flijk, O. R., Uher, G., and Andreae, M. O.: Photochemical production and air-sea exchange of
1378 sulfide in the eastern Mediterranean Sea, *Marine Chemistry*, 25–39 pp., 1996.

1379 Urbanski, S., Barford, C., Wofsy, S., Kucharik, C., Pyle, E., Budney, J., McKain, K., Fitzjarrald, D., Czikowsky,
1380 M., and Munger, J. W.: Factors controlling CO₂ exchange on timescales from hourly to decadal at Harvard Forest,
1381 112, <https://doi.org/10.1029/2006JG000293>, 2007.

1382 Wania, R., Ross, I., and Prentice, I. C.: Implementation and evaluation of a new methane model within a dynamic
1383 global vegetation model: LPJ-WHyMe v1.3.1, 3, 565–584, <https://doi.org/10.5194/gmd-3-565-2010>, 2010.

1384 Watts, S. F.: The mass budgets of carbonyl sulfide, dimethyl sulfide, carbon disulfide and hydrogen sulfide,
1385 *Atmospheric Environment*, Volume 34, Issue 5, p. 761-779, 2000.

1386 Wehr, R., Commane, R., Munger, J. W., Barry Mcmanus, J., Nelson, D. D., Zahniser, M. S., Saleska, S. R., and
1387 Wofsy, S. C.: Dynamics of canopy stomatal conductance, transpiration, and evaporation in a temperate deciduous
1388 forest, validated by carbonyl sulfide uptake, 14, 389–401, <https://doi.org/10.5194/bg-14-389-2017> (last access: 21
1389 Octobre 2021), 2017.

1390 Weiner, T., Gross, A., Moreno, G., Migliavacca, M., Schrupf, M., Reichstein, M., Hilman, B., Carrara, A., and
1391 Angert, A.: Following the Turnover of Soil Bioavailable Phosphate in Mediterranean Savanna by Oxygen Stable
1392 Isotopes, 123, 1850–1862, <https://doi.org/10.1029/2017JG004086>, 2018.

1393 Whelan, M. E., Min, D. H., and Rhew, R. C.: Salt marsh vegetation as a carbonyl sulfide (COS) source to the
1394 atmosphere, 73, 131–137, <https://doi.org/10.1016/j.atmosenv.2013.02.048>, 2013.

1395 Whelan, M. E. and Rhew, R. C.: Carbonyl sulfide produced by abiotic thermal and photodegradation of soil organic
1396 matter from wheat field substrate, 120, 54–62, <https://doi.org/10.1002/2014JG002661>, 2015.

1397 Whelan, M. E., Hilton, T. W., Berry, J. A., Berkelhammer, M., Desai, A. R., and Elliott Campbell, J.: Carbonyl
1398 sulfide exchange in soils for better estimates of ecosystem carbon uptake, 16, 3711–3726,
1399 <https://doi.org/10.5194/acp-16-3711-2016>, 2016.

1400 Whelan, M., Lennartz, S., Gimeno, T., Wehr, R., Wohlfahrt, G., Wang, Y., Kooijmans, L., Hilton, T., Belviso, S.,
1401 Peylin, P., Whelan, M. E., Lennartz, S. T., Gimeno, T. E., Kooijmans, L. M. J., Hilton, T. W., Commane, R., Sun,
1402 W., Chen, H., Kuai, L., Mammarella, I., Maseyk, K., Berkelhammer, M., Li, K.-F., Yakir, D., Zumkehr, A.,
1403 Katayama, Y., Ogée, J., Spielmann, F. M., Kitz, F., Rastogi, B., Kesselmeier, J., Marshall, J., Erkkilä, K.-M.,
1404 Wingate, L., Meredith, L. K., He, W., Bunk, R., Launois, T., Vesala, T., Schmidt, J. A., Fichot, C. G., Seibt, U.,
1405 Saleska, S., Saltzman, E. S., Montzka, S. A., Berry, J. A., and Campbell, J. E.: Reviews and syntheses: Carbonyl
1406 sulfide as a multi-scale tracer for carbon and water cycles, 15, 3625–3657, [https://doi.org/10.5194/bg-15-3625-
1407 2018i](https://doi.org/10.5194/bg-15-3625-2018i), 2018.

1408 Wilhelm, Emmerich., Battino, Rubin., and Wilcock, R. J.: Low-pressure solubility of gases in liquid water, 77,
1409 219–262, <https://doi.org/10.1021/cr60306a003>, 1977.

1410 Wohlfahrt, G., Brilli, F., Hörtnagl, L., Xu, X., Bingemer, H., Hansel, A., and Loreto, F.: Carbonyl sulfide (COS)
1411 as a tracer for canopy photosynthesis, transpiration and stomatal conductance: Potential and limitations, 35, 657–
1412 667, <https://doi.org/10.1111/j.1365-3040.2011.02451.x>, 2012.

1413 Wu, J., Larsen, K. S., van der Linden, L., Beier, C., Pilegaard, K., and Ibrom, A.: Synthesis on the carbon budget
1414 and cycling in a Danish, temperate deciduous forest, 181, 94–107,
1415 <https://doi.org/10.1016/j.agrformet.2013.07.012>, 2013.

1416 Yan, Y., Li, R., Peng, L., Yang, C., Liu, C., Cao, J., Yang, F., Li, Y., and Wu, J.: Emission inventory of carbonyl
1417 sulfide (COS) from primary anthropogenic sources in China, 247, 745–751,
1418 <https://doi.org/10.1016/j.envpol.2019.01.096>, 2019.

1419 Yang, F., Qubaja, R., Tatarinov, F., Stern, R., and Yakir, D.: Soil-atmosphere exchange of carbonyl sulfide in a
1420 Mediterranean citrus orchard, 19, 3873–3883, <https://doi.org/10.5194/acp-19-3873-2019>, 2019.

1421 Yi, Z., Wang, X., Sheng, G., Zhang, D., Zhou, G., and Fu, J.: Soil uptake of carbonyl sulfide in subtropical forests
1422 with different successional stages in south China, 112, <https://doi.org/10.1029/2006JD008048>, 2007.

1423 Zeebe, R. E.: On the molecular diffusion coefficients of dissolved CO₂, HCO₃⁻, and CO₃²⁻ and their dependence
1424 on isotopic mass, 75, 2483–2498, <https://doi.org/10.1016/j.gca.2011.02.010>, 2011.

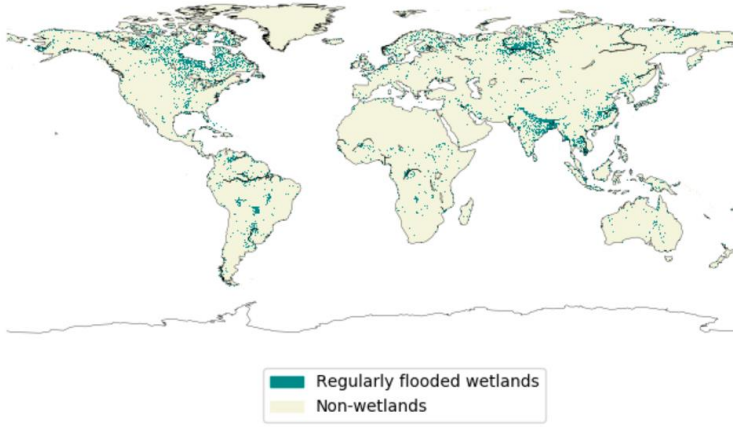
1425 Zhang, J., Wang, L., and Yang, Z.: Emission of Biogenic Sulfur Gases from the Microbial Decomposition of
1426 Cystine in Chinese Rice Paddy Soils Environmental Contamination and Toxicology 850, Bull. Environ. Contam.
1427 Toxicol, 850–857 pp., 2004.

1428 Zobler, L.: A World Soil File for Global Climate Modelling, 87802, 1986.

1429 Zumkehr, A., Hilton, T. W., Whelan, M., Smith, S., Kuai, L., Worden, J., and Campbell, J. E.: Global gridded
1430 anthropogenic emissions inventory of carbonyl sulfide, 183, 11–19,
1431 <https://doi.org/10.1016/j.atmosenv.2018.03.063>, 2018.

1432

1433



1434

1435 **Figure 1: Map of wetlands distribution used to represent anoxic soils in ORCHIDEE. The map resolution is 0.5°x0.5°**
1436 **(adapted from Tootchi et al., 2019).**

1437

1438

1439 **Table 1:** lists the sites' characteristics including their identification name, location, climate, soil type, dominant
1440 **vegetation and species, corresponding PFT fractions we used for the ORCHIDEE simulations, and reference studies for**
1441 **more details. The spatial distribution of the sites is represented in Appendix B, Figure B1.**

	Grassland	Savannah-like grassland	Deciduous broadleaf forest	Agricultural soybean field	Evergreen needleleaf forest	Boreal evergreen needleleaf forest	Temperate deciduous broadleaf forest
Country	Austria	Spain	Denmark	Italy	Estonia	Finland	United-States
Sampling site	Neustift	Las Majadas del Tietar	Sorø	Rivignano	Järvelja	Hyytiälä	Harvard
ID	AT-NEU	ES-LMA	DK-SOR	IT-CRO	ET-JA	FI-HYY	US-HA
Coordinates	47°07'N, 11°19'E	39°56'N, 5°46'W	55°29'N, 11°38'E	45°52'N, 13°05'E	58°16'N, 27°18'E	61.85°N, 24.29°E	42.54°N, 72.17°W
Climate	Humid continental	Mediterranean	Temperate maritime	Humid subtropical	Temperate	Boreal	Cool, moist temperate
Soil type	Fluvisol	Abruptic Luvisol	Luvisols or Chernozems-Alfisols or-Mollisols	Silt loam	Haplic Gleysol	Haplic Podzol	Podzol and Regosol/Sandy loam-glacial-till
Dominant vegetation	Graminoids: <i>Dactylis glomerata</i> , <i>Festuca pratensis</i> Forbs: <i>Ranunculus acris</i> , <i>Taraxacum officinale</i>	Tree: <i>Quercus ilex</i> Grass: <i>Vulpia bromoides</i>	European beech (<i>Fagus sylvatica</i>)	Soybean	Norway spruce (<i>Picea abies</i>)	Scots pine (<i>Pinus sylvestris</i>)	Red oak (<i>Quercus rubra</i>), Red maple (<i>Acer rubrum</i>), Hemlock (<i>Tsuga canadensis</i>).
ORCHIDEE PFT representation	100% temperate natural grassland (C ₃) (PFT 10)	20% temperate broadleaf evergreen (PFT 5) 80% temperate natural grassland (C ₃) (PFT 10)	80% boreal broadleaf summergreen (PFT 8) 20% boreal natural grassland (C ₃) (PFT 15)	100% C ₃ crops (PFT 12)	50% boreal needleleaf evergreen (PFT 7) 40% boreal broadleaf summergreen (PFT 8) 10% boreal natural grassland (C ₃) (PFT 15)	80% boreal needleleaf evergreen (PFT 7) 20% boreal natural grassland (C ₃) (PFT 15)	80% temperate broadleaf summergreen (PFT 6) 20% of temperate natural grassland (C ₃) (PFT 10)
References	Hörtnagl et al. (2011) Hörtnagl and Wohlfahrt (2014) Spielmann et al. (2019) Kitz et al. (2020)	Lopez-Sangil et al. (2011) El-Madany et al. (2018) Weiner et al. (2018) Spielmann et al. (2019) Spielmann et al. (2019)	Pilegaard et al. (2011) Wu et al. (2013) Brændholt et al. (2018) Spielmann et al. (2019) Kitz et al. (2020)	Spielmann et al. (2019)	Noe et al. (2011, 2015) Kitz et al. (2020)	Kolari et al. (2009) Sun et al. (2018)	Urbanski et al. (2007) Wehr et al. (2017)

mis en forme : Justifié

		Kitz et al. (2020)						
--	--	-----------------------	--	--	--	--	--	--

1442

a mis en forme : Justifié

Table 2: Prescribed COS surface fluxes used as model input. Mean magnitudes and standard deviations of different types of fluxes are given for the period 2009-2016.

Type of COS flux	Temporal resolution	Total (Gg S yr ⁻¹)	Standard deviation (Gg S yr ⁻¹)	Data Source
Anthropogenic	Monthly, interannual	394	21	Zumkehr et al. (2018). The fluxes for the year 2012 were repeated after 2012.
Biomass burning	Monthly, interannual	48	9	Stinecipher et al. (2019)
Soil	Monthly, interannual	See Table 5.	5 (oxic) 2 (anoxic)	This work, including mechanistic and empirical approaches (Berry et al., 2013; Launois et al., 2015)
Ocean	Monthly, interannual	313	14	Lennartz et al. (2021) and Masotti et al. (2015) for indirect oceanic emissions (via CS ₂ and DMS respectively), and Lennartz et al. (2017) for direct oceanic emissions
Vegetation uptake	Monthly, interannual	-576	7	Maignan et al. (2021)

Table 2: Sink and source components of COS budget used in this study. Mean magnitudes and standard deviations of different types of fluxes are given for the period 2009-2016.

Type of COS flux	Temporal resolution	Total (Gg S yr ⁻¹)	Standard deviation (Gg S yr ⁻¹)	Data Source
Anthropogenic	Monthly, interannual	+394	21	Zumkehr et al. (2018). The fluxes for the year 2012 were repeated after 2012.
Ocean	Monthly, interannual	+313	14	Lennartz et al. (2021) and Masotti et al. (2015) for indirect oceanic emissions (via CS ₂ and DMS respectively), and Lennartz et al. (2017) for direct oceanic emissions
Biomass burning	Monthly, interannual	+48	9	Stinecipher et al. (2019)
Soil	Monthly, interannual	See Table 3.	5 (oxic) 2 (anoxic)	This work, including mechanistic and empirical approaches (Berry et al., 2013; Launois et al., 2015)
Vegetation uptake	Monthly, interannual	-576	7	Maignan et al. (2021)

à mis en forme : Justifié

<u>Atmospheric OH oxidation</u>	<u>Monthly, interannual</u>	<u>-100</u>	<u>(-)</u>	<u>Hauglustaine et al. (2004)</u>
<u>Photolysis in the stratosphere</u>	<u>Monthly, interannual</u>	<u>-30</u>	<u>(-)</u>	<u>Remaud et al. (2022)</u>

a mis en forme le tableau

1448

1449

1450

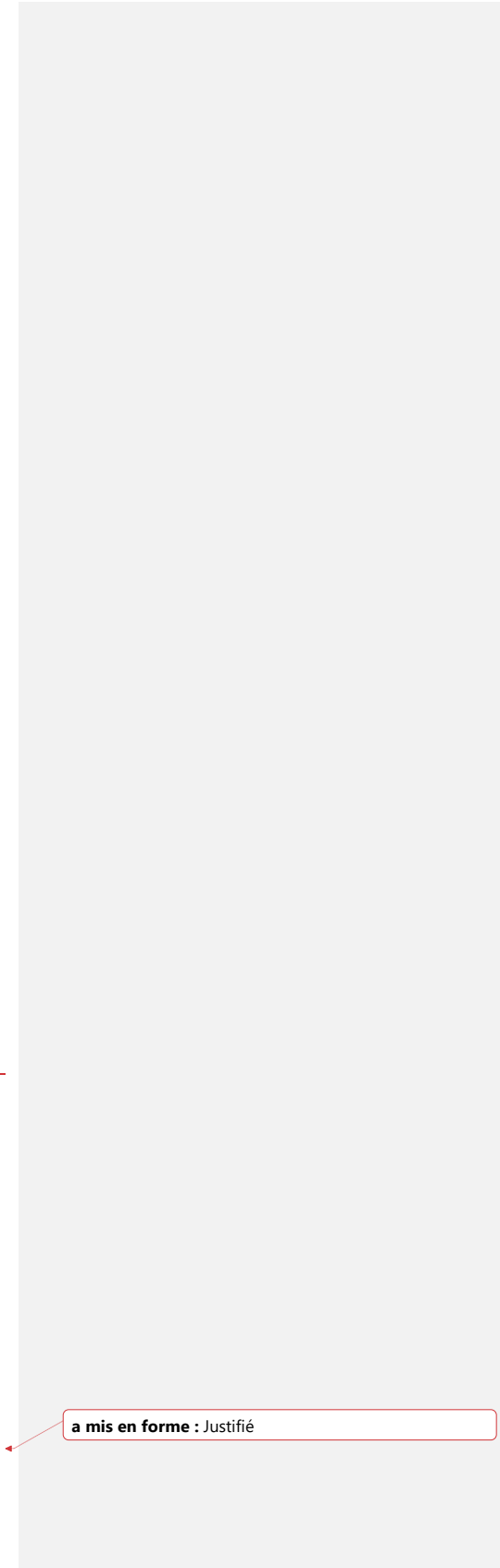
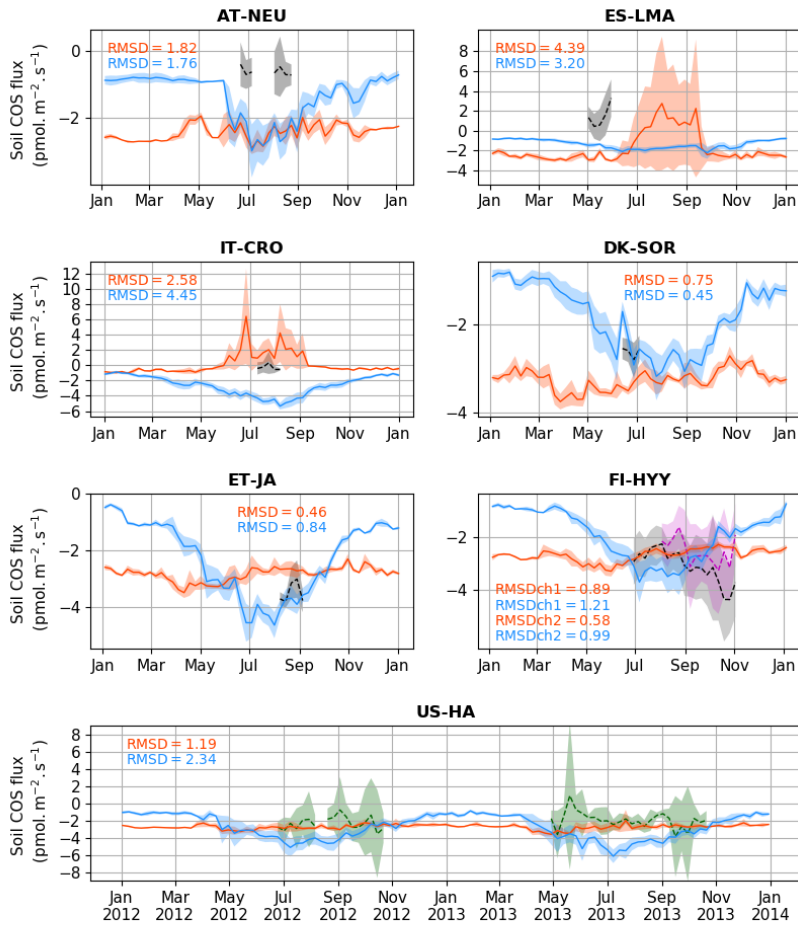
1451

1452

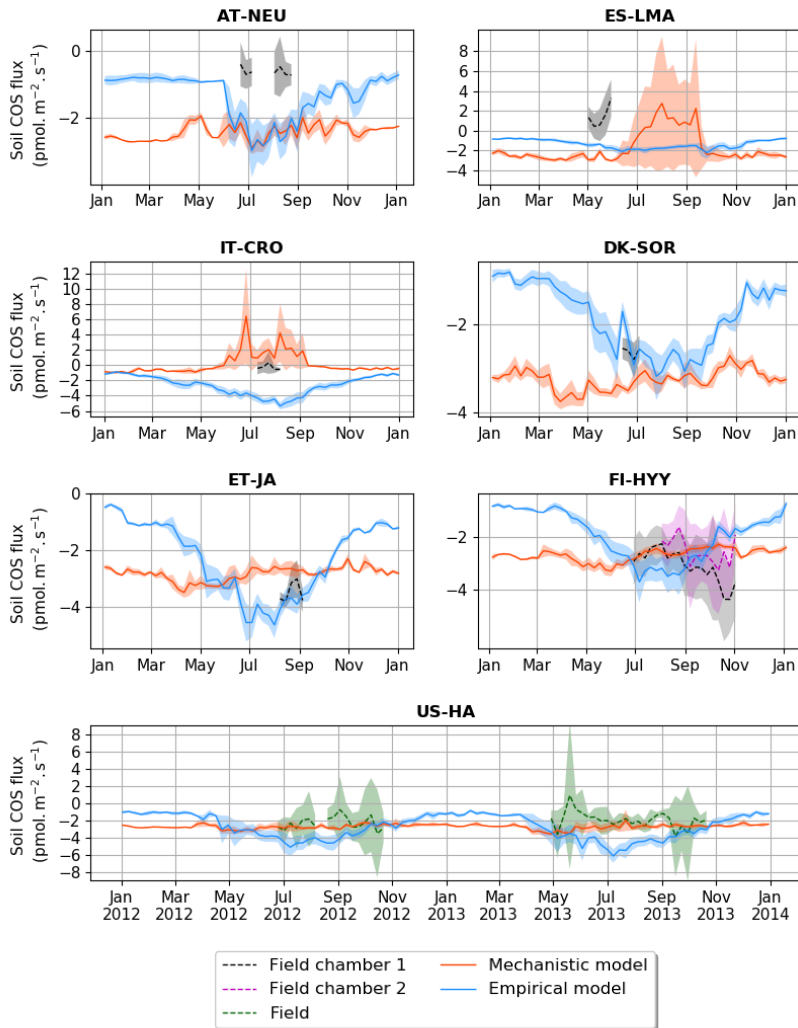
Table 3: Comparison between simulated and measured weekly soil COS fluxes (RMSD) at ES-LMA, DK-SOR, IT-CRO, AT-NEU, ET-JA, FI-HYY and US-HA. Values in bold show the highest accuracy between modelled and measured soil COS fluxes for each site (smallest RMSD values). Soil COS fluxes are computed with a variable atmospheric COS concentration.

	Empirical model	Mechanistic model
ES-LMA	3.20	4.39
DK-SOR	0.45	0.75
IT-CRO	4.45	2.58
AT-NEU	1.76	1.82
ET-JA	0.84	0.46
FI-HYY-chamber-1	1.21	0.89
FI-HYY-chamber-2	0.99	0.58
US-HA	3.34	1.19
Mean-all-sites	2.03	1.58

a mis en forme : Justifié



a mis en forme : Justifié



1454

1455

1456

1457

1458

1459

1460

1461

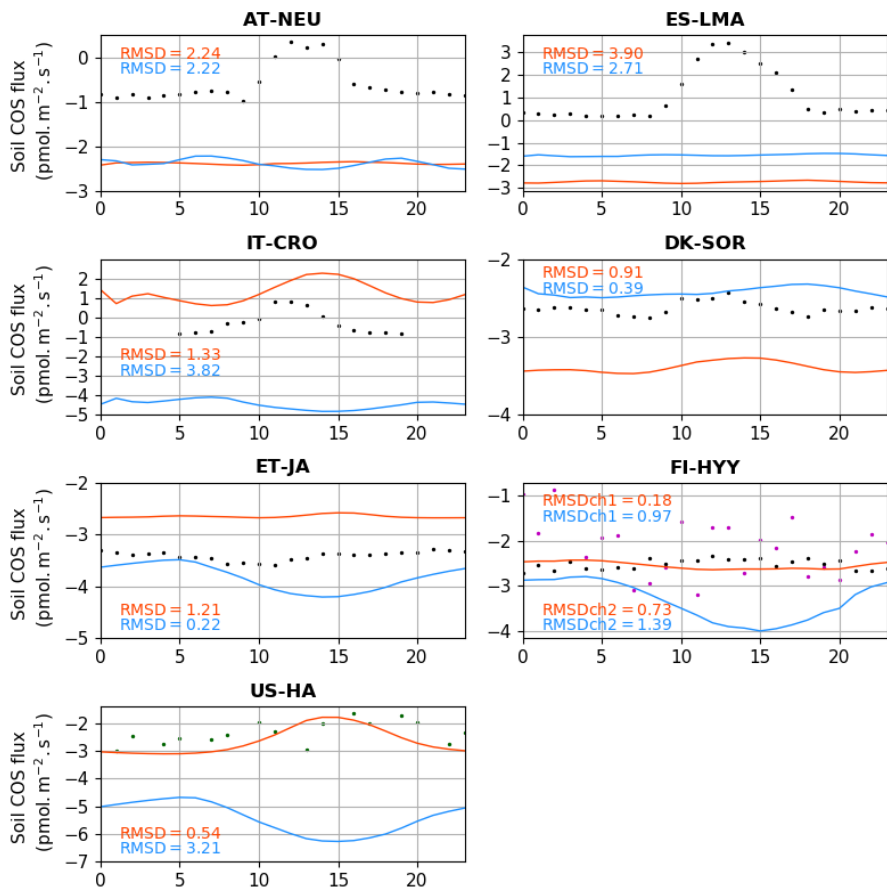
1462

1463

Figure 2: Seasonal cycle of weekly average net soil COS fluxes ($\text{pmol m}^{-2} \text{s}^{-1}$) at: AT-NEU, ES-LMA, IT-CRO, DK-SOR, ET-JA, FI-HYY and US-HA. The shaded areas around the observation and simulation curves represent the standard-deviation over a week for each site. Soil COS fluxes are computed with a variable atmospheric COS concentration. RMSD values between the simulated and observed fluxes are given with the respective model color at each site, and for both soil chambers at FI-HYY (ch1 and ch2).

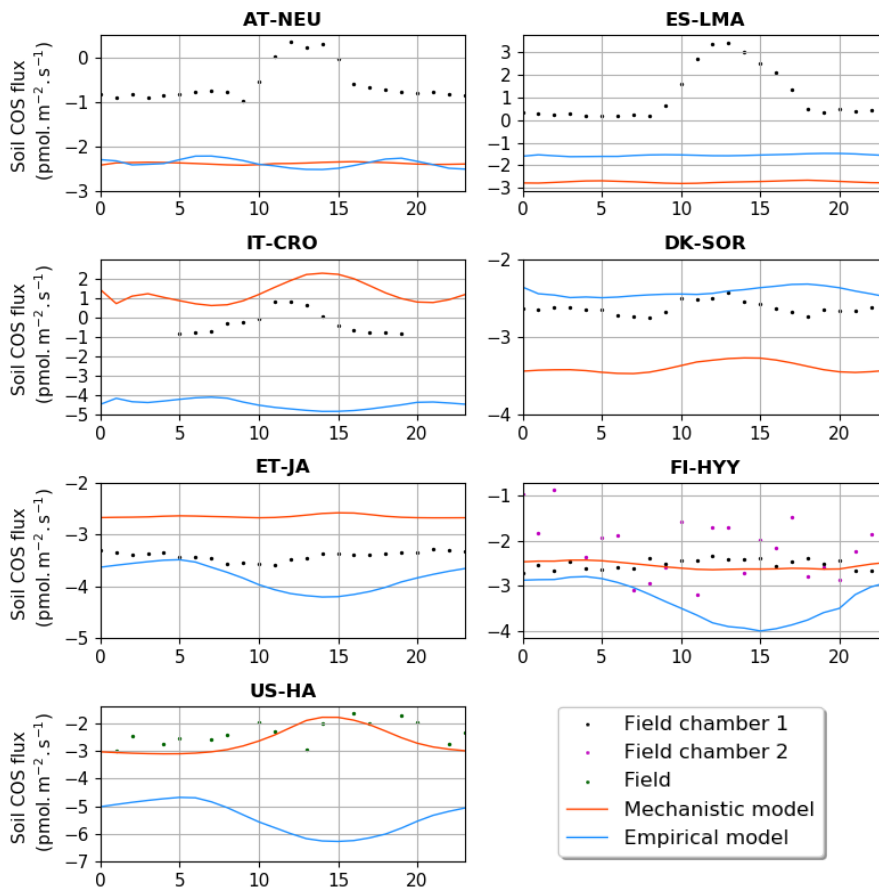
1464 **Table 4: Comparison between simulated and measured half-hourly soil CO₂ fluxes (RMSD) at ES-LMA, DK-SOR, IT-**
 1465 **CRO, AT-NEU, ET-JA, FI-HYY and US-HA. Values in bold show the highest accuracy between modelled and**
 1466 **measured soil CO₂ fluxes for each site (smallest RMSD values). Soil CO₂ fluxes are computed with a variable**
 1467 **atmospheric CO₂ concentration.**

	Empirical model	Mechanistic model
ES-LMA	2.71	3.90
DK-SOR	0.39	0.91
IT-CRO	3.82	1.33
AT-NEU	2.22	2.24
ET-JA	0.22	1.21
FI-HYY chamber 1	0.97	0.18
FI-HYY chamber 2	1.39	0.73
US-HA	3.21	0.54
Mean all sites	1.87	1.38

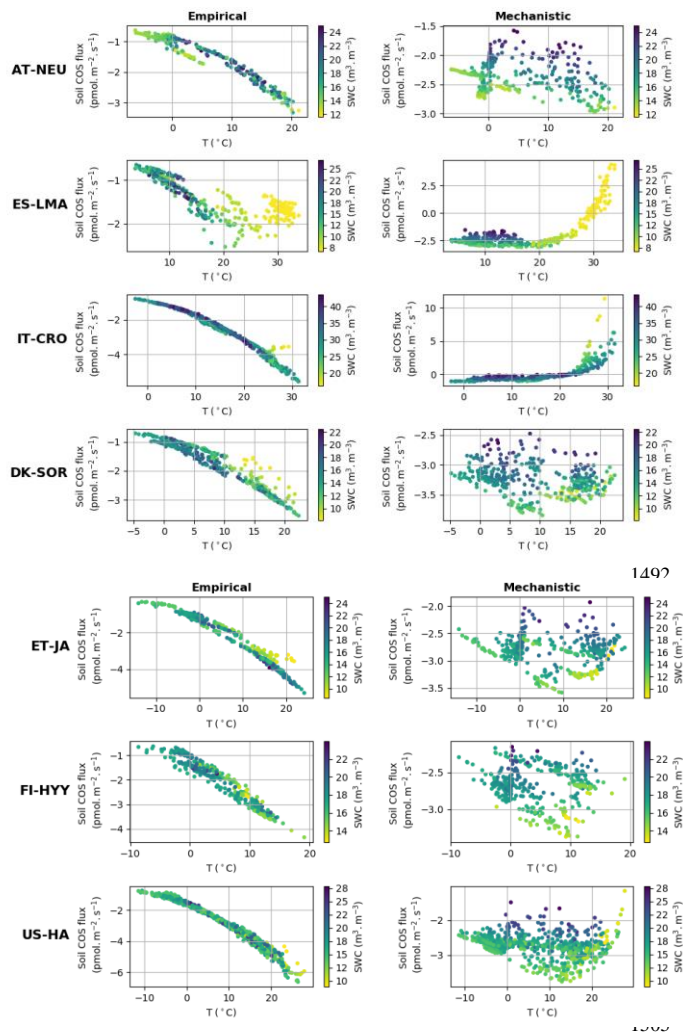


468

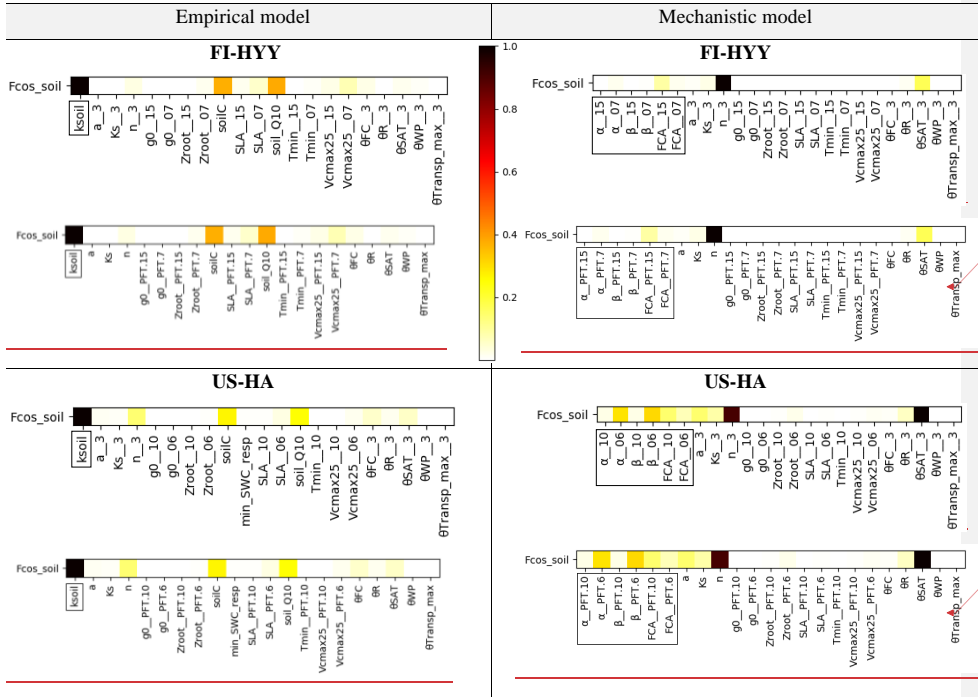
a mis en forme : Justifié



1469
 1470 **Figure 3:** Mean diel cycle of net soil COS fluxes ($\text{pmol m}^{-2} \text{s}^{-1}$) over a month at: AT-NEU (08/2015), ES-LMA (05/2016),
 1471 IT-CRO (07/2017), DK-SOR (06/2016), ET-JA (08/2016), FI-HYY (08/2015) and US-HA (07/2012). Soil COS fluxes are
 1472 computed with a variable atmospheric COS concentration. The observation-based diel cycles (dots) are computed using
 1473 Random Forest models at At-NEU, ES-LMA, IT-CRO, DK-SOR and ET-JA. At AT-NEU and ES-LMA, RMSD values
 1474 between the simulated and observed fluxes are given with the respective model color at each site, and for both soil
 1475 chambers at FI-HYY (ch1 and ch2).



1506
 1507 **Figure 4: Simulated daily average net soil CO₂ flux (pmol m⁻² s⁻¹) versus soil temperature (°C) and soil water content**
 1508 **(SWC) (m³.m⁻³) at AT-NEU, ES-LMA, IT-CRO, DK-SOR, ET-JA, US-HA and FI-HYY, for the empirical and the**
 1509 **mechanistic model.**



a mis en forme : Droite

a mis en forme : Droite

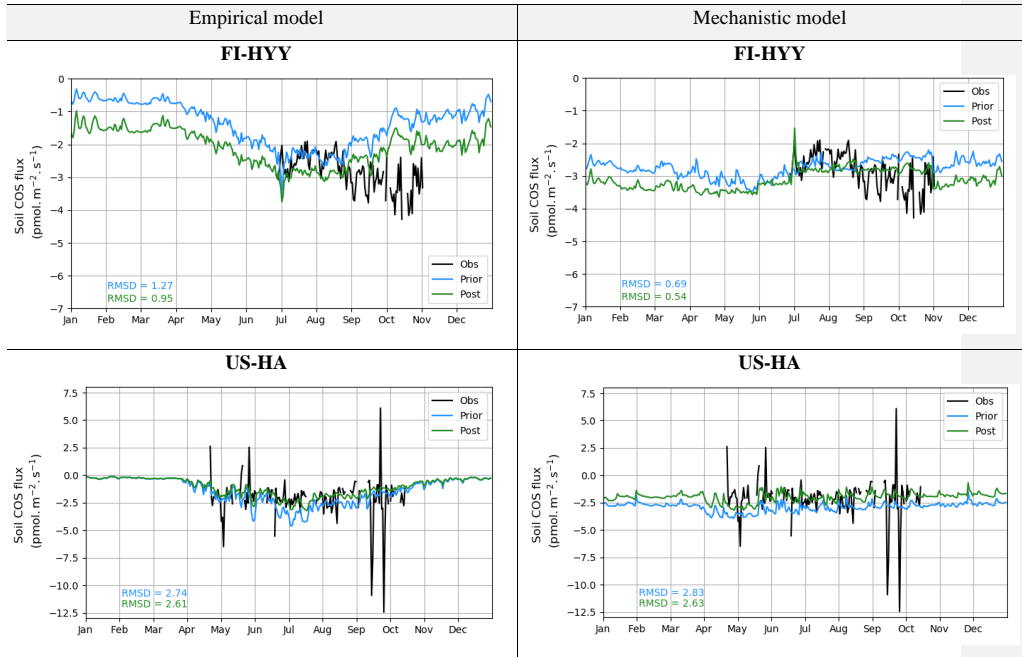
1510
 1511 **Figure 5: Morris sensitivity scores of the key parameters to which soil COS fluxes are sensitive, for the empirical (left)**
 1512 **and the mechanistic (right) models. The two studied sites are FI-HYY (top) and US-HA (bottom). Full descriptions of**
 1513 **each tested parameter can be found in Tables S3 and S4 in the supporting information. The PFT is indicated numbers**
 1514 **at the end of the parameter names correspond to the PFTs at each site for the PFT-dependent parameters, and to the**
 1515 **dominant soil texture for soil texture-dependent parameters (soil texture number 3, i.e. (sandy loam, at FI-HYY and**
 1516 **US-HA)(at FI-HYY: PFT7 = boreal needleleaf evergreen and PFT 15 = boreal natural C3 grassland, at US-HA: PFT6**
 1517 **= temperate broadleaf summergreen and PFT10 = temperate natural C3 grassland), sandy loam, at FI-HYY and US-**
 1518 **HA)(at FI-HYY: PFT7 = boreal needleleaf evergreen and PFT 15 = boreal natural C3 grassland, at US-HA: PFT6 =**
 1519 **temperate broadleaf summergreen and PFT10 = temperate natural C3 grassland). The first-order parameters are**
 1520 **shown in the frames.**

1521

1522

a mis en forme : Justifié

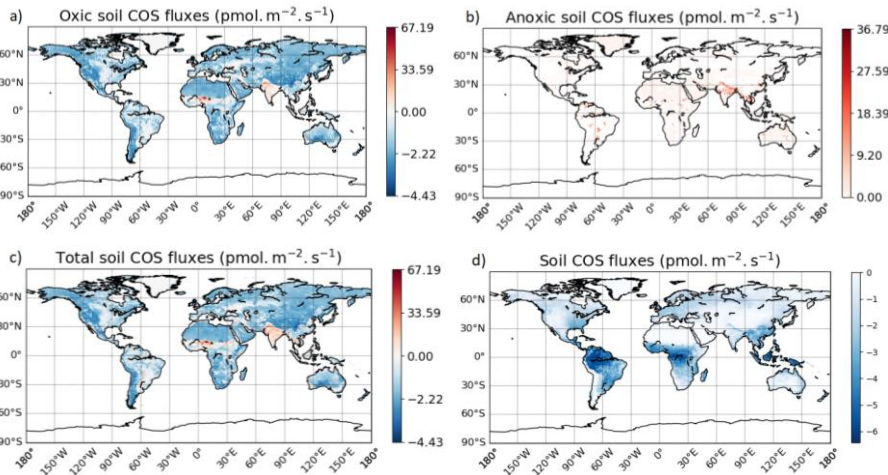
1523



1524

1525 **Figure 6: Prior and post optimization net soil COS fluxes ($\text{pmol m}^{-2} \text{s}^{-1}$) for the empirical (left) and the mechanistic**
1526 **(right) models. The two studied sites are FI-HYY (top) in 2015 and US-HA (bottom) in 2013.**

1527

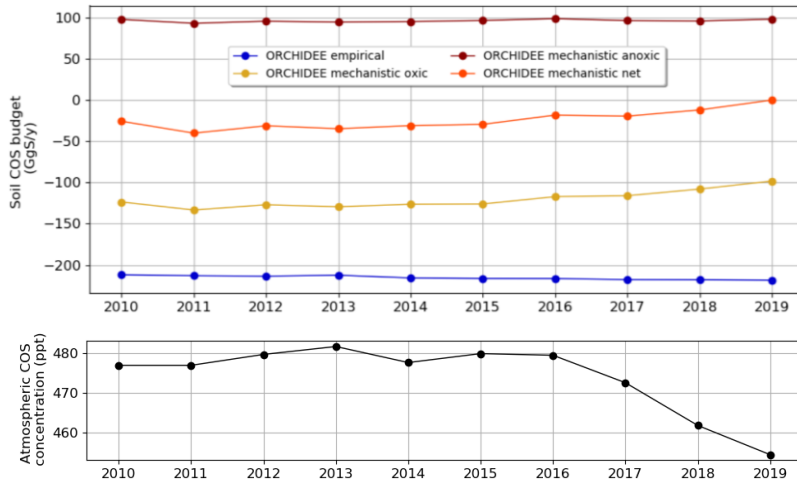


1528

1529

1530 **Figure 7: Maps of mean soil COS fluxes for the mechanistic (a, b, c) and the empirical model (d), computed over 2010-**
 1531 **2019 with a variable atmospheric COS concentration. Color scales were normalized between the minimum and**
 1532 **maximum soil COS flux values and centered on zero for oxic and total soil COS fluxes computed with the mechanistic**
 1533 **model. The map resolution is 0.5°x0.5°.**

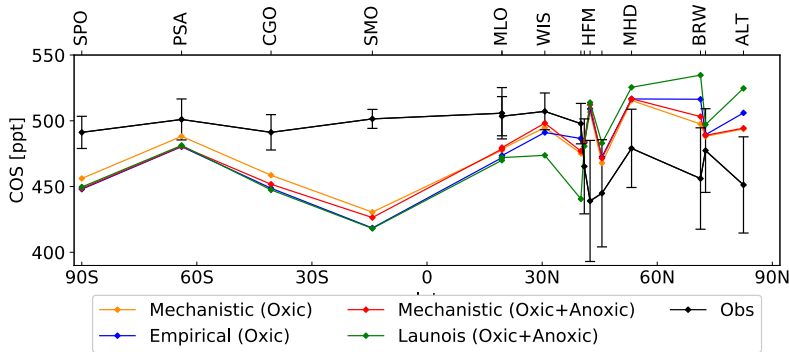
1534



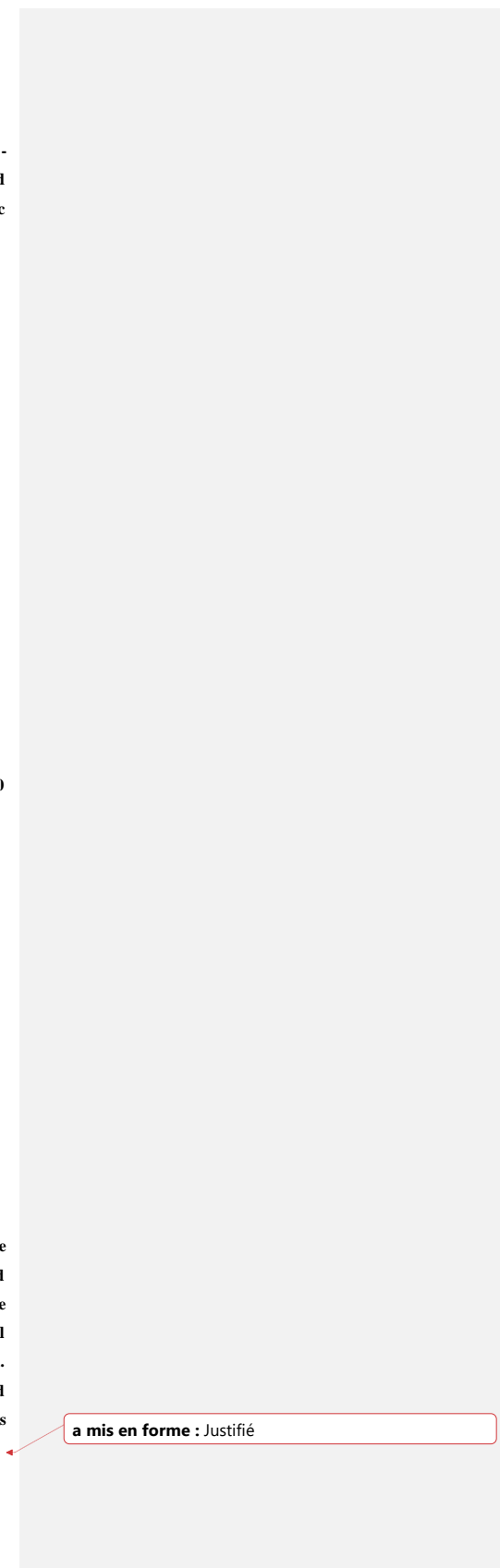
1535

1536 **Figure 8: Evolution of mean annual soil COS budget and mean annual atmospheric COS concentration between 2010**
 1537 **and 2019, computed with a variable atmospheric COS concentration.**
 1538

1539



1540 **Figure 9: Comparison of the latitudinal variations of the COS abundances simulated by LMDZ at NOAA sites with the**
 1541 **observations (black). The LMDZ COS abundances have been vertically shifted such that the means of the simulated**
 1542 **concentrations are the same as the mean of the observations. The error bars around the black curve represent the**
 1543 **standard deviation over the whole studied period at each NOAA site. The orange curve is obtained using the oxic soil**
 1544 **fluxes of the mechanistic model. The red curve is obtained using the oxic and anoxic soil fluxes of the mechanistic**
 1545 **model. The blue curve is given by LMDZ using the oxic soil fluxes from the Berry empirical model. The green curve is obtained**
 1546 **using the soil fluxes from the empirical approach of Launois et al. (2015). For more clarity, the names of the stations**
 1547

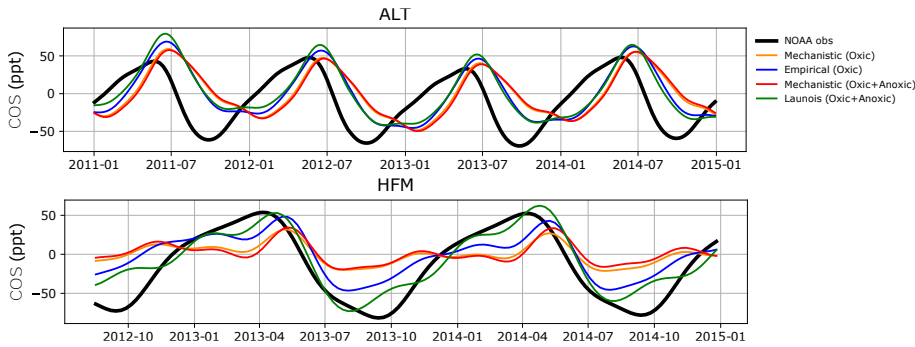


a mis en forme : Justifié

1548 KUM (19.74°N, 155.01°W), NWR (40.04°N, 105.54°W), LEF (45.95°N, 90.28°W) and SUM (72.6°N, 38.42°W) are not
1549 shown on this figure due to their proximity to other stations (Appendix B, Figure B1 and Table B1).

1550

1551



1552

1553

1554 **Figure 10.** Detrended temporal evolution of simulated and observed COS concentrations at two selected sites, simulated
1555 with LMDZ6 transport between 2011 and 2015. The simulated concentrations are obtained by transporting the surface
1556 fluxes described in Table 2, and changing only the contribution from soils, with, for the mechanistic (Oxic soils alone,
1557 and Oxic + Anoxic soils) and empirical approaches (Berry et al., 2013; Launois et al., 2015) simulated with LMDZ6
1558 transport between 2011 and 2015. Top: Alert station (ALT, Canada), bottom: Harvard Forest station (HFM, USA). The
1559 curves have been detrended beforehand and filtered to remove the synoptic variability (see Sect. 2.3.3).

1560

1561 **Table 53:** Comparison of soil COS budget per year (GgS yr⁻¹). The net total COS budget is computed by adding all
 1562 sources and sinks of COS used (anthropogenic, ocean, biomass burning, soils, vegetation, atmospheric OH oxidation,
 1563 photolysis in the atmosphere) used to transport COS fluxes (Table 2).

Period	Kettle et al. (2002)	Berry et al. (2013)	Launois et al. (2015)			<u>Kooijmans et al. (2021)</u>	This study	
			ORCHIDEE	LPJ	CLM4	<u>SiB4 (modified)</u>	Empirical soil model	<u>Mechar</u> soil model
Period	2002	2002–2005	2006-2009			<u>2000-2020</u>	2009-2016	
Plants	-238	-738	-1335	-1069	-930	<u>-664</u>	-576	
Soil oxic	-130	-355	-510			<u>-89</u>	-214	<u>-120</u>
Soil anoxic	+26	Neglected	+101			<u>Neglected</u>	Neglected	+96
Soil total	-104	-355	-409			<u>-89</u>	-214	-30
Net total	+64	+1	-566	-300	-161	<u>(-)</u>	<u>-16535</u>	<u>+19+149</u>

a mis en forme le tableau

a mis en forme : Taquets de tabulation : 2,54 cm, Centré + 5,08 cm, Droite

a mis en forme : Justifié, Espace Après : 0 pt, Interligne : 1,5 ligne

a mis en forme : Justifié